

MICRO SYNTHETIC APERTURE RADAR USING FM/CW  
TECHNOLOGY

by

Ryan L. Smith

A thesis submitted to the faculty of

Brigham Young University

in partial fulfillment of the requirements for the degree of

Master of Science

Department of Electrical and Computer Engineering

Brigham Young University

December 2002

Copyright © 2002 Ryan L. Smith

All Rights Reserved

BRIGHAM YOUNG UNIVERSITY

GRADUATE COMMITTEE APPROVAL

of a thesis submitted by

Ryan L. Smith

This thesis has been read by each member of the following graduate committee and by majority vote has been found to be satisfactory.

\_\_\_\_\_

Date

\_\_\_\_\_

David V. Arnold, Chair

\_\_\_\_\_

Date

\_\_\_\_\_

Michael A. Jensen

\_\_\_\_\_

Date

\_\_\_\_\_

David G. Long

BRIGHAM YOUNG UNIVERSITY

As chair of the candidate's graduate committee, I have read the thesis of Ryan L. Smith in its final form and have found that (1) its format, citations, and bibliographical style are consistent and acceptable and fulfill university and department style requirements; (2) its illustrative materials including figures, tables, and charts are in place; and (3) the final manuscript is satisfactory to the graduate committee and is ready for submission to the university library.

---

Date

---

David V. Arnold  
Chair, Graduate Committee

Accepted for the Department

---

A. Lee Swindlehurst  
Graduate Coordinator

Accepted for the College

---

Douglas M. Chabries  
Dean, College of Engineering and Technology



## ABSTRACT

### MICRO SYNTHETIC APERTURE RADAR USING FM/CW TECHNOLOGY

Ryan L. Smith

Department of Electrical and Computer Engineering

Master of Science

This work demonstrates a synthetic aperture radar (SAR) capable of generating high quality images using frequency modulated, continuous wave (FM/CW) technology and its advantages over conventional SAR systems. A mathematical analysis examines the range and azimuth compression of a single target and shows that FM/CW based SAR produces compressed images. A 10 GHz prototype is developed using innovative coplanar techniques and a simple FM/CW signal generator. The performance of the system matches the expected performance based upon the analysis. The experimental and mathematical models support the conclusion that FM/CW based SAR is capable of creating well-compressed imagery in both range and azimuth.

## ACKNOWLEDGMENTS

The work contained in this thesis is made possible by the contributions and funding of the Canadian National Railway, National Aeronautic and Space Administration, and the Brigham Young University College of Engineering. Thanks is given to Don Crockett, Jeff Beard, and Jonathan Waite who contributed to development of the FM/CW radar system and assisted me on several projects.

David Arnold who acted as my advisor and mentor provided me with an early opportunity to learn engineering principles. I express my thanks to him for believing in my abilities and making challenging research opportunities available to students. He also helped me strengthen areas of my skills that were lacking and helped me achieve the educational goals that I had set. Michael Jensen assisted in this research with his expertise in high frequency circuit simulation and design. Some of the simulations used in this work are based upon work assignments he gave in class course work.

I am grateful to my parents for their encouragement to gain a higher education and the example of work and endurance. My father's interest in science and its application initiated a desire in me that feeds the joy I find in engineering. A special thanks goes to my wife Michelle and daughter Hannah for their encouragement and support in completing this thesis. They were patient during many unexpected delays, allowing me to focus on the development of this thesis.

# Contents

<b>Acknowledgments</b>	<b>vi</b>
<b>List of Tables</b>	<b>xi</b>
<b>List of Figures</b>	<b>xv</b>
<b>1 Introduction</b>	<b>1</b>
1.1 Purpose . . . . .	1
1.2 Contributions of this Work . . . . .	2
1.3 Outline . . . . .	3
<b>2 SAR Background</b>	<b>5</b>
2.1 Microwave Sensors . . . . .	5
2.2 Current SAR Systems and Applications . . . . .	8
2.2.1 SIR-C/X-SAR . . . . .	8
2.2.2 NASA's AIRSAR . . . . .	11
2.2.3 Intermap's STAR-3i . . . . .	13
2.2.4 BYU's SAR Program . . . . .	16
2.2.5 Basis for the BY $\mu$ SAR . . . . .	20
<b>3 FM/CW SAR Techniques</b>	<b>23</b>
3.1 FM/CW Range Detection and Resolution . . . . .	23
3.1.1 Range Detection . . . . .	23
3.1.2 Range Resolution and Processing Gain . . . . .	25
3.2 SAR Geometry . . . . .	28
3.3 Illustrated SAR Compression . . . . .	28

3.3.1	Pulsed FM SAR . . . . .	29
3.3.2	FM/CW SAR . . . . .	32
3.4	Range Compression Techniques . . . . .	33
3.4.1	FM/CW Range Compression . . . . .	33
3.4.2	Pulsed FM Range Compression . . . . .	36
3.4.3	Range Compression Contrast . . . . .	40
3.5	Azimuth Compression . . . . .	41
3.5.1	Derivation . . . . .	41
3.5.2	FM/CW Phase Error Analysis . . . . .	45
3.6	FM/CW Limitations and Optimization . . . . .	52
<b>4</b>	<b>BY<math>\mu</math>SAR System Design</b>	<b>55</b>
4.1	BY $\mu$ SAR Specifications . . . . .	55
4.1.1	Airborne System Specifications . . . . .	55
4.1.2	Track System Specifications . . . . .	58
4.1.3	Block Diagram . . . . .	58
4.2	Transmitter . . . . .	61
4.2.1	LFM Generation . . . . .	61
4.2.2	RF Module . . . . .	63
4.2.3	RF Driver Module . . . . .	65
4.2.4	Algorithms and Control Code . . . . .	69
4.3	Low Noise Receiver . . . . .	71
4.3.1	Low Noise Amplifier . . . . .	72
4.3.2	RF Mixer Module . . . . .	75
4.3.3	IF Gain Module . . . . .	76
4.4	System Assembly . . . . .	77
4.5	Signal to Noise Analysis . . . . .	79
4.5.1	The Radar Equation . . . . .	81
4.5.2	Radiometric Noise . . . . .	84
4.5.3	Thermal Noise . . . . .	86

4.5.4	SNR Calculations . . . . .	88
<b>5</b>	<b>BY<math>\mu</math>SAR System Tests</b>	<b>91</b>
5.1	Bench Tests . . . . .	91
5.1.1	Phase Counter . . . . .	91
5.1.2	Impulse Response . . . . .	92
5.1.3	Transmitter Spectral Output . . . . .	94
5.2	Inverse SAR of Corner Reflector . . . . .	94
5.3	Imaging using Track Platform . . . . .	97
<b>6</b>	<b>Conclusion</b>	<b>103</b>
6.1	Summary . . . . .	103
6.2	Future Work . . . . .	104
6.3	Contributions . . . . .	105
<b>A</b>	<b>Channelized Coplanar Waveguide Technology</b>	<b>107</b>
A.1	Coplanar's Benefits . . . . .	107
A.2	50 $\Omega$ Transmission Line . . . . .	108
A.3	DC Isolation and Cavity Effects . . . . .	110
A.4	CCPW Elements . . . . .	111
A.5	Prototypes and Developing . . . . .	113
<b>B</b>	<b>SAR Imaging Functions</b>	<b>117</b>
<b>C</b>	<b>SAR Visual Basic Code for Instrument Control</b>	<b>121</b>
<b>D</b>	<b>PicBasicPro Code for Transmitter Module</b>	<b>129</b>
<b>E</b>	<b>PicBasicPro Code for Receiver Module</b>	<b>137</b>
<b>F</b>	<b>PECL Design Overview</b>	<b>141</b>
F.1	ECL Basic Gate . . . . .	141
F.2	Positive Emitter Coupled Logic . . . . .	141
F.3	Termination of Transmission Lines and Interconnects . . . . .	142



## List of Tables

2.1	Comparison of Six SAR Systems with the BY $\mu$ SAR. . . . .	22
4.1	BY $\mu$ SAR Airborne Parameters . . . . .	57
4.2	BY $\mu$ SAR Track Parameters . . . . .	59
4.3	LNA Interdigital Dimensions . . . . .	76
5.1	RF Module Output Spectrum . . . . .	95
A.1	Tangential Line Coupling in Coplanar . . . . .	113
F.1	ECL to PECL Voltage Level Conversion . . . . .	142





## List of Figures

2.1	Radiometer Image of Southeast Asia . . . . .	6
2.2	SIR-C/X-SAR Aboard the Space Shuttle . . . . .	8
2.3	SIR-C Image of Salt Lake City . . . . .	9
2.4	X-SAR Image enhancement of the Rocky Mountains . . . . .	10
2.5	AIRSAR's DC-8 Aircraft and Equipment Racks . . . . .	11
2.6	AIRSAR Image of Canadian Farm Land . . . . .	12
2.7	STAR-3i Integrated into a Learjet 36 . . . . .	14
2.8	STAR-3i Created DEMs near Denver, Colorado . . . . .	15
2.9	Truck platform used to deploy BYUSAR . . . . .	16
2.10	BYU SAR Image near University Avenue, Provo, Utah . . . . .	17
2.11	YINSAR uncovers an archeological site in Israel . . . . .	18
2.12	YINSAR's Aircraft and Hardware . . . . .	19
2.13	Image of BYU Campus by YINSAR . . . . .	20
3.1	The Real Part of the Exponential Chirp $m(t)$ . . . . .	24
3.2	How a Chirp is Used to Measure Distance . . . . .	26
3.3	Rayleigh Resolution and the Sinc Function . . . . .	27
3.4	SAR Geometry . . . . .	29
3.5	Illustrated Range Compression . . . . .	30
3.6	Illustrated Azimuth Compression . . . . .	31
3.7	FM/CW Model of Transmitted and Return Signal Relationship. . . . .	34
3.8	Mathematical and Simulated FM/CW Range Compression . . . . .	41
3.9	Mathematical Model Showing Both SNR and Resolution Degradation . . . . .	42
3.10	Distance Relationship of Moving Platform and a Single Target. . . . .	43
3.11	Range Walk due to Extended FM/CW Chirp Period . . . . .	50

3.12	Compressed Azimuth Response for FM/CW . . . . .	52
4.1	Maximum and Minimum Range . . . . .	56
4.2	Range resolution is related to slant range resolution, range, and elevation. . . . .	56
4.3	Simplified Block Diagram of SAR System. . . . .	60
4.4	VCO Nonlinearities . . . . .	62
4.5	Block Diagram of Transmitter Architecture. . . . .	63
4.6	Transmitter Module Schematic. . . . .	64
4.7	Transmitter Module . . . . .	65
4.8	Main board Schematic Including Transmitter Driver. . . . .	66
4.9	Driver Board without Modules. . . . .	67
4.10	Frequency Profile of Transmit Signal . . . . .	68
4.11	Transmitter Calibration Algorithm . . . . .	71
4.12	Visual Basic Graphical User Interface . . . . .	72
4.13	Biassing Network for Gate and Drain. . . . .	73
4.14	NE329S01 $\Gamma_s$ Biased at 2 Volts and 10 mA . . . . .	74
4.15	NE329S01 $\Gamma_s$ Biased at 3 Volts and 20 mA . . . . .	75
4.16	Matching Network and Transistor Setup for a 50 dB Low Noise Amplifier. . . . .	76
4.17	ADS Simulation of LNA. . . . .	77
4.18	ADS Simulation Results for LNA. . . . .	77
4.19	Measurements of 10 GHz Low Noise Amplifier with 50 dB of Gain. . . . .	78
4.20	10 GHz Low Noise Amplifier with 50 dB of Gain. . . . .	78
4.21	HMC220S08 Mixer in Housing. . . . .	79
4.22	IF Filter and Amplification Module. . . . .	79
4.23	Bottom View of RF Subassembly . . . . .	80
4.24	Top View of RF Subassembly . . . . .	81
4.25	Complete SAR System with all Modules in Place. . . . .	82
4.26	Radiometric Noise for Radar . . . . .	84
4.27	Typical RF Receiver's Noise Figure and Gain . . . . .	87
5.1	Setup for verifying the accuracy of the SAR's phase counting circuit. . . . .	92
5.2	Measurement of Linearity of Phase Counter . . . . .	92

5.3	Test Setup for the Impulse Response. . . . .	93
5.4	Time and Frequency Domain Responses for the Impulse Response Test	94
5.5	BY $\mu$ SAR is Stationary While it Images a Moving Corner Reflector. .	95
5.6	Azimuthal Response from a Moving Corner Reflector . . . . .	96
5.7	Azimuth and Range Resolution . . . . .	96
5.8	Range and Azimuth Compressed Image of a Corner Reflector . . . . .	97
5.9	BY $\mu$ SAR Imaging the Fletcher Building and Wilkinson Center . . . . .	98
5.10	Radar Acquisition Setup for Imaging . . . . .	99
5.11	SAR Image of Fletcher Building Contrasted with Photographs . . . . .	100
5.12	Image Taken of the Fletcher and Clyde Buildings from Airborne YINSAR	101
A.1	Static solution of microstrip and coplanar technologies . . . . .	108
A.2	Test fixture Used to Analyze Coplanar Circuits . . . . .	109
A.3	Layout of Simulation and Board to Case Transition . . . . .	110
A.4	ADS Momentum Simulation Results of a 50 $\Omega$ Line. . . . .	111
A.5	Board Used to Analyze Isolation in Coplanar . . . . .	112
A.6	A 5 Port Hybrid Ring in Coplanar . . . . .	114
A.7	Fundamental Circuit Elements in Coplanar . . . . .	115
A.8	Staggered Interdigital Capacitor . . . . .	115
F.1	An AC Signal Coupled to an ECL Device. . . . .	143

# Chapter 1

## Introduction

### 1.1 Purpose

Synthetic Aperture Radar (SAR) is recognized for its ability to construct high-resolution images. Current strip-map SAR systems are complex in design because they use pulsed FM waveforms to produce the radar signals. FM/CW is a technique used in many radar systems to achieve high pulse compression and large processing gains. FM/CW has not been validated as a viable SAR foundation for remote sensing applications. The work presented here shows that a SAR is capable of generating high quality imagery devoid of serious defects using FM/CW technology. The proof is based upon a mathematical analysis and the results of a prototype FM/CW based SAR system.

Six SARs are described along with their platforms and uses in order to show the significance of the novel SAR system described in this work. Six SAR systems are described ranging from the orbital SIR-C/X-SAR aboard the space shuttle to a system that is used in a Cessna airplane. Their uses range from archeology to plate tectonics by providing information that is not easily obtained by other means. The Brigham Young micro SAR (BY $\mu$ SAR) finds a niche by providing a compact, affordable, high resolution SAR with the aid of FM/CW technology.

Traditional methods of generating radar signals are contrasted with this use of FM/CW to show that a number of key benefits are achieved using the latter. The comparison is first carried out in an illustrative manner followed by a detailed mathematical analysis. The analysis shows the range and azimuth compression for

both types of systems and concludes with a phase error analysis. The phase analysis shows that FM/CW based SAR does not introduce significant errors in the azimuthal phase response and thus allows excellent azimuth compression.

A short guide is given on how to select the optimum parameters for a FM/CW-based SAR using key equations derived in the analysis section 3.5.2. A prototype SAR based on the earlier developments is then shown. The system is designed and built using coplanar technology which is covered in the Appendix. The SAR performance is measured by plotting the range and azimuth compressed response of a single corner reflector. Its abilities are further illustrated in an image acquired of a building. These results show that FM/CW technology is able to create high-quality SAR imagery that is well-compressed in azimuth and range. The BY $\mu$ SAR is therefore well suited to many applications that are not currently feasible in traditional SAR systems.

## 1.2 Contributions of this Work

The work in this thesis introduces a sensor and an analytic solution to a new technique for SAR imaging. The analytic solution derived represents the range compressed signal in the frequency domain. It shows that FM/CW SAR introduces no azimuth phase errors within limitations, but adds a linear shift to range walk as shown. A simple LFM signal generator is designed and built that obtains good linearity and fair frequency stability.

Techniques are developed to design and make innovative coplanar circuits using relatively inexpensive equipment. A high gain, low noise amplifier is achieved using a low cost printed circuit board substrate and this gives confidence for the design of other technical building blocks of microwave circuits. The development of a modular style microwave design is initiated where parts such as the driver circuit could be reused in other designs helping to eliminate unnecessary design cost and effort.

### 1.3 Outline

This thesis is developed as follows:

Chapter 2 gives a background to SAR by describing microwave sensors and explaining their benefits. Six different SAR systems are analyzed by looking at their application and the images they produced.

Chapter 3 covers FM/CW range detection and resolution followed by SAR geometry. An illustrative approach is taken to FM/CW SAR compared to pulsed FM SAR before it is mathematically contrasted. The effects that FM/CW has on SAR imaging is presented along with a guide for optimum system configuration.

Chapter 4 specifies the parameters for a BY $\mu$ SAR prototype design. It then covers the design and construction of the transmitter, receiver, and other system components. A detailed signal-to-noise ratio analysis covers radiometric and thermal noise sources.

Chapter 5 identifies several bench tests performed on the BY $\mu$ SAR system and provides the results. The radar resolution is then measured using a moving corner reflector. Data is then taken by the SAR system and an image of a building is formed using SAR processing. This image is then compared to photographs.

Chapter 6 is the conclusion containing a summary of the thesis, a outline of proposed future enhancements, and a list the contributions made.

Appendix A covers a relatively new technology of channelized coplanar waveguides used to build microwave circuits. Here its benefits and abilities to realize key elements with ease are examined. The board manufacturing system is also described along with issues encounter in the board manufacturing process.

Appendix B includes the functions used in the processing of the SAR images.

Appendix C shows the Visual Basic code used for instrument control.

Appendix D shows the PicBasicPro code for the microcontroller used in the transmitter.

Appendix E shows the PicBasicPro code for the microcontroller used in the receiver's IF gain block.

Appendix F gives a brief overview and design help for Positive Emitter Coupled Logic (PECL).

## Chapter 2

### SAR Background

This chapter gives a brief background of microwave sensors and provides the motivation for the development of the BY $\mu$ SAR. Six SAR systems are described ranging from an orbital sensor aboard the space shuttle to units mounted in small aircraft. In addition, numerous examples of current SAR imagery products are shown in figures that graphically illustrate their usefulness. The advantages of a miniature system like BY $\mu$ SAR are then discussed in light of the current systems now in use, and a comparison follows in a table.

#### 2.1 Microwave Sensors

SAR has many features that give it an advantage over other sensors for imaging. SAR is selected for its ability to penetrate the atmosphere and ground, precisely measure range, and provide high resolution images with height detection.

Images are able to quickly communicate a large amount of information that is otherwise obscure and difficult to communicate. Decisions are made based on the information that is available and accessible. The eye and mind are trained to look for and focus on contrasts in order to analyze a given view. Rich optical images are formed by bordering colors and shades that produce sharp edges and high contrasts, and these are prevalent in man-made and natural structures. Then why use radar when optics can provide an image that is full of detail and familiar to the observer?

Microwaves have three key advantages over optics. First, they can penetrate rain, smoke and dust clouds; second, they are not dependent on the sun for illumination; and third, they are able to penetrate through vegetation and soils. The ability of



radar signals to penetrate is a linear function of wavelength, where longer wavelength signals penetrate deeper. Large contrasts are seen in radar images between objects that reflect energy well and materials that do not. Microwave frequencies range from 300 MHz to 100 GHz corresponding to wavelengths of 1m to 3 mm respectively [1].

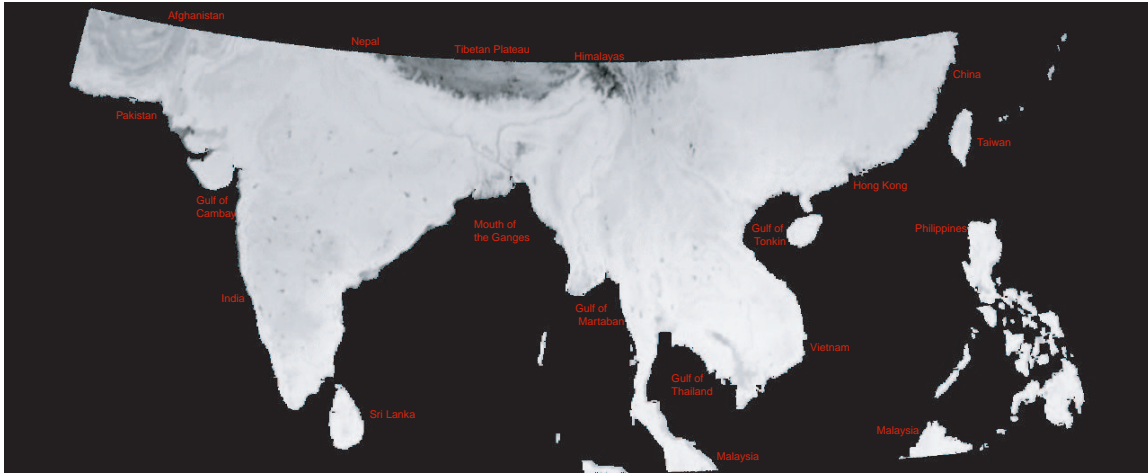


Figure 2.1: A radiometer image of southeast Asia that shows the contrast in brightness temperature. The Himalayan high lands appear cold compared to the Indian continent. The data is from the horizontal 85.5 GHz channel of the SSM/I F13 spacecraft and processed using BYU’s algorithms.

Microwave sensors are classified into two categories, active and passive. A passive sensor is one that depends on energy radiated from the target which is related to the object’s physical temperature. These devices are called radiometers, and they require sensitive receivers in order to detect the small amount of energy being emitted from the earth. A radiometer’s resolution is based primarily on its antenna beamwidth, and a swath is typically produced by scanning the beam back and forth. Figure 2.1 shows a radiometer image over the Indian continent where the cold Tibetan Plateau contrasts with the warmer Indian mainland with a resolution of 12.5 x 12.5 km [2].

The main feature of a radiometric image is the contrast of the brightness temperature as a product of the physical temperature and emissivity. Emissivity is the relation of brightness temperature to the physical temperature, with its value ranging from zero to one. Metal objects have a emissivity of zero and appear very dark where land surfaces vary from 0.3 to 0.7. Ocean and lakes have a low emissivity and thus appear much colder than land. Dark spots in the image indicate sites of urban centers and developed areas.

An active sensor transmits energy that reflects off targets in a scene and is then received by a sensor. The transmit and receive signals are compared using processing techniques that extract effects produced by individual targets known as a coherent processing. Active sensors are also called Radar (Radio Detection and Ranging)[1]. Radar is commonly thought of as a circular green display that has a scan beam rotating around the center, displaying a target as a bright dot when detected. This is known as the plan-position indicator because it is able to measure the distance to an object with precision.

Radar signals can be modified or filtered into a format that displays the information of interest with an appropriate amount of contrast. Doppler radar used in weather forecasting uses bright colored maps to reveal storm systems as they move over a region. Radar does not differentiate the color spectrum like an optical camera; rather, it perceives electromagnetic properties of physical objects as well as the geometric shape and orientation of targets[1]. For example, metal objects reflect electromagnetic (EM) waves much like a mirror reflects light. Other materials absorb most of the incoming EM energy similar to the way black objects absorb optical energy.

SAR is an active sensor that uses multiple illuminations to produce a high resolution image. Signals are processed to get desired information such as range, height, and the scene's electromagnetic properties. Interferometric SAR is a system that has multiple receive antennas that are separated vertically on the platform. This geometrical relationship allows the measurement of relative heights, thereby enabling terrain mapping [3]. SAR systems are commonly used in military applications to

perform target recognition, reconnaissance, damage assessment, and border watch. This work focuses on non-military systems and their applications.

## 2.2 Current SAR Systems and Applications

Six systems are contrasted with key features of frequency, resolution, platform velocity, swath width, elevation, transmit and system power, imaging rate, in-flight or post-flight processing, weight, and cost. Applications include terrain mapping, archeology, agricultural and urban planning, plate tectonics, and oceanography. The six systems that will be described are: SIR-C/X-SAR, NASA's AIR-SAR, Intermap's STAR-3i, and BYU's BYU-SAR, YSAR, and YINSAR. The  $BY\mu$ SAR is then contrasted with these six systems showing that it provides a valuable and complementary source of SAR imagery.

### 2.2.1 SIR-C/X-SAR



Figure 2.2: SIR-C/X-SAR aboard the space shuttle at an orbit altitude of 225 km. Courtesy of NASA/JPL.

This section looks at the SIR-C/X-SAR system and then at a diverse terrain map over Salt Lake City, Utah that was created using data collected by SIR-C shown in Figure 2.3. Figure 2.4 is shown of the Rocky Mountains in Montana showing the usefulness of SAR in geology.

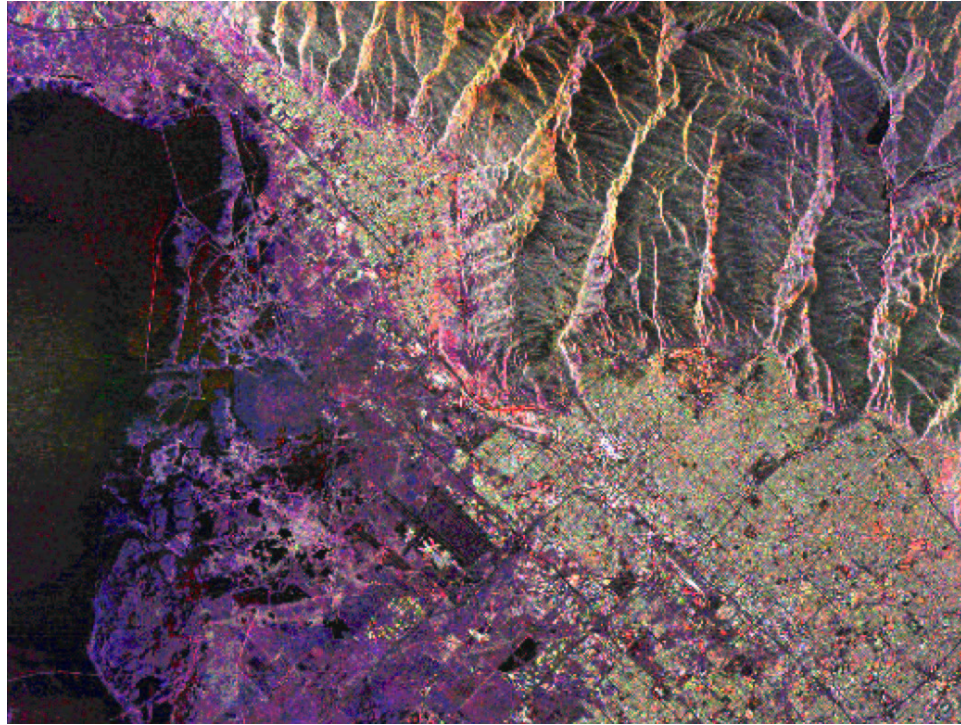


Figure 2.3: SIR-C image of Salt Lake City, Utah showing the lake, mountains, and city. Courtesy of NASA/JPL.

X-SAR is a 9.6 GHz system developed by the German and Italian Aerospace Agencies for use on the space shuttle as seen in Figure 2.2. SIR-C was developed by the United States and operated in the L and C bands. Both SAR systems operate simultaneously aboard the space shuttle. Their primary purpose is imaging vegetation variation, oceans, snow, ice and geological activity [4]. The space shuttle orbits 225 km above the earth while imaging with X-SAR, producing a 20 to 70 km swath on the surface of the earth with a 25 x 25 m resolution and an imaging rate of 17,000

$km^2/min$  [5]. This is a 250,000 times resolution improvement over images obtained with the passive sensor aboard the SSM/I spacecraft. Pulses are sent out at a 1240 to 1736 Hz rate, with peak transmit power level at 1.4 kW. The system draws 3 to 9 kW, enough to consume almost the entire electrical power capability of the shuttle. Most of the other systems on the shuttle must be shut down while imaging is in process. The instrument weighs 11,000 kg and processing is accomplished post-flight. The X-SAR does provide excellent resolution at orbital altitudes and this can be seen from its images.

Figure 2.3 is a SIR-C image of Salt Lake City, Utah where there is great contrast between the lake, city and mountains. Here color and shading are added to make the 2D image appear 3-D. Roadways are visible and differences are seen throughout the city. The Salt Lake International airport is seen below and to the left of center in the image, appearing as a black rectangle.

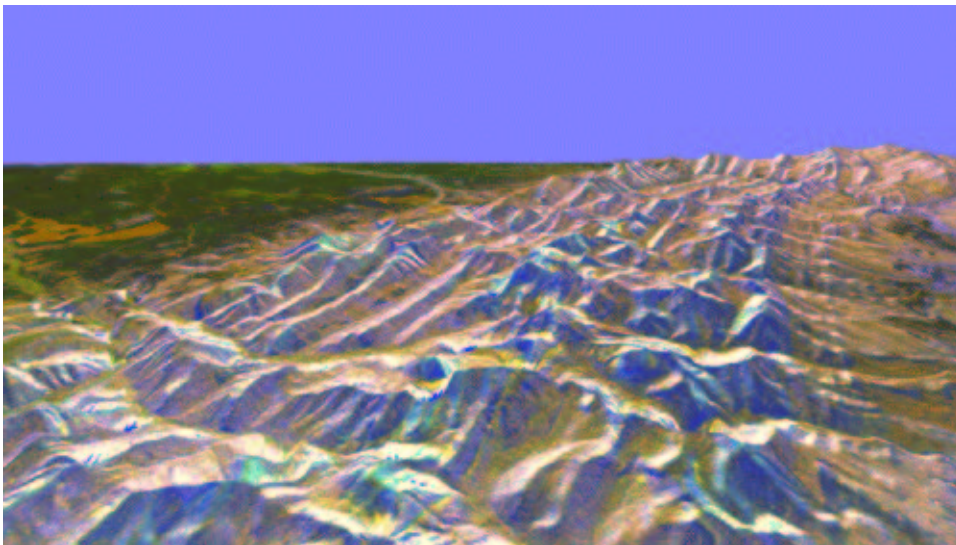


Figure 2.4: X-SAR imagery overlaid on a topographical map of the Rocky Mountains 150 miles west of Great Falls, Montana. This image shows the effects of plate tectonic activity seen by the ripples produced by two large continental plates colliding. Courtesy of NASA/JPL.



The next image, Figure 2.4, is of the Rocky Mountains located 150 miles west of Great Falls, Montana. A topographical map is colored and shaded using X-SAR imagery to give the 3-D effect and is useful to geologists who study the effects of platetectonics and associated phenomena. Ripples are easily seen due to the impact of the two plates colliding. What is not shown in the image is the height sensitivity of the elevation map. Based on this sensitivity, digital elevation maps (DEMs) may be constructed, giving precise surface topographies. Scientists can determine the motion of plates by monitoring the change in the topography over a number of years which allows them to more accurately predict platetectonic events [6].

### 2.2.2 NASA's AIRSAR



(a) DC-8 Jetliner



(b) AIRSAR Equipment Racks

Figure 2.5: Figure (a) shows AIRSAR, a DC-8 commercial jetliner with several different types of SAR systems operating at three different frequencies. Figure (b) shows AIRSAR 5 rack instrument cluster used to process SAR data real time. Courtesy of NASA/JPL.

The details of the AIRSAR system parameters are given followed by figure 2.6 which is created over fertile farm ground that shows the contrast in crop, moisture, and soil compositions.

NASA's AIRSAR uses 3 different frequency channels and a number of modes to make complex mappings. AIRSAR is a collection of instruments mounted aboard a DC-8 passenger jet. The aircraft is a flying laboratory as seen in Figure 2.5 with racks of test and data acquisition equipment onboard. The system can operate in several modes with signals at the three frequencies of 0.45 GHz, 1.26 GHz, and 5.31 GHz, which are all produced from a single digital chirp generator [7]. The polarimetric SAR (POLSAR) mode uses both horizontal and vertical polarizations, and topographical SAR (TOPSAR) mode uses cross-track interferometry transmitting out of one or two antennas to produce topographical maps. The Along-track Interferometric mode has receive antennas separated horizontally to measure the ocean current movement.

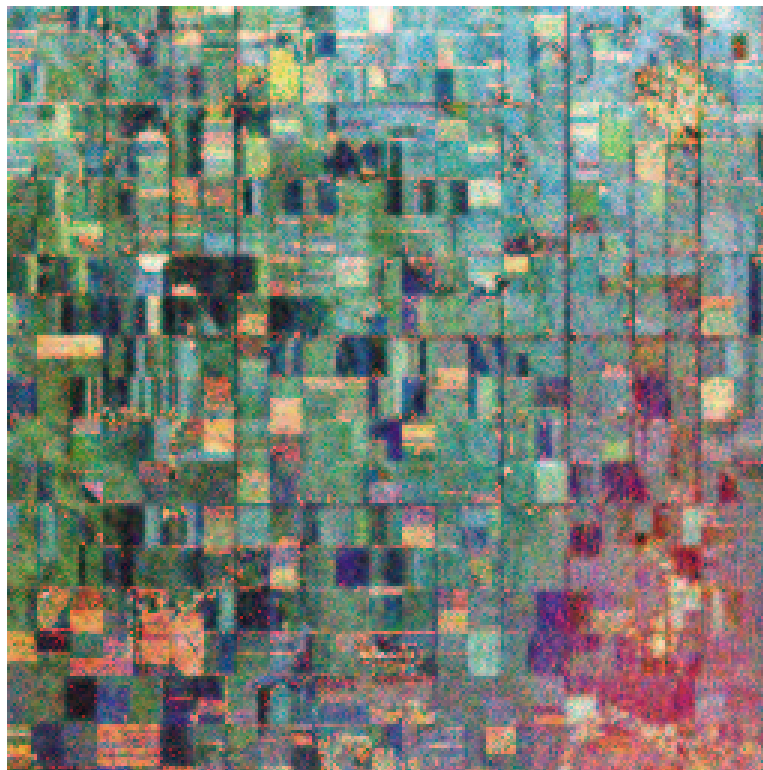


Figure 2.6: AIRSAR image taken over Altona, Manitoba, Canada with the P, L, and C bands mapped with red, green, and blue respectively. Contrast between crop types, moisture content, and soil mixture are visible by the use of multiple penetrating depth wavelengths mapped to different colors . Courtesy of NASA/JPL.

The system has range resolutions of 7.5, 3.75 and 1.875 m corresponding to the P,L, and C bands, and an azimuth resolution of 1 m. The power consumption is 1, 6, and 2 kW for the P,L, and C bands respectively. The aircraft's imaging altitude is normally 8 km, and it travels at 231 m/s. The swath widths vary from 10 km to 17 km imaging  $235 \text{ km}^2/\text{min}$  [7]. The processing onboard this aircraft is real-time, allowing the image to scroll out while the data is collected. The precise location and orientation of the aircraft is required to process the data correctly and generate accurate DEMs. The aircraft uses several inertial navigation systems and global position systems to locate the antennas. This SAR system costs approximately \$10,000,000.

The penetration depth of an electromagnetic wave into a material is proportional to the wavelength of the radar signal [1]. By using three wavelengths the system is able to penetrate the soil at several depths allowing soil profiling. This information is useful in understanding the effects of farming techniques. Figure 2.6 shows an image taken over Altona, Manitoba, Canada that is located in the floodplain of the Red River. The image comprises data taken from all three channels that is transmitted and received in the vertical polarization. P, L, and C band data corresponds to red, green and blue respectively, yielding an information-rich map. Differences due to crop type, moisture content and soil state are all detectable to the trained eye allowing scientists to make assessments of agricultural practices. In turn they may inform farmers and ranchers allowing them to use better crop and range management practices.

### **2.2.3 Intermap's STAR-3i**

The STAR-3i system was developed at a the Environmental Research Institute of Michigan (ERIM) and later purchased by Intermap technologies to produce commercial DEMs. The aircraft and several products generated from STAR-3i data are shown.

ERIM and Horizons Inc. spent \$30 million to develop a 9.57 GHz interferometric SAR specifically designed to create large DEMs. The system is integrated



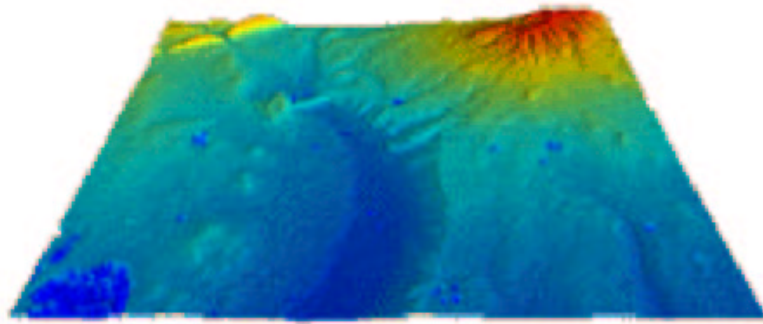


Figure 2.7: ERIM's 9.57 GHz Interferometric SAR mounted aboard a Learjet 36 costing \$30 million in development. Intermap Technologies commercialized the system investing another \$3 million.

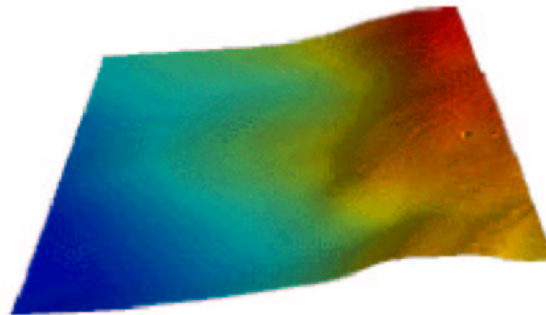
into a Learjet 36 with a heat control radome located at the bottom of the aircraft as seen in Figure 2.7, and is able to image over  $100 \text{ km}^2/\text{min}$  flying at 200 m/s. The aircraft's altitude can range from 6.15 to 12.3 km while imaging, and produces swaths 10 km wide. The image resolution may vary from 2.5m x 2.5m to 10m x 10m and the absolute elevation and horizontal position accuracy is 1.5 - 3m, and 2 - 3m respectively [8]. The data is post-flight processed on a ground based workstation system.

In 1996 Intermap Technologies Ltd. of Calgary, Alberta, Canada commercialized the system and obtained exclusive rights from ERIM and DARPA (Defense Advanced Projects Agency) and spent another \$3 million in upgrades [9]. Intermap produces a number of products similar to those already discussed. Another product of interest is their GEOID referenced elevation maps.

The earth is an ellipsoid in shape, and elevation measurements are referenced to the mean sea level. Inland it is more difficult to calculate the elevation exactly. GPS systems measurements are referenced to the ellipsoid surface and this surface



(a) Denver DEM



(b) Denver Local GEOID

Figure 2.8: Figure (a) shows a DEM of Denver Colorado created using SAR data and an ellipsoid earth model. Figure (b) shows the GEOID undulation in the Denver local which must be used with the DEM in Figure (a) to get the correct elevation with respect to the mean sea level. The images are not on an equal scale.

has no physical meaning [10]. The GEOID map is based on the physical property that water flows from a higher to lower potential on the GEOID, this is also the basis for topographical maps. Intermap claims that their instrument is the only system that can simultaneously create a DEM and then compute the GEOID, making their data useful for the design of canals and dams, and the assessment of flood plain risks [11].

Figure 2.8 (a) shows a DEM of the Denver, Colorado area and Figure 2.8 (b) shows the difference between the ellipsoid and GEOID. There is a high probability

that water would not flow in the direction intended if a canal were built in this area only using GPS measurements. Quick feasibility studies can be carried out for various hydro projects by the use of airborne SAR and its associated byproducts. Intermap plans to map the entire United States in the next three years [11].

#### 2.2.4 BYU's SAR Program

The BY $\mu$ SAR design described in this thesis follows on the success of three other BYU SAR systems. The development of each system is outlined and several images that they have generated are shown. The Microwave Earth Remote Sensing group at Brigham Young University has developed a number of unique SAR systems. The systems uniqueness stems from the fact that they were all developed on a small budget, and comprise some of the smallest SAR equipment in the world. In 1993 the group developed BYUSAR and later it developed YSAR and then an interferometric SAR, called YINSAR.

#### BYU SAR



Figure 2.9: Truck platform used to deploy BYUSAR

BYUSAR was developed in hopes to have an instrument capable of mapping archaeology sites. The system cost is approximately \$70,000 and transmits 1 Watt of power at 10 GHz. Processing is accomplished near real-time and achieves 2.5m x

0.45m resolution. The system is small enough to be mounted aboard a small aircraft and would be capable of imaging velocities of 168 m/s with near real-time processing [12]. Due to budget and time constraints the system has only been deployed on a truck platform shown in Figure 2.9.

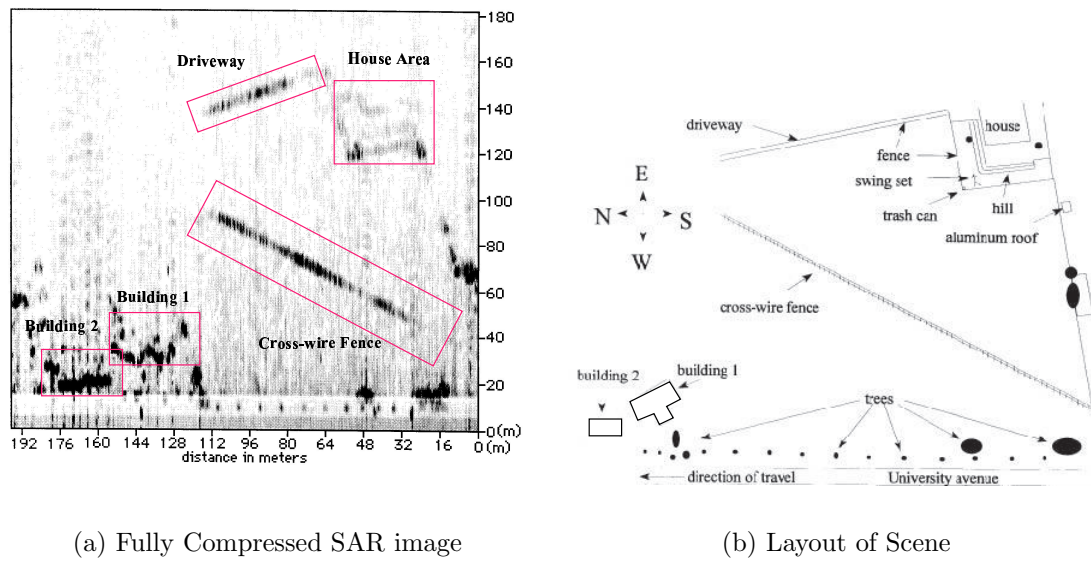


Figure 2.10: Figure (a) shows the fully compressed SAR image with significant features outlined. Figure (b) illustrates the layout of the scene.

Data was collected from a site east of University Avenue and 2230 North in Provo, Utah shown in Figure 2.10. The fully compressed image shows good detail highlighted by the significant features pointed out. An analysis of the range and azimuth resolutions shows that the radar achieves the resolution for which it is designed. Fuelled by this success the team moved onto the YSAR project.

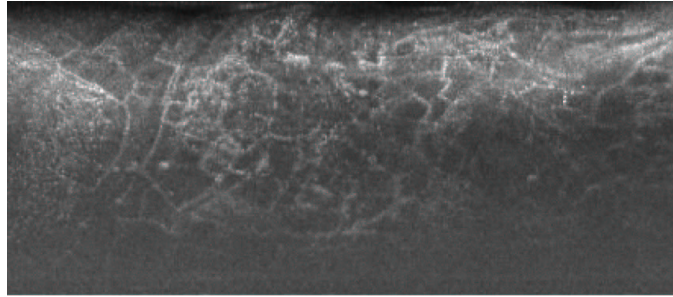
## YSAR

YSAR was designed specifically to target archaeological sites and so the frequency is lowered to 2.1 GHz for greater ground penetration [13]. Commercial parts

are used to design the majority of the system keeping the cost low. The platform for this system is a Lance Piper with imaging altitudes of 305 to 610 m [14, 15]. The overall system weighs 360 lbs with half of the weight in the battery pack.



(a) Photo of Tel Safi, Israel



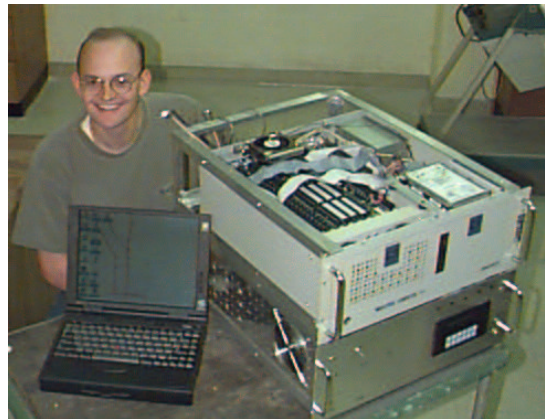
(b) 2.1 GHz SAR Image of Tel Safi

Figure 2.11: Figure (a) shows the photo of the area that is imaged with nothing resembling any order that is characteristic of civilizations. Figure (b) shows how long wavelengths are able to penetrate into the ground sufficiently to reveal the complex of walls, roads and foundations that lie below the surface of the landscape.

Data was collected in Israel at four sites, Zippori National Forest, Tel Safi, Tel Micnah, and Qumran. Some of the images are blurred due to air turbulence caused by upwellings off the Dead Sea. Figures 2.11(a) and 2.11(b) show the differences between photographs and SAR imagery at the Tel Safi site. The photo gives no indication that there is any kind of archeological significance to this area. By operating at a lower frequency the radar is able to penetrate deep enough into the soil to expose the ruins of a civilization. Walls, roads, and foundations are seen in the image that clearly outline the organization of the site. The blurring in the image can be corrected by using motion compensation, and this enhancement is made in the YINSAR project[14].



(a) Cessna 337 N Skymaster



(b) YINSAR Radar and Processing Boxes

Figure 2.12: Figure (a) shows the aircraft used to fly the YINSAR system. Figure (b) shows the YINSAR RF box and data acquisition system. The laptop is used to monitor the location of the aircraft and control the radar.

## YINSAR

BYU and Utah State University jointly own a Cessna 337 N Skymaster reconnaissance plane seen in Figure 2.12(a). By using a push and pull propeller system the plane is able to steer a straight course making it suitable for imaging [16]. The Skymaster flies at an imaging altitude of 305 to 610 m and a nominal velocity of 60 m/s. YINSAR images a 600m swath at  $2.16 \text{ km}^2/\text{min}$  with 1m by 0.5m resolution [17]. The system operates at 9.9 GHz with a peak transmit power of 10W and a total system power of 600 W. A differential GPS, kinematic GPS, and inertial measurement unit are used to obtain the precise location and motion of the aircraft. The entire system weighs 150 lbs and costs \$200,000.

The processing is post-flight, which integrates data from the motion detectors and the radar signals to generate well focused images with high resolution as seen in Figure 2.13. This image includes the Marriot Center on BYU campus in the left upper corner and the baseball stadium below it. Trees are apparent in this image





Figure 2.13: A YINSAR image of BYU campus with motion compensation applied.

but cars are more difficult to discern. The MERS program shows that SARs can be developed at a modest cost and still provide excellent image quality.

### 2.2.5 Basis for the $BY\mu$ SAR

A few SAR systems have been discussed and each of these systems are complementary in their functionality, but differ greatly in complexity and cost. High altitude sensors aboard satellites and spacecrafts like the X-SAR, have the capability to map out large tracks of land quickly with good resolution. Intermap Technologies has focused on acquiring large data sets at a rate of approximately 100 square km/min by using an high speed aircraft and post processing. Their system is costly and they only have one, thereby limiting the amount of real-time imaging available. BYU's YINSAR demonstrates that smaller systems are feasible and yield excellent resolution in azimuth, range, and elevation.

All of the previous systems outlined use pulsed FM technology. The  $BY\mu$ SAR is based on FM/CW technology that allows a compact, inexpensive design. Designing and building small, inexpensive radars has become feasible due to the advances in microwave electronics. The  $BY\mu$ SAR presented in this thesis operates at 9.9 GHz

with a bandwidth of 200 MHz. Its resolution is  $1.0 \times 0.2$  m, platform velocity is 60 m/s, and has a variable swath width of 300 to 600 m. It can be used at an elevation of 300 to 600 m and is capable of imaging  $2.16 \text{ km}^2/\text{min}$  making the performance the same as YINSAR. It only uses 1 mW of transmit power and consumes 12 W of system power. It weighs 10 lbs including the waveguide antennas, cost \$20,000 to develop, and the processing is accomplished post-flight using Matlab scripts. It does not have motion compensation and data is collected using a digital sampling oscilloscope, but these functions could be integrated into the design with minimal impact to size, weight and cost.

Unmanned Aerial Vehicles (UAVs) are now developed to the point that they are being used extensively by the military and commercial imaging companies. Small aircraft are only able to carry a small payload and provide a conservative amount of power. The technology used in  $\text{BY}\mu\text{SAR}$  is well suited for deployment on a UAV. A SAR mounted on a UAV is well suited for a large number of applications such as reconnaissance, terrain mapping, archeology, surveillance and surveying. Table 2.1 shows that the  $\text{BY}\mu\text{SAR}$  provides excellent resolution and has an advantage in size, cost, and low power in comparison to the other systems already presented.



Table 2.1: Comparison of Six SAR Systems with the BY $\mu$ SAR.

System/Parameters	X-SAR	AIR-SAR	STAR-3i	BYUSAR	YSAR	YINSAR	BY $\mu$ SAR
Center Frequency (GHz)	9.6	0.45, 1.26, 5.31	9.57	10	2.1	9.9	9.9
Resolution (m x m)	25x25	7.5-1.9	2.5-10	2.5x0.45	0.8x0.8	1x0.5	1x0.2
Platform Velocity (m/s)	N/A	231	200	168	N/A	60	60
Swath Width (m)	(20-70)k	(10-17)k	10k	N/A	600	300-600	300-600
Elevation (m)	225k	8k	(6-12)k	N/A	305-610	305-600	305-600
Transmit Power (W)	1.4k	(1-6)k	N/A	1	N/A	10	0.001
System Power (W)	(3-9)k	N/A	N/A	N/A	N/A	600	12
Imaging Rate ( $km^2/min$ )	17,000	235	100	N/A	N/A	2.16	2.16
Weight (lbs)	24,250	N/A	N/A	N/A	360	150	10
Cost (\$)	N/A	10M	30M	70k	N/A	200k	20k
Processing	Post	Realtime	Post	Near Real	Post	Post	Post

## Chapter 3

### FM/CW SAR Techniques

FM/CW has not been generally accepted as a technology capable of generating quality SAR images for remote sensing, although others have published on its uses for short range imaging [18, 19, 20, 21]. This chapter mathematically shows that FM/CW based SAR does not introduce artifacts that deteriorate the quality of the compressed image. This is done by first looking at the traditional use of FM/CW for range detection and resolution. Then SAR geometry in airborne systems is explained prior to an illustrative comparison of pulsed and CW SAR compression techniques. Investigation into the quality of range and azimuth compression when using FM/CW is made, and it is shown that FM/CW does not introduce significant phase errors. A guide for designing a FM/CW system is given, outlining limitations and optimizations.

#### 3.1 FM/CW Range Detection and Resolution

FM/CW is used in many systems that required range detection. The FM/CW signal is first described and then the parameters used to determine performance are identified. A simple example is shown illustrating the use of FM/CW to determine the range to a target, and followed by a proof that the range resolution is determined solely by the bandwidth of the FM/CW signal.

##### 3.1.1 Range Detection

FM/CW is chosen because it is a convenient way to increase SNR, while reducing the required system power level, complexity and cost. FM/CW is a continuous

wave (CW) radar that is frequency modulated (FM). This means that the source is not turned off and on like a pulsed system, but it is continuously modulated. Typically the modulation is linear in frequency, as shown in Figure 3.2. This ramp is also known as a chirp, named after the sound a bird makes when it increases the pitch of its call over a short period of time. FM/CW systems generally have a long period on the order of 1 to 10 ms where pulsed systems have a period on the order of 1  $\mu$ s.

The chirp is expressed as

$$f(t) = f_0 + \dot{f}t, \quad \text{where} \quad 0 \leq t \leq T. \quad (3.1)$$

$f_0$  is the initial frequency of the signal,  $\dot{f}$  is the chirp rate ( $\dot{f} = BW/T$ ), and  $T$  is the chirp period. The Pulse Repetition Frequency (PRF) is also specified as the rate at which the waveform repeats and for some systems this is the same as the chirp period. The transmit signal bandwidth  $BW$  is later shown to define the range resolution. The phase with respect to time is found by changing Equation 3.1 to radians and integrating. This results in

$$\phi(t) = \psi + \omega_0 t + \frac{\dot{\omega} t^2}{2}, \quad \text{where} \quad 0 \leq t \leq T, \quad (3.2)$$

and this includes the phase term  $\psi$  which models the initial phase of signal. The

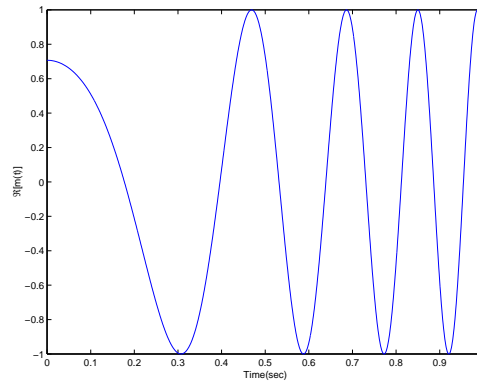


Figure 3.1: The Real Part of the Exponential Chirp  $m(t)$ .

phase expression is used in an exponential to represent the time domain waveform,

$$m(t) = e^{i\phi(t)}, \quad (3.3)$$

which is useful in radar analysis. Figure 3.1 is an illustrative plot of  $m(t)$  where  $\omega_0 = 0$ ,  $\dot{\omega} = 0.05$  and  $\psi = \pi/4$ .

The usefulness of a FM/CW signal is shown by a simple example of a single target. Figure 3.2 shows how a chirp may be used to measure the distance to an object. A chirp begins at  $t = 0$  sec and ends  $T$  sec later. The signal strikes a single target at a distance  $x$ , and reflects back to the receiver in  $t_0$  seconds. The frequency difference  $\Delta f$  is measured by the vertical separation of the transmit and receive signals. The distance  $x$  to the reflecting object is found using the similar triangle theorem as related in the equation

$$x = \frac{t_0 c}{2}, \quad \frac{\Delta f}{t_0} = \frac{BW}{T}, \quad x = \frac{c \Delta f T}{2BW}, \quad (3.4)$$

where  $c$  is the speed of light.

### 3.1.2 Range Resolution and Processing Gain

Here it is shown that range resolution is controlled by only one system variable, the transmit bandwidth  $BW$ . Processing gain is then demonstrated to be proportional to the chirp period, making FM/CW very desirable.

The range resolution of an arbitrary FM/CW system is based on the Rayleigh resolution criterion. The criterion states that two components of equal intensity should be considered to be just resolved when the first maximum from one component sits at the first minimum from the other, as illustrated in Figure 3.3(a) [22]. The distance between peaks is called the frequency resolution  $f_{res}$ .

The resulting signal from a FM/CW system is the superposition of sinusoidal signals. The Fourier transform a single sinusoid is a delta function. Consider two independent frequencies that are windowed in time by a rectangular window with a width equal to the chirp period  $T$  to determine the frequency resolution of a system.

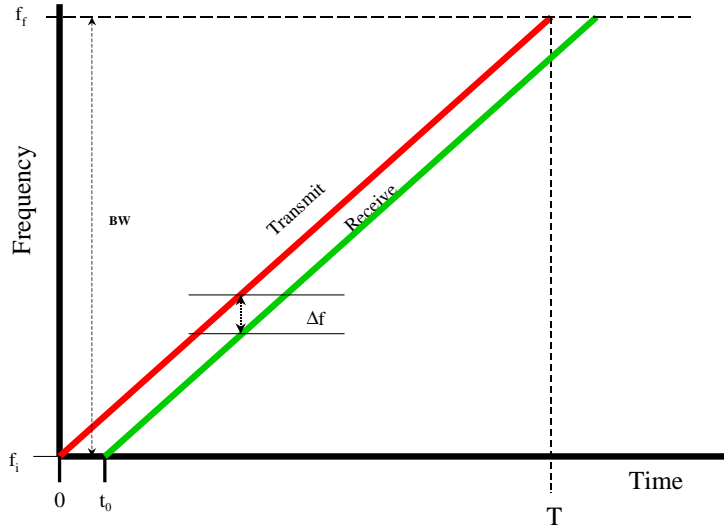


Figure 3.2: How a Chirp is Used to Measure Distance

Assume that  $t_o \ll T$  and then the frequencies are to be spaced apart such that the Rayleigh criterion is met. A rectangular window in the time domain transformed to the frequency domain becomes a sinc function. The peak to null spacing of sinc is  $1/T$  as illustrated in Figure 3.3(b) [23]. The Rayleigh criterion is met by placing the null of one signal at the same point in frequency as the peak of the other, thus the frequency resolution of this system is  $1/T$ .

It was just shown that the frequency resolution is  $f_{res} = 1/T$ . This frequency resolution is used to determine the range resolution  $\Delta R$  by using the relationships found in Equation 3.4. The resolution is solved by substituting  $\Delta R$  for  $x$  and  $1/T$  for  $\Delta f$  in Equation 3.4, which results in

$$\Delta R = \frac{c}{2BW}. \quad (3.5)$$

Pulse compression is a method used to enhance the range resolution of a system from its uncompressed result of  $1/T$ . The enhanced resolution  $\Delta t$  is obtained by chirping the pulse  $T$  over a large bandwidth  $BW$  [24]. This pulse compression is represented

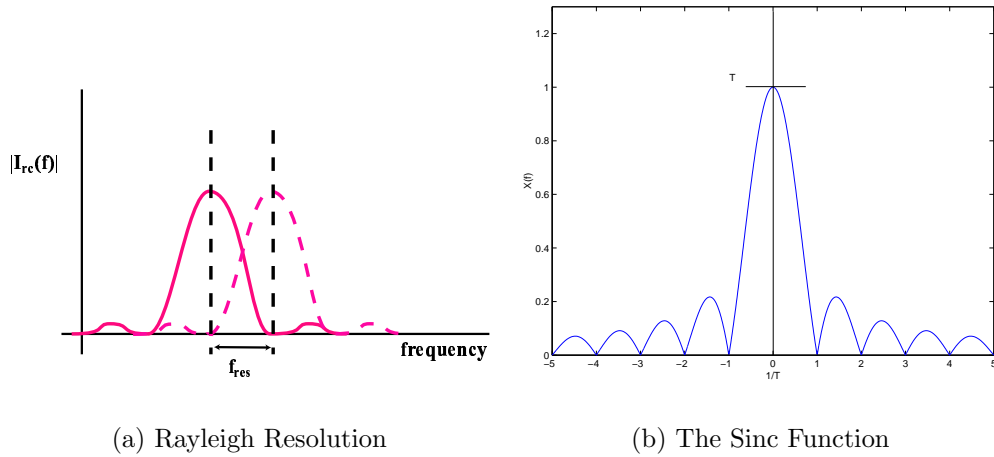


Figure 3.3: Subfigure (a) shows the Rayleigh Resolution Criterion for Fourier based frequency estimation. Subfigure (b) illustrates the sinc function that results from taking the Fourier transform of a rectangular window. The time window width determines both frequency resolution and processing gain.

by

$$\frac{T}{\Delta t} = BW \cdot T, \quad (3.6)$$

where  $\Delta t$  is the time resolution of the system. The time bandwidth product  $BW \cdot T$  indicates the ratio of pulse compression and the amount of SNR gain. A portion of this gain is achieved using techniques like the Fourier transform and the gain is proportional to the duration of the waveform  $T$ , as seen by the magnitude of the sinc in Figure 3.3 (b). Less transmit power is required because the signal is transmitted over a longer period of time. The remaining SNR gain is due to bandwidth reduction of the noise which is not coherent and is therefore reduced by pulse compression. The FM/CW technique is attractive for low probability intercept systems making the transmitter difficult to locate because it has low power output and a wide frequency sweep [25].

### 3.2 SAR Geometry

It is important to understand the geometric problem to see how a SAR image is generated. Variables are first defined based on the geometry of SAR and these are used in key equations that define resolution, range, imaging velocity and other sensor parameters. SAR images are traditionally generated using a moving radar platform and they may also be obtained for targets which move relative to the platform known as inverse SAR (ISAR). Whether the target or the platform is moving, the analysis is the same since the process is reciprocal. Here the approach will focus on a moving platform.

A narrow beamwidth transmit antenna focuses a periodic chirp signal perpendicular to the azimuth direction. The signal strikes targets limited to a small area on the ground called a footprint. The targets in the footprint reflect the energy back to the receive antennas mounted on the platform.

Figure 3.4 shows the geometry based upon an airborne platform which travels in the azimuth direction at a constant velocity  $v$  illuminating an array of targets over time resulting in a swath. The swath runs parallel to the azimuth direction, and its width  $S_{max}$ , is a function of the antenna's elevation beamwidth, platform elevation, baseband bandwidth, and system's SNR. The geometry relates the position of the platform to that of a single target as it passes through the aperture of the antenna.  $H$  denotes the platform's elevation above the target,  $R$  is range (horizontal distance), and  $R_s$  is the slant range or line of sight distance to the target.

Based upon the antenna's azimuth beamwidth  $\theta_a$ , a target appears in the aperture over a distance  $L$ . A high resolution image may be formed by processing the data and using the instantaneous position of the platform while a given target is in the aperture.

### 3.3 Illustrated SAR Compression

Traditional methods for SAR use a pulsed FM signal. A contrast between pulsed FM and FM/CW based SAR is made using several illustrations to provide a general overview of SAR compression techniques and how they differ. Pulsed FM

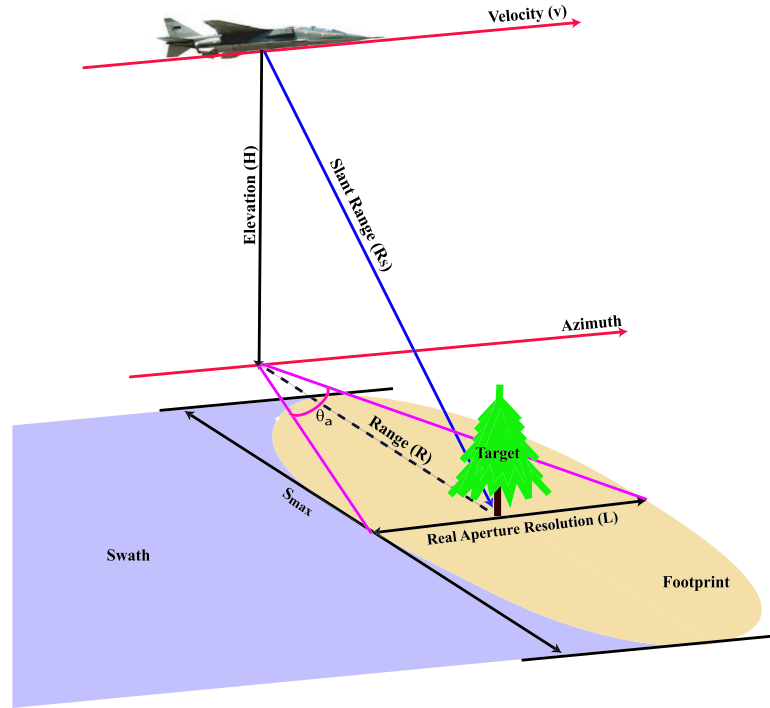


Figure 3.4: A SAR system moving in the azimuth direction at velocity  $v$ , and illuminating a target at range  $R$ .

processing is compared with the FM/CW technique pointing out key benefits and limitations. The digital processing for range compression is compared showing the end result to be essentially the same. Azimuth processing is pictorially explained by the use of several graphs showing range walk, phase response, Doppler frequency, and a final range and azimuth compressed image.

### 3.3.1 Pulsed FM SAR

Figure 3.5 shows the differences and similarities in the signal generation and processing between the traditional and FM/CW approach to SAR. Traditional SAR systems use a pulsed transmit signal  $S_{tr}$ , as shown in Figure 3.5(a) where the chirp has a short period  $T_{pulsed}$  resulting in the transmit signal beginning and ending before a reflected signal  $S_{rc}$  is ever received. The receive signal is down converted in Figure



3.5(b) to an intermediate frequency  $IF$  where it is sampled with a high speed analog to digital converter. As shown earlier, the bandwidth of the signal determines the resolution of the radar, so large bandwidths are desirable. The Nyquist sampling rate will be  $2(IF + BW)$ , and for many systems this is 500 MS/s or greater. Acquisition systems that operate at these frequencies are complicated and expensive.

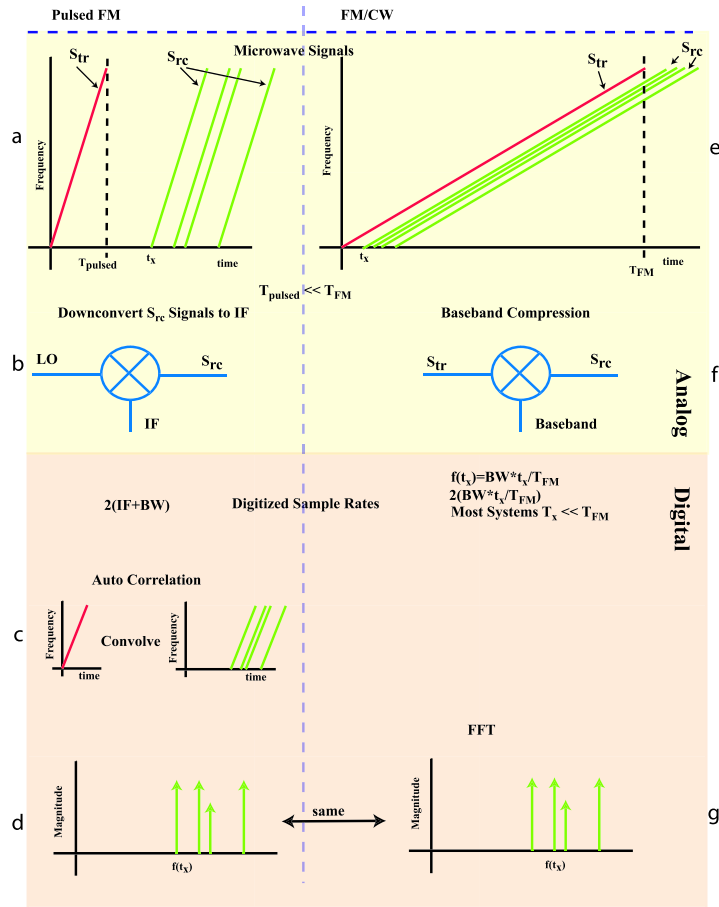


Figure 3.5: Comparison of Traditional SAR range compression in relation to the FM/CW approach. (a) shows the transmit and receive signals for FM pulsed systems, (b) illustrates the downconversion, and (c) shows the convolution of the transmit and receive signals. (d) is the final range compressed signal. (e) shows the relationship between the transmit and receive signals for FM/CW systems with a mixer performing the pulse compression as shown in (f). The final range compressed signal is the same for either system as shown in (d) and (g).

Once the pulsed FM SAR receive signal is digitized, it must be convolved with a matched filter that has the same impulse response as the down converted transmit signal as shown in Figure 3.5(c). Once convolved, the signal passes through a FFT as shown in Figure 3.5(d), where targets are now a function of frequency. This step completes the range compression of the FM pulsed signal.

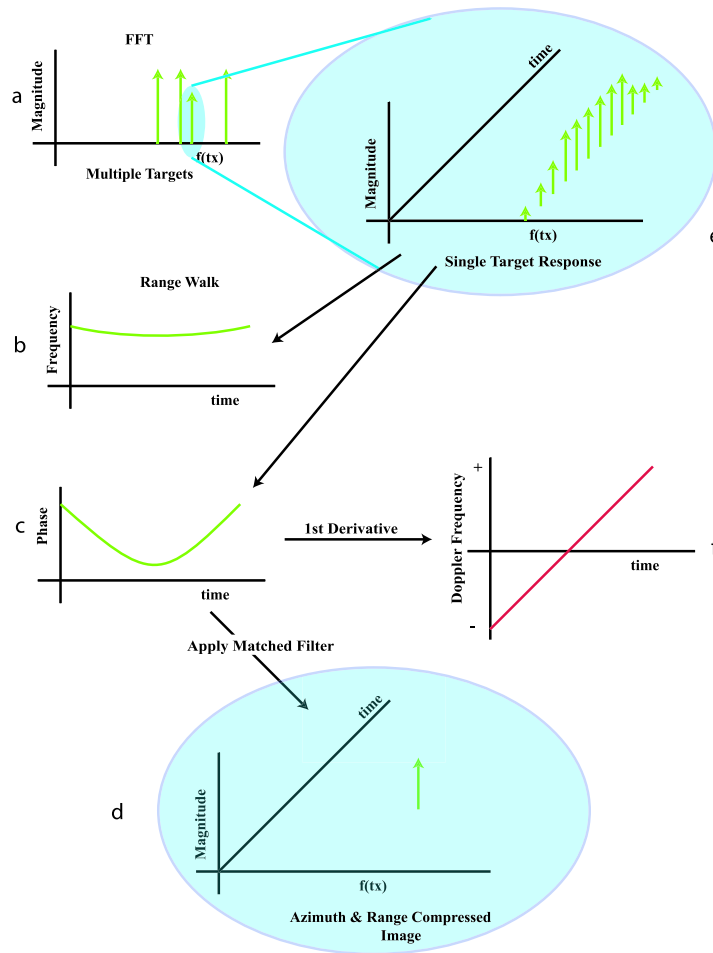


Figure 3.6: Azimuth compression of a single target using a matched filter. Subfigures (a) and (e) show the azimuth response of a single target. (b) and (c) show key quadratic effects due to the time-distance relationship between the target and radar platform. (f) shows that the first derivative of the phase is essentially linear thereby allowing a simple matched filter technique to be used to azimuth compress the image. A fully azimuth and range compressed image is shown in (d).

### 3.3.2 FM/CW SAR

The FM/CW technique shown in Figure 3.5(e) shows how the chirp period  $T_{FM}$  is extended such that transmit and receive signals overlap. Transmit power may be lowered due to the longer period that the signal is present contributing to processing gain. The required overlap of the transmit and receive signals has a limiting effect by making the SNR and range resolution dependant on range. The longer period also restricts the velocity of the radar platform for proper azimuth sampling.

The delay time  $t_x$  is the time it takes the transmit signal to travel to a target  $x$ , reflect, and travel back to the receiver. The transmit and receive signals are mixed using a microwave mixer to compress the signals to the baseband frequency in Figure 3.5(f). The baseband sample rate is dependent on range and is  $2BWt_x/T_{FM}$  where  $t_x$  is the delay time for the farthest target of interest. For most systems  $t_x \ll T_{FM}$  allowing the sample rates to be approximately 10 MS/s or less, and at these rates standard video data acquisition circuits are sufficient. In Figure 3.5(g) the baseband signal is passed through a FFT where the signal is fully range compressed. From this point the SAR processing is the same and produces almost equivalent results.

The radar will image a single target multiple times in a single pass. Figure 3.6(a) shows a single target being selected, and then displays the FFT results over time in Figure 3.6(e). The target appears small on the edge of the antenna beam, it appears large in the middle of the beam and remains large until it reaches the other edge of the beam where it drops off again. This is the azimuthal response of a target and the azimuthal antenna pattern. Linear range walk and parabolic phase response occur because the distance between the target and radar platform changes parabolically. Range walk results when a single target moves across range cells quadratically, as illustrated in Figure 3.6(b). This undesirable effect may be removed by the use of algorithms in the signal processing [26].

The second result is a parabolic phase response, illustrated in Figure 3.6(c). The frequency is found by taking the first derivative of the phase, which in this case

is the Doppler frequency. The Doppler frequency shown in Figure 3.6(f) is approximately linear with time so it now looks like the chirps used in range compression. An image is formed by applying the correct matched filter, and the image is then range and azimuth compressed and is illustrated as a single point in azimuth time and frequency in Figure 3.6(d). Mathematically it is later shown that both CW and pulsed FM yield essentially the same results.

### 3.4 Range Compression Techniques

A detailed comparison between the FM/CW compression and the traditional pulsed FM compression using the correlation function shows that differences occur due to windowing effects. A comparison of ranges from 1 - 140 km is shown in Figure 3.9 indicating that FM/CW SAR has good range capabilities. This analysis assumes that the radar platform is stationary relative to the target and thus eliminates the complex azimuth effects that are addressed later.

#### 3.4.1 FM/CW Range Compression

First, this derivation represents the time delay of a receive signal with a time constant  $t_o$  which ignores azimuth effects but gives a simple result to model the range compression. The final equation includes a convolution of the compressed signal with a window that models the limits of integration.

A transmitted LFM signal is first considered in the exponential form,

$$m_T(t) = e^{i(\psi + \omega_0 t + \frac{\dot{\omega} t^2}{2})} \quad \text{for} \quad 0 \leq t \leq T. \quad (3.7)$$

Each received signal will have a time delay  $\tau$  associated with the range of the reflecting target and an amplitude  $A(\tau)$  corresponding to the targets radar cross section. The signal is a summation of all the targets in the aperture of the antenna yielding the mathematical form

$$m_R(t) = \int_{-\infty}^{\infty} d\tau A(\tau) m_T(t - \tau). \quad (3.8)$$

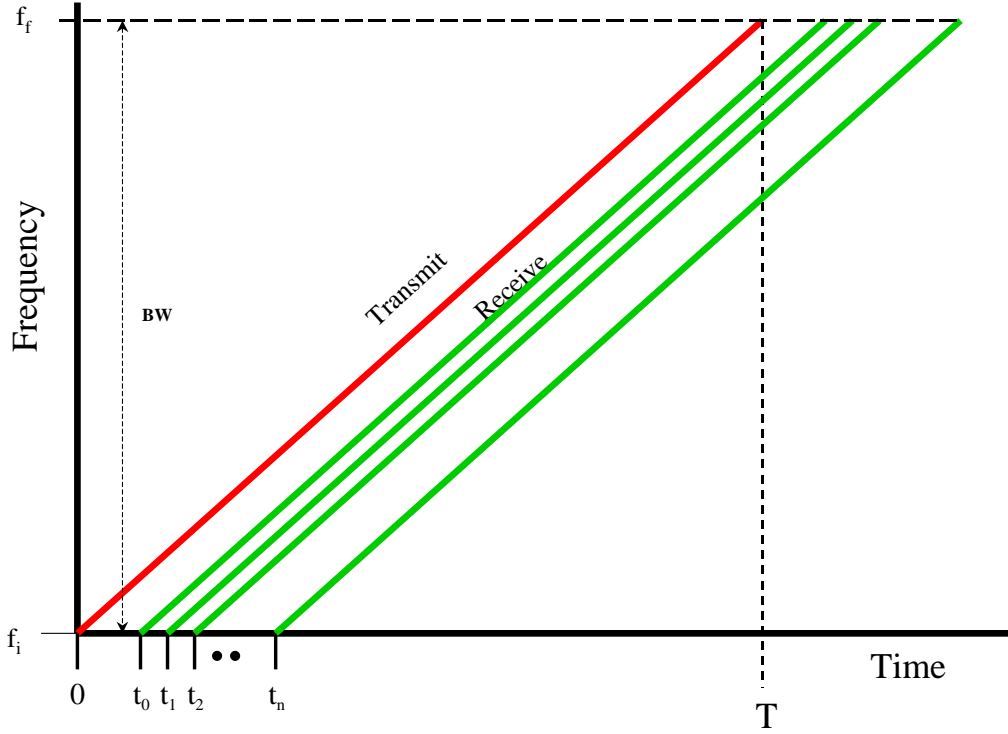


Figure 3.7: FM/CW Model of Transmitted and Return Signal Relationship.

Figure 3.7 shows the transmitted signal and the delayed copies that return from respective ranges. Data acquisition time is limited between  $t_0$  to  $T$  because the hardware implements range compression. This processing is accomplished by mixing the transmitted and received signals followed by a lowpass filter. Mathematically this is a multiplication of Equation 3.7 and the complex conjugate of Equation 3.8 resulting in the range compressed signal

$$i_{RC}(t) = m_T(t)m_R^*(t), \quad (3.9)$$

$$= e^{i(\psi + \omega_0 t + \frac{\dot{\omega} t^2}{2})} \int_{-\infty}^{\infty} d\tau A^*(\tau) e^{-i(\psi + \omega_0(t-\tau) + \frac{\dot{\omega}(t-\tau)^2}{2})}, \quad (3.10)$$

$$= \int_{-\infty}^{\infty} d\tau A^*(\tau) e^{i(\omega_0 \tau + \dot{\omega} \tau t - \frac{\dot{\omega} \tau^2}{2})}. \quad (3.11)$$

Now consider the response of a single target at a delayed time of  $t_o$

$$i_{RC}(t) = A^*(t_o)e^{i(\omega_0 t_o + \dot{\omega} t_o t - \frac{\dot{\omega} t_o^2}{2})}. \quad (3.12)$$

Here the limits of integration are ignored, but are later used to construct a rectangular window.  $i_{RC}(t)$  is then lowpass filtered, for anti-aliasing and for a higher SNR, and then digitized. Using Nyquist criterion the compressed signal is sampled at a frequency greater than twice the highest  $i_{RC}$  frequency content. The highest frequency is determined by the farthest range of interest and should be the same as the lowpass filters corner frequency. An ideal lowpass filter is a rectangular window in the frequency domain .

By using the Fourier Transform the range compressed signal,  $I_{RC}(\omega)$  is found as follows,

$$I_{RC}(\omega) = \int_{-\infty}^{\infty} dt A^*(t_o) e^{i(\omega_0 t_o + \dot{\omega} t_o t - \frac{\dot{\omega} t_o^2}{2})} e^{-i\omega t}, \quad (3.13)$$

$$= A^*(t_o) e^{i(\omega_0 t_o - \frac{\dot{\omega} t_o^2}{2})} \int_{-\infty}^{\infty} dt e^{i\dot{\omega} t_o t} e^{i\omega t}, \quad (3.14)$$

$$= A^*(t_o) e^{i(\omega_0 t_o - \frac{\dot{\omega} t_o^2}{2})} 2\pi \delta(\dot{\omega} t_o - \omega). \quad (3.15)$$

The limits of integration are now considered. The FM/CW window left hand limit will shift as there will only be a signal present from time  $\tau$  to time  $T$  leading to

$$W_{CW}(\omega) = \begin{cases} (T - t_o) e^{-j\omega \frac{T-t_o}{2}} \text{sinc}(\omega(T - t_o)/2) & \text{if } t_o < T, \\ 0 & \text{if } 0 > t_o \text{ or } t_o > T. \end{cases} \quad (3.16)$$

The window in Equation 3.16 is convolved with the result in Equation 3.15 to produce the complete range compressed signal,

$$I_{CW}(\omega) = \int_{-\infty}^{\infty} dx I_{RC}(\omega - x) W_{CW}(x) \quad (3.17)$$

$$= \int_{-\infty}^{\infty} dx A^*(t_o) e^{i(\omega_0 t_o - \frac{\dot{\omega} t_o^2}{2})} 2\pi \delta(\dot{\omega} t_o - \omega - x) \\ (T - t_o) e^{-jx \frac{T-t_o}{2}} \text{sinc} \left( x \frac{T-t_o}{2} \right) \quad (3.18)$$

$$= 2\pi(T - t_o) A^*(t_o) e^{i(\omega_0 t_o - \frac{\dot{\omega} t_o T}{2} + \frac{\omega(T-t_o)}{2})} \\ \text{sinc} \left( (\dot{\omega} t_o - \omega) \frac{T-t_o}{2} \right). \quad (3.19)$$

Several significant results are found in Equation 3.19. First the signal level is proportional to the term  $(T - t_o)$  indicating that more energy is received with a larger chirp period  $T$ , and that farther ranged targets have a diminished power level. The argument of the sinc function  $(\dot{\omega} t_o - \omega) \frac{T-t_o}{2}$  produces the second result. The  $\dot{\omega} t_o - \omega$  term shifts the center of the sinc function and the shift is dependant on the magnitude of  $\dot{\omega} t_o$ . The  $\frac{T-t_o}{2}$  term determines the width of the sinc function and in turn the resolution of the system. It is shown in section 3.1.2 how this resolution translates to the range resolution of the system. It is also seen that larger ranges will degrade the range resolution as the sinc function broadens when  $\frac{T-t_o}{2}$  becomes smaller.

### 3.4.2 Pulsed FM Range Compression

FM Range compression is the traditional method for generating SAR images in remote sensing applications. The following derivation parallels Robertson's analysis of the YINSAR autocorrelation range compression [3]. The development is reduced to a single sideband chirp rather than a dual side band which Robertson developed because a single sideband represents the type of modulation used in the BY $\mu$ SAR. A similar notation as Robertson's is used so that the two derivations may be easily compared, and then several substitutions allow the final result to be expressed in a comparable form to Equation 3.19.

The transmit and receive signals are respectively,

$$x_t(t) = \frac{1}{2}\cos(\omega_c t + \beta t^2), \quad (3.20)$$

$$x_r(t) = A(t_o)\frac{1}{2}\cos(\omega_c(t - t_o) + \beta(t - t_o)^2), \quad (3.21)$$

where  $\beta = BW\pi/T$ . In hardware the signal is mixed down and low pass filtered to a intermediate frequency of  $\omega_d$ . Mathematically this is

$$m_{if}(t) = x_r(t) \otimes \cos(\omega_d t), \quad (3.22)$$

$$= A(t_o)\frac{1}{2}\cos(\omega_c(t - t_o) + \beta(t - t_o)^2)\cos(\omega_d t), \quad (3.23)$$

$$= A(t_o)\frac{1}{4}[\cos(\omega_c(t - t_o) + \beta(t - t_o)^2 - \omega_d t) + \cos(\omega_c(t - t_o) + \beta(t - t_o)^2 + \omega_d t)].$$

Applying the lowpass filter,

$$= A(t_o)\frac{1}{4}\cos(\omega_c(t - t_o) + \beta(t - t_o)^2 - \omega_d t). \quad (3.25)$$

At this point the signal is digitized and processed. Robertson points out that the remaining derivation may be done in the continuous time domain if the data is sample above Nyquist rate [3]. Next the Hilbert transform is applied letting  $\omega_c - \omega_d = \omega_o$ ,

$$m_{if}(t) = A(t_o)\frac{1}{4}e^{j(\omega_c(t-t_o)+\beta(t-t_o)^2-(\omega_c-\omega_o)t)}, \quad (3.26)$$

$$= A(t_o)\frac{1}{4}e^{j(\omega_o t + \beta(t-t_o)^2 - \omega_c t_o)}. \quad (3.27)$$

The Nyquist sample is found by looking at the phase,  $\phi(t)$ , and differentiating.

$$\phi = \omega_o t + \beta(t - t_o)^2 - \omega_c t_o, \quad (3.28)$$

$$\dot{\phi} = \omega_o + 2\beta(t - t_o), \quad (3.29)$$

and the maximum frequency will occur when  $t - t_o = T$ , thus the minimum sampling rate  $AtoDmin$  must be at least  $2(f_o + BW)$ .



Assuming a infinite length matched filter of the form,

$$h(t) = e^{j(\omega_0 t + \beta t^2)}, \quad (3.30)$$

due to the large period  $T$ . The autocorrelation function is used to extract the range compressed image  $m(t)$ ,

$$m(t) = m_{if}(t) \otimes h^*(t), \quad (3.31)$$

$$= \int_{-\infty}^{\infty} m_{if}(t + \tau) h^*(\tau) d\tau, \quad (3.32)$$

$$= A(t_0) \frac{1}{4} \int_{-\infty}^{\infty} e^{j(\omega_0(t+\tau) + \beta(t-t_0+\tau)^2 - \omega_c t_0)} e^{-j(\omega_0 \tau + \beta \tau^2)} d\tau, \quad (3.33)$$

$$= A(t_0) \frac{1}{4} e^{j(\omega_0 t + \beta(-2t t_0 + t_0^2 + t^2) - \omega_c t_0)} \int_{-\infty}^{\infty} e^{j\beta(2t\tau - 2t_0\tau)} d\tau, \quad (3.34)$$

applying limits of integration,

$$= A(t_0) \frac{1}{4} e^{j(\omega_0 t + \beta(t-t_0)^2 - \omega_c t_0)} \int_{-t+t_0}^{T-t+t_0} e^{j2\beta\tau(t-t_0)} d\tau, \quad (3.35)$$

$$= A(t_0) \frac{1}{4} \frac{e^{j(\omega_0 t + \beta(t-t_0)^2 - \omega_c t_0)}}{2j\beta(t-t_0)} (e^{2j\beta(T-t+t_0)(t-t_0)} - e^{2j\beta(-t+t_0)(t-t_0)}), \quad (3.36)$$

$$= A(t_0) \frac{1}{4} \frac{e^{j\omega_0 t - j\omega_c t_0}}{2j\beta(t-t_0)} (e^{2j\beta T(t-t_0)} e^{-j\beta(t-t_0)} - e^{-j\beta(t-t_0)}), \quad (3.37)$$

$$= A(t_0) \frac{1}{4} \frac{e^{j\omega_0 t - j\omega_c t_0}}{\beta(t-t_0)} e^{j\beta T(t-t_0)} \sin(\beta T(t-t_0)) e^{-j\beta(t-t_0)}, \quad (3.38)$$

$$m(t) = A(t_0) \frac{T}{4} e^{j\omega_0 t - j\omega_c t_0} e^{j\beta(t-t_0)(T-1)} \text{sinc}(\beta T(t-t_0)). \quad (3.39)$$

The last equation reveals the sinc effect due to the autocorrelation. The width of the sinc is independent of the range dependant time  $t_0$ , but is inversely proportional to the bandwidth of chirp. The direct implication is that the range resolution is a function of bandwidth and not the chirp period as shown in Section 3.1.2. The  $T/4$  term at the beginning of the equation indicates the SNR of the signal is a direct function of the chirp period, and increases with the period as was also shown.

Two differences in the range compression derivations must be pointed out in order to contrast the two solutions. First, the pulsed solution has an intermediate

frequency  $\omega_d$ , which is zero in the FM/CW case. Second, the CW result is in the frequency domain while the pulsed result is in the time domain.

By making the following substitutions the CW and pulsed solutions converge with slight, yet significant differences:

$$2\beta = \dot{\omega}, \quad (3.40)$$

$$\omega_d = 0, \quad (3.41)$$

$$(3.42)$$

The autocorrelation is carried out using

$$m(t) = \int_{-\infty}^{\infty} m_{if}^*(\tau)h(t + \tau)d\tau, \quad (3.43)$$

and ignoring the limits of integration. Also applying the Fourier transform yields exactly the same result for Equation 3.15 as found in the CW solution. This implies that the difference in the two solutions lies in the window functions due to integration limits. The window from the pulsed system has the limits  $\tau = (-t + t_0, T - t + t_0)$  that results in the window

$$W_{ac}(\omega) = Te^{-i\omega(t_0 + \frac{T}{2})} \text{sinc}(\omega T/2). \quad (3.44)$$

The window is convolved with Equation 3.12:

$$I_{Pulsed}(\omega) = \int_{-\infty}^{\infty} dx I_{RC}(\omega - x)W_{ac}(x) \quad (3.45)$$

$$= \int_{-\infty}^{\infty} dx A^*(t_o) e^{i(\omega t_o - \frac{\dot{\omega} t_o^2}{2})} 2\pi \delta(\dot{\omega} t_o - \omega - x) \\ T e^{-ix(t_o + \frac{T}{2})} \text{sinc}\left(x \frac{T}{2}\right) \quad (3.46)$$

$$= 2\pi T A^*(t_o) e^{i(\omega t_o + \omega t_o - \frac{3\dot{\omega} t_o^2}{2} - \frac{\dot{\omega} t_o T}{2} + \frac{\omega T}{2})} \\ \text{sinc}\left((\dot{\omega} t_o - \omega) \frac{T}{2}\right). \quad (3.47)$$

### 3.4.3 Range Compression Contrast

The two range compressed solutions are contrasted by making them both a function of range. Representing the frequency  $\omega(R_s) = 2\dot{\omega}R_s/c$  and the time delay to the target  $t_o = 2R_{s,o}/c$  as a function of slant range allows the range compressed signals to reduce to the forms

$$I_{CW}(R_s) = 2\pi \left(T - \frac{2R_{s,o}}{c}\right) A^* \left(\frac{2R_{s,o}}{c}\right) e^{i\left(\frac{2\omega_o R_{s,o}}{c} - \frac{\dot{\omega} R_{s,o} T}{c} + \frac{\dot{\omega} R_s}{c} \left(T - \frac{2R_{s,o}}{c}\right)\right)} \text{sinc} \left(\frac{\dot{\omega}}{c} \left(T - \frac{2R_{s,o}}{c}\right) (R_{s,o} - R_s)\right), \quad (3.48)$$

$$I_{Pulsed}(R_s) = 2\pi T A^* \left(\frac{2R_{s,o}}{c}\right) e^{i\left(\frac{2\omega_o R_{s,o}}{c} + \frac{4\dot{\omega} R_{s,o} R_s}{c^2} - \frac{6\dot{\omega} R_{s,o}^2}{c^2} - \frac{\dot{\omega} R_{s,o} T}{c} + \frac{\dot{\omega} R_s T}{c}\right)} \text{sinc} \left(\frac{\dot{\omega} T}{c} (R_{s,o} - R_s)\right). \quad (3.49)$$

Equation 3.48 is compared to a computer simulated response for a target 7.3 m away in Figure 3.8. The effective width of the sinc waveform in both plots is 0.75m comparing to the slant range resolution  $\Delta R_s$ . The null to null width differs slightly with the mathematical model measuring  $2\Delta R_s$  and the simulation slightly less. The plots for the pulsed FM model and associated simulation are almost identical to the FM/CW model at 7.5m. As predicted earlier this changes with range as shown in Figure 3.9.

The plots in Figure 3.9 assume a FM/CW chirp period of 1 ms and a pulsed period of 1  $\mu s$ . The transmit power level of the pulsed system is raised to a sufficient level to make the compressed signal level at 1 km the same. The effects of power drop due to range in the radar equation are ignored. The range resolution and SNR are both strongly effected when targets are approximately a hundredth (10 $\mu s$ ) of the chirp period (1ms) away, thereby limiting the effective range of the radar. The range resolution effect is determined by the  $(T - 2R_{s,o}/c)$  term in the sinc function. The processing gain drop is due to the multiplicative term  $(T - 2R_{s,o}/c)$  found at the beginning of the window. When using auto correlation each of these terms are simply

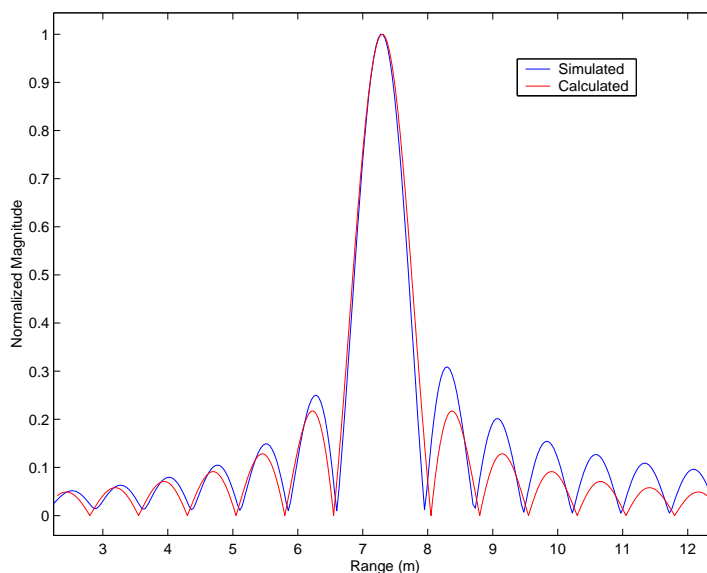


Figure 3.8: The CW mathematical model is compared with a computer simulation of a target 7.5m away. The range resolution for both is approximately 0.75m, which is predicted by the range resolution estimation.

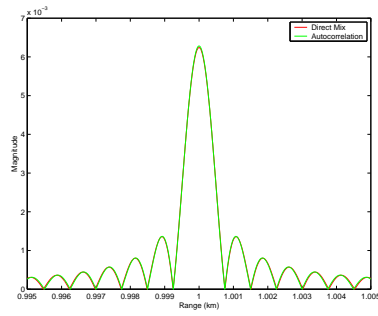
equal to  $T$  thus providing no degradation in processing gain or resolution as a function or range.

### 3.5 Azimuth Compression

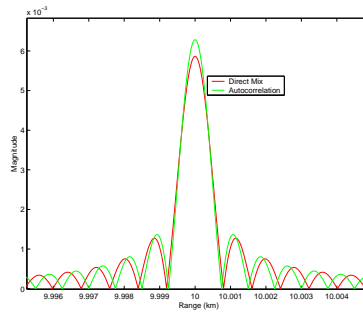
This section derives an azimuth compression matched filter and performs an analysis to determine whether FM/CW SAR introduces phase errors. The analysis shows that the FM/CW and pulsed FM azimuth compression results are essentially the same with discrepancies appearing in a slight linear shift in rangewalk. A quality FM/CW SAR system can be designed based on the results that are derived and analyzed in this section.

#### 3.5.1 Derivation

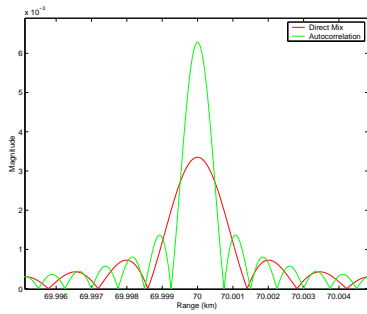
This derivation simplifies the azimuth problem by noting that the phase is quadratic. A quadratic phase is linear in frequency so the same techniques can be used to derive a range-dependent matched filter as is in the range compression derivation.



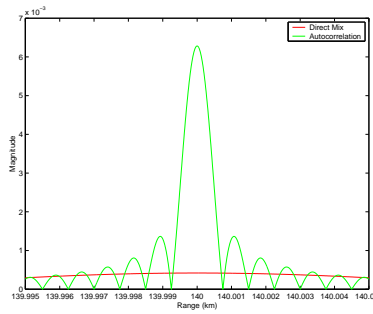
(a) Single Target at 1 km with a time delay  $t_o = 6.67\mu\text{sec}$



(b) Single Target at 10 km with a time delay  $t_o = 66.7\mu\text{sec}$



(c) Single Target at 70 km with a time delay  $t_o = 0.48\text{msec}$



(d) Single Target at 140 km with a time delay  $t_o = 1\text{msec}$

Figure 3.9: Mathematical model of single targets showing both SNR and resolution degradation. The transmit power level of the autocorrelated signal is 30 dB greater than the FM/CW level which shows the great power advantage of an FM/CW system.

A positive Doppler shift is added to the return signal as a SAR platform approaches a target, decreases to zero shift at boarside, and then receives a negative Doppler shift as the platform moves away from the target. The phase change  $\phi_D$  of the received signal is associated with the change in range  $\delta r$  from platform to target

due to the platform's velocity as modelled by [26],

$$\phi_D = \frac{4\pi f \delta r}{c} \quad (3.50)$$

$$= \frac{4\pi \delta r}{\lambda}. \quad (3.51)$$

Figure 3.10 shows the relationship required to find the range difference  $\delta r$  between

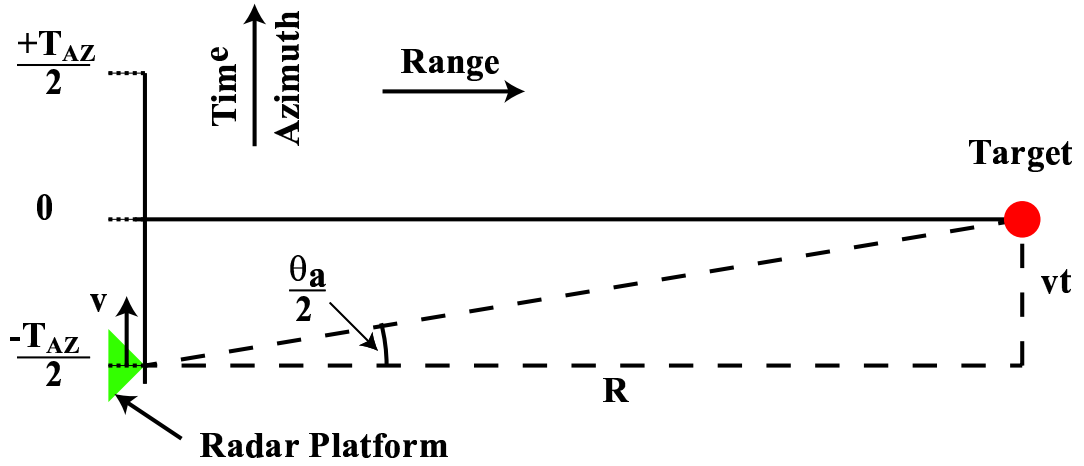


Figure 3.10: Distance Relationship of Moving Platform and a Single Target.

the projected slant range  $R_{ps}$  and image range  $R$ . First solving for  $R_{ps}$  in terms of  $vt$  and  $R$ ,

$$R_{ps} = \sqrt{(vt)^2 + R^2}, \quad (3.52)$$

$$\approx R + \frac{(vt)^2}{2R}, \quad (3.53)$$

$$\delta r \approx \frac{(vt)^2}{2R}. \quad (3.54)$$

Equation 3.53 is found by assuming that  $vt < R$  and using the Taylor expansion approximation,

$$\sqrt{1+x} \approx 1 + \frac{x}{2} \quad \text{where} \quad x \ll 1, \quad (3.55)$$

and the error is  $x^2/4$ . Substituting  $\delta r$  into Equation 3.51 yields

$$\phi_D(t) = \frac{2\pi v^2 t^2}{\lambda R}. \quad (3.56)$$

This time dependent phase may be considered an azimuth chirp by noticing the phase is quadratic in time. Thus parameters such as bandwidth, chirp rate, and period may be found to enable azimuth compression [27]. The azimuth frequency  $f_{az}$  is found by differentiating the phase

$$f_{az} = \frac{2v^2 t}{\lambda R}, \quad (3.57)$$

and thus the azimuth chirp rate is found to be

$$\dot{f}_{az} = \frac{2v^2}{\lambda R}. \quad (3.58)$$

The azimuth bandwidth  $BW_{AZ}$  may be solved for by using the previously defined chirp rate  $\dot{f} = BW/T$  and extending this notion to the azimuth parameters. First the azimuth period  $T_{AZ}$  must be derived, and it is shown that the period is dependent on the range of the target. From Figure 3.10 it is seen that

$$\tan(\theta_a/2) = \frac{vT_{az}}{2R}. \quad (3.59)$$

Using the small angle approximation  $\tan(\theta_a/2) \approx \theta_a/2$ , the azimuth period can be solved for, where

$$T_{az} = \frac{\theta_a R}{v}. \quad (3.60)$$

The azimuth bandwidth is defined by

$$BW_{az} = \dot{f}_{az} T_{az}, \quad (3.61)$$

$$= \frac{2v^2 \theta_a R}{\lambda R v}, \quad (3.62)$$

$$= \frac{2v\theta_a}{\lambda}. \quad (3.63)$$

The minimum pulse repetition frequency  $PRF_{min}$  must meet the Nyquist criterion which is twice the azimuth bandwidth, namely

$$PRF_{min} = \frac{4v\theta_a}{\lambda}. \quad (3.64)$$

The derivation continues using the fact that the resolution is related to the velocity of the platform and the signal bandwidth by

$$\Delta a = \frac{v}{BW_{az}}, \quad (3.65)$$

$$= \frac{\lambda}{2\theta_a}, \quad (3.66)$$

$$= \frac{d}{2}, \quad (3.67)$$

where  $d$  is the physical dimension of the antenna in the azimuth direction. The last equation also makes use of the antenna beamwidth approximation  $\theta_a = \lambda/d$ . This allows the azimuth LFM signal to be expressed as a function of the system parameters,

$$m_{az}(t) = A \text{rect} \left| \frac{t}{T_{AZ}} \right| e^{\frac{j}{2}(2\pi f_{az})t^2}, \quad (3.68)$$

$$= A \text{rect} \left| \frac{t}{\frac{\lambda R}{2\Delta av}} \right| e^{j(\frac{2\pi v^2}{\lambda R})t^2}. \quad (3.69)$$

A separate matched filter must be used for each range due to the filters dependence on range. The azimuth matched filter  $h_{az}(t)$  is simply the conjugate of the azimuth signal such that

$$h_{az}(t) = A \text{rect} \left| \frac{t}{\frac{\lambda R}{2\Delta av}} \right| e^{-j(\frac{2\pi v^2}{\lambda R})t^2} \quad (3.70)$$

### 3.5.2 FM/CW Phase Error Analysis

The following analysis proves that a properly designed FM/CW SAR system will generate images that are properly compressed in both range and azimuth. The range compression now accounts for the Doppler shift. Several approximations must be used in order to simplify the complexity of the compression transforms. This results



in a solution that shows that there is minimal phase error introduced by FM/CW. The analysis also shows that a linear rangewalk term dependent on the chirp period  $T$  becomes more significant for longer periods. Equations are given to calculate the amount of frequency shift expected for a set of system parameters and the amount of phase error that is to be considered due to the approximations made.

The azimuth imaging is dependent upon the phase information obtained from the range compression. SAR is restricted to having enough azimuth samples per second in order to meet the Nyquist sampling criterion for azimuth compression. SAR systems generally are designed with a short pulse of energy typically on the order of  $1\mu s$  in duration. With FM/CW the duration is lengthened in order to achieve a direct mix between transmit and receive signals in hardware. As shown earlier, the pulse must be sustained long enough to achieve adequate SNR and range resolution, and in the BY $\mu$ SAR the period is designed to be 1 ms. It is shown that azimuth compression is not adversely affected by using FM/CW but a linear skew to the range walk is enhanced.

Take Equation 3.11 and assume only one target. The equation will take the form of

$$m_{rc}(\tau) = Ae^{\omega_o\tau + \dot{\omega}\tau t - \frac{\dot{\omega}\tau^2}{2}}. \quad (3.71)$$

It is known that  $\tau$  is quadratic in time and is related to projected slant range by

$$\tau = \frac{2R_{ps}}{c}, \quad (3.72)$$

and using the approximation for range from Equation 3.53,

$$\tau \approx \frac{2}{c}\left(R + \frac{(v\bar{t})^2}{2R}\right). \quad (3.73)$$

Note that the distinction between time  $t$  in 3.71 and time  $\bar{t}$  in 3.73. Time  $t$  represents the time index into the chirp of the radar signal and resets to zero at the beginning of every chirp. Time  $\bar{t}$ , also known as "slow time", is the time index as the platform

approaches and passes the target and has the bounds of  $-T_{az}/2$  to  $T_{az}/2$ . They are related by

$$\bar{t} = nT + t, \quad (3.74)$$

where  $T$  is the chirp period and  $n$  is the index of the number of chirps.  $n$  is bounded by  $-n_o$  and  $n_o$ , where

$$n_o = \frac{T_{az}}{2T}, \quad (3.75)$$

$$= \frac{\theta_a R}{2vT}. \quad (3.76)$$

$n$  is an integer, so  $n_o$  may be rounded to the nearest whole number.  $2n_o$  also tells how many azimuth samples are taken of a single target at a given range, and this value is used to calculate the azimuth processing gain.

Next, an approximation reduces the order of  $t$  introduced by the  $\bar{t}$  in  $\tau$ . Squared  $\bar{t}$  results in

$$\bar{t}^2 = (nT)^2 + 2nTt + t^2, \quad (3.77)$$

which may be approximated as

$$\bar{t}^2 \approx (nT)^2 + 2nTt. \quad (3.78)$$

The maximum amount of phase error caused by the approximation can be found because  $t$  is bounded by  $T$ . The maximum error in  $\tau$  is bounded, where

$$\epsilon_\tau < \frac{(vT)^2}{Rc}, \quad (3.79)$$

thus bounding the maximum error in the phase to

$$\epsilon_{ph} < \omega_o \epsilon_\tau + \dot{\omega} T \epsilon_\tau - \frac{\dot{\omega} \epsilon_\tau^2}{2}, \quad (3.80)$$

$$< \omega_o \frac{(vT)^2}{Rc} + \dot{\omega} T \frac{(vT)^2}{Rc} - \frac{\dot{\omega} (vT)^4}{2(Rc)^2}. \quad (3.81)$$

The velocity is bounded by a maximum velocity  $v_{max}$  and can be found by solving

for  $v$  in Equation 3.63. The azimuth bandwidth is proportional to the inverse of the period,

$$BW_{az} = \frac{1}{2T}, \quad (3.82)$$

resulting in the expression

$$v_{max} = \frac{\lambda}{4T\theta_a}. \quad (3.83)$$

The maximum velocity is substituted into Equation 3.81 with  $\lambda = c/f_o$ ,

$$\epsilon_{ph} < \frac{\pi c}{8f_o\theta_a^2 R} + \frac{\pi BWc}{8f_o^2\theta_a^2 R} - \frac{\pi BWc^3}{256Tf_o^4\theta_a^4 R}. \quad (3.84)$$

This equation is true for any system in general, and it can be seen that the minimum range of interest needs to be specified to obtain the correct result. The phase error is 0.039 radians at a 10 m range using BY $\mu$ SAR airborne parameters. This error may be reduced by a factor of 8 by using the approximation,

$$\bar{t}^2 \approx (nT)^2 + (2n+1)Tt - \frac{T^2}{8}, \quad (3.85)$$

but for simplicity the approximation in Equation 3.78 is used.

$\tau$  is now approximated as

$$\tau \approx \frac{2R}{c} + \frac{v^2}{RC}((nT)^2 + 2nTt), \quad (3.86)$$

but can be more easily handled with the substitution  $\tau = a + bt$ , where

$$a = \frac{2R}{c} + \frac{(vnT)^2}{Rc} \quad \text{and} \quad (3.87)$$

$$b = \frac{v^2}{Rc}(2nT). \quad (3.88)$$

Equation 3.71 is now expressed as

$$m_{rc}(t) \approx Ae^{i(\omega_o a - \frac{\dot{\omega} a^2}{2} + [\omega_o b + \dot{\omega} a - \dot{\omega} ab]t + [\dot{\omega} b - \frac{\dot{\omega} b^2}{2}]t^2)}. \quad (3.89)$$

A Fourier transform can be used by making another approximation to get an analytic solution. This time the  $t^2$  term is dropped. By using the fact that  $t$  is bounded by  $T$ , it is shown that the phase error introduced by the drop is

$$\epsilon_{ph2} = \dot{\omega}b \left(1 - \frac{b}{2}\right) T^2, \quad (3.90)$$

$$= \dot{\omega} \frac{2v^2 n T^3}{RC} \left(1 - \frac{v^2 n T}{RC}\right), \quad (3.91)$$

$$= \frac{\dot{\omega} v \theta_a T^2}{c} \left(1 - \frac{v \theta_a}{2c}\right), \quad (3.92)$$

$$= \frac{\pi BW}{f_o} \left(1 - \frac{1}{8f_o T}\right). \quad (3.93)$$

Equation 3.92 substitutes  $n_o$  for its maximum value derived in Equation 3.76, and Equation 3.93 substitutes in the maximum velocity and simplifies. The result is general for any system and is based solely on system parameters. A maximum error of 0.065 radians results from the BY $\mu$ SAR parameters.

The final time waveform is solved by dropping the  $t^2$  in Equation 3.89, where

$$m_{rc}(t) \approx A e^{i(\omega_o a - \frac{\dot{\omega} a^2}{2} + [\omega_o b + \dot{\omega} a - \dot{\omega} ab]t)}. \quad (3.94)$$

The signal essentially exists from time  $a$  to  $T$ . Thus the transform becomes

$$M_{rc}(\omega) = \int_a^T m_{rc}(t) e^{-i\omega t} dt, \quad (3.95)$$

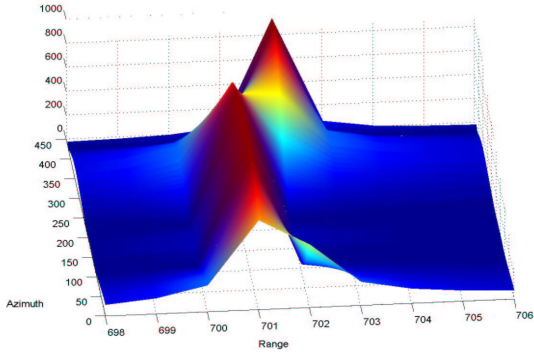
$$= A e^{i(\omega_o a - \frac{\dot{\omega} a^2}{2})} \int_a^T e^{i([\omega_o b + \dot{\omega} a - \dot{\omega} ab]t)} e^{-i\omega t} dt, \quad (3.96)$$

$$= A e^{i(\omega_o a - \frac{\dot{\omega} a^2}{2})} \int_a^T e^{i(\omega_o b + \dot{\omega} a - \dot{\omega} ab - \omega)t} dt, \quad (3.97)$$

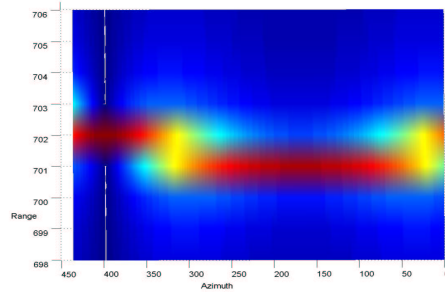
$$M_{rc}(\omega, n) = A e^{i(\omega_o a - \frac{\dot{\omega} a^2}{2} + (\omega_o b + \dot{\omega} a - \dot{\omega} ab - \omega) \frac{T+a}{2})} (T-a) * \text{sinc} \left( (\omega_o b + \dot{\omega} a - \dot{\omega} ab - \omega) \frac{T-a}{2} \right). \quad (3.98)$$

The parameter  $n$  is added to the last equation to indicate the dependence of  $a$  and  $b$  on  $n$ . A two dimensional equation results that represents the response of a single

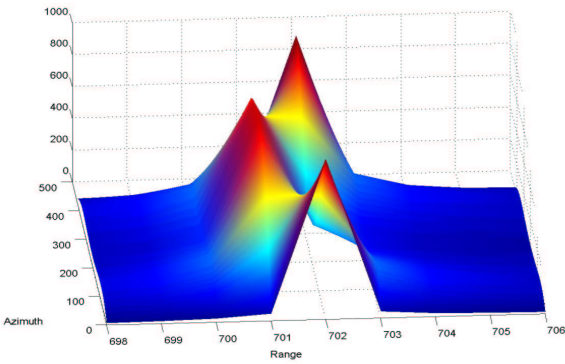
target with  $n$  representing the azimuthal response and  $\omega$  the range response after range compression.



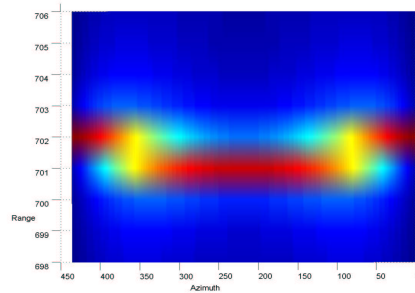
(a) Range Walk Skew at 1ms



(b) Range Walk Skew at 1ms



(c) Range Walk Skew at  $10\mu s$



(d) Range Walk Skew at  $10\mu s$

Figure 3.11: Simulation results showing the difference in range walk skew between a 1ms and a  $10\mu s$  chirp period. Plots a and b are the same data rotated to illustrate the shift, as are c and d for  $10\mu s$ .

Both simulated and analytic plots of range compression show a linear skew to the typical range walk. Figure 3.11 shows plots of the simulated response at a range of 150m. Plots (a) and (b) have a period of 1  $ms$  and plots (c) and (d) have a 10

$\mu s$  period. The term  $\omega_o b(T + a)/2$  in the exponent of Equation 3.98 is found to be the contributor to this effect. The shift in frequency is found by substituting in the  $a$  and  $b$  variables,

$$\omega_{lrw} = \frac{2\omega_o v^2 n T (T + \frac{2R}{c} + \frac{(vnT)^2}{Rc})}{2Rc}. \quad (3.99)$$

A dominantly linear range walk term in frequency becomes apparent because  $n$  is linear.

A single target fixed in range has all constants with the exception of  $n$  which ranges from  $-n_o$  to  $n_o$ . Substituting  $2n_o$  in place of  $n$  sets the maximum bound for the amount of frequency shift expected from  $-T_{az}$  to  $T_{az}$ ,

$$\omega_{shift} = \frac{\omega_o v \theta_a (T + \frac{2R}{c} + \frac{(vnT)^2}{Rc})}{c}. \quad (3.100)$$

The result is dependent on range, and this is true for only FM/CW SAR systems. The response for a pulsed FM SAR is

$$\omega_{shift} = \frac{\omega_o v \theta_a T}{c}. \quad (3.101)$$

The period  $T$  determines that amount of skew in the range walk, and for pulsed systems  $T$  is so small that the effect is negligible. For FM/CW systems this must be considered as well as the range dependence, and appropriate algorithms may be used to compensate for the skew.

The phase integrity of a FM/CW SAR is the main question that this thesis is to address. The first two terms  $\omega_o a - \frac{\dot{\omega} a^2}{2}$  dominate the phase response in Equation 3.98 and determine the phase of the signal for every value of  $n$ . Substituting back in the variable  $a$  results in

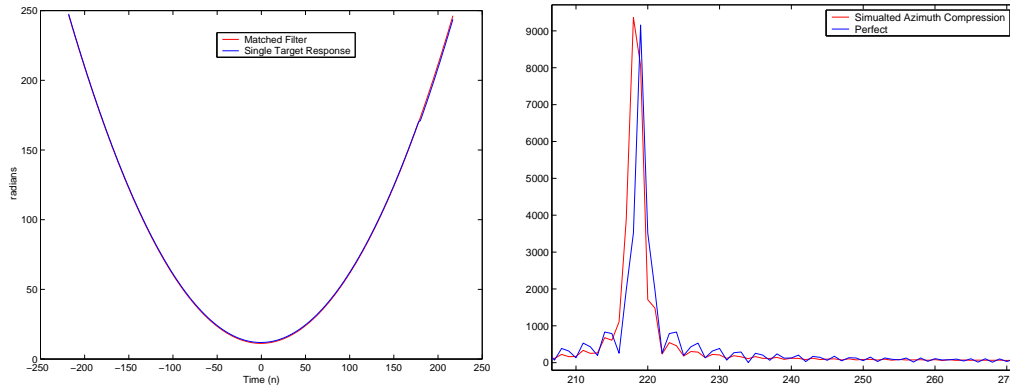
$$\phi_{dop} = \frac{2\omega_o R}{c} + \frac{\omega_o v^2 n^2 T^2}{Rc} + \frac{2\dot{\omega} R^2}{c^2} + \frac{2\dot{\omega} v^2 n^2 T^2}{c^2} + \frac{\dot{\omega} v^4 n^4 T^4}{2c^2 R^4}. \quad (3.102)$$

The only variable with time is  $n$  so any term that does not have dependence on  $n$  may be dropped. Two  $n^2$  terms are left and a  $n^4$  term. Next the maximum amount

of phase change introduced by the  $n^4$  term is calculated. Substituting  $2n_o$  for  $n$  forces an upper bound on the phase change,

$$\Delta\Phi_{n^4} = \frac{\dot{\omega}\theta_a^4 R^2}{2c^2}. \quad (3.103)$$

It is 0.00185 radians for the BY $\mu$ SAR airborne parameters, so the removal of the term is justified. The  $n^2$  term is exactly what is expected because  $n$  increases linearly, thus  $n^2$  is quadratic. The simulated results show this to be true as shown in Figure 3.12 (a). Plot (b) shows the FM/CW signal has good azimuth compression.



(a) Uncompressed Phase Response

(b) Azimuth Compression

Figure 3.12: Azimuth Compression of simulated phase for a target 150m in range. The chirp period is 1 ms.

### 3.6 FM/CW Limitations and Optimization

The limits of FM/CW SAR systems that are presented here are based on the previous analysis. A guide is given on how to choose and optimize the system parameters for the best performance.

Three key limitations on the chirp period are found when implementing FM/CW based SAR. First the range is limited by the degree to which the range resolution is able to degrade. From Equation 3.48 it is seen that the range resolution is degraded by the  $T-2R_s/c$  term located in the sinc function. If the term drops to  $T/2$  then the resolution doubles, and if to  $T/4$  it quadruples and so on. Equation 3.5 may be modified to account for this effect by letting

$$\Delta R_{s,mod} = \frac{c}{2BW} \left( \frac{cT}{cT - 2R_s} \right). \quad (3.104)$$

Second, platform velocity limits the chirp period. The maximum velocity is related to the period by Equation 3.83 for a system where  $PRF_{min} = 1/T$ , and it is seen that the relationship is inversely proportional. Knowing the type of platform to be used, realistic speeds for imaging may be calculated and used to determine an upper bound of the period. The  $PRF_{min}$  and  $1/T$  may be equal depending on the type of modulation being used. In general,  $PRF_{min}$  must be less than or equal to  $1/T$  in order to ensure that proper azimuth sampling is occurring. This puts an upper limit on the range of  $T$ . The  $PRF_{min}$  is related to the velocity by Equation 3.64 and so it is seen that there are fundamental relationships between the PRF,  $v$  and  $T$ . Therefore FM/CW based SAR is best suited for shorter ranged remote sensing of approximately a 10 km maximum range. The platform is also velocity limited and would not be appropriate in high speed aircraft.

Finally, the period is limited by the amount of range walk skew that is permissible. No attempt is made to perform any range walk compensation which is generally used in high performance systems. These algorithms can be modified to encompass the linear skew.

It has been shown that FM/CW has a number of benefits that are maximized when the period is maximized. Long pulse periods are achievable because the transmit and receive signals are required to simultaneously exist. High SNR and low transmit power are a result of the long pulse period. A low baseband frequency, simpler electronics, feed-through rejection, and less digital processing power are results of



directly mixing the transmit and receive signals to dechirp or compress the receive signal.

A guideline for maximizing the period of a FM/CW SAR system is outlined below:

1. Choose a frequency for the desired electromagnetic interaction with the scene and within licensing limitations.
2. Set the bandwidth to achieve the desired range resolution allowing for any increase due to large periods. This may also be limited by licensing limitations.
3. Determine the desired azimuth resolution and set the antenna azimuthal beamwidth according to Equation 3.66.
4. Determine the maximum and minimum ranges of interest.
5. Determine the maximum velocity that the platform will achieve during imaging. This sets the minimum PRF.
6. Determine the chirp type whether sawtooth or triangular. Also determine whether both the up and down chirps or only one will be used. Note that all previous derivations assumed a sawtooth type chirp with a 100% duty cycle.
7. Maximize T and ensure that the following satisfy the desired performance criterion:

$$\text{Range walk} \Rightarrow \omega_{shift} = \omega_o v \theta_a (T + \frac{2R}{c} + \frac{(vnT)^2}{Rc}) / c$$

$$\text{Phase error} \Rightarrow \Delta\Phi_{n^4} = \frac{\dot{\omega}\theta_a^4 R^2}{2c^2}$$

$$PRF_{min} < 1/T$$

Make sure the approximations in Equations 3.84 and 3.93 are within the specified tolerance.

## Chapter 4

### BY $\mu$ SAR System Design

A prototype system is required to verify that FM/CW can be used to generate quality SAR images. This chapter defines the specifications for an airborne and track system, and builds a design around them. The first section gives a system block diagram and a list of modules that make up the complete SAR. The next two sections divide these modules into two groups, transmitter and receiver. The whole assembly of the system is reviewed, and then the system's SNR is calculated based on the radar equation and noise analysis.

#### 4.1 BY $\mu$ SAR Specifications

Airborne and track specifications are listed in this section with attention paid to slant range calculations and the dependence of range resolution on the elevation of the platform. The system block diagram is given followed by a list identifying each module and its interconnects.

##### 4.1.1 Airborne System Specifications

This SAR system is designed so that it can be used in the same aircraft as YINSAR. The same geometrical parameters and velocity for the aircraft are also used. The geometry, as illustrated in Figure 4.1, helps define the maximum and minimum slant range from a chosen elevation and swath width. The aircraft flies at an elevation between 300m and 600m. The look angles are  $\phi_1 = 45^\circ$  and  $\phi_2 = 65^\circ$ .  $R_{min} = 300m$ ,  $R_{max} = 600m$ ,  $R_{s,min} = 424m$ , and  $R_{s,max} = 671m$  for the 300m

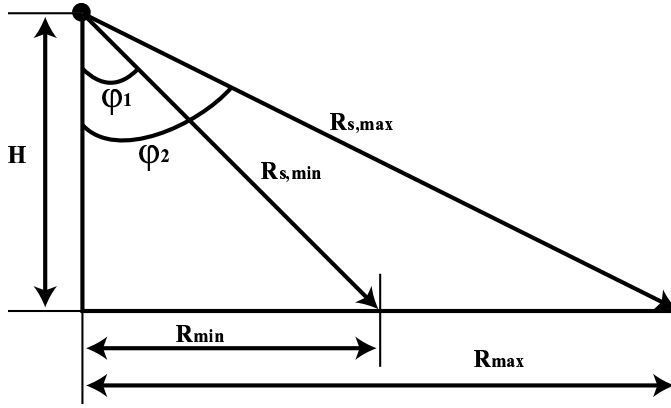


Figure 4.1: Maximum and minimum ranges help to determine the dynamic range and SNR required for the radar.

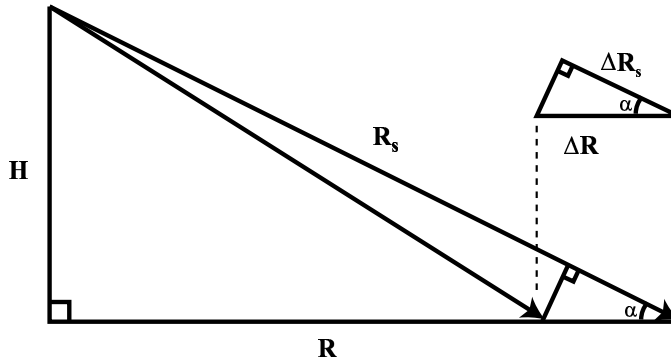


Figure 4.2: Range resolution is related to slant range resolution, range, and elevation.

elevation, and at a 600m elevation  $R_{min} = 600m$ ,  $R_{max} = 1,200m$ ,  $R_{s,min} = 849m$ , and  $R_{s,max} = 1,342m$ .

Range resolution is also a function of elevation and can be approximated by knowing the slant range resolution. Consider the relationship between the two triangles in Figure 4.2.

It is seen that

$$\tan \alpha = \frac{H}{R} \quad (4.1)$$

Table 4.1: BY $\mu$ SAR Airborne Parameters

Symbol	Description	Value
$f_o$	Initial Frequency	9.8 GHz
$\lambda$	Wavelength	3.03 cm
$BW$	Chirp Bandwidth	200 MHz
$T$	Chirp Period	1ms
$T \cdot BW$	Time Bandwidth Product	10,000
$Samp_{A/D}$	A/D Sample Rate	2 MHz
$PRF_{min}$	Minimum Pulse Repetition Frequency (PRF)	700 Hz
$d$	Real Aperture Length	0.223 m
$\Delta R_s$	Slant Range Resolution	.75 m
$\Delta a$	Theoretical Azimuth Resolution	0.10 m
$v$	Velocity	60 m/s
$H$	Nominal Radar Platform Elevation	300 $\rightarrow$ 600 m
$L_{TL}$	Transmission Line Loss	2 dB
$P_t$	Transmit Power	0 dBm
$\theta_a$	Azimuth 3dB Beam-width	10 $^\circ$
$\theta_r$	Range 3dB Beam-width	45 $^\circ$
$G_t$	Transmit Antenna Gain	17 dB
$G_r$	Receive Antenna Gain	17 dB
$\sigma^\circ$	Surface Scattering Coefficient	-25 $\rightarrow$ 20 dB
$F_{RF}$	RF Amplifier Noise Figure	4 dB
$G_{RF}$	RF Amplifier Gain	50 dB
$F_M$	Mixer Noise Figure	10 dB
$G_M$	Mixer Gain	-10 dB
$F_{IF}$	IF Noise Figure	10 dB
$G_{IF}$	Gain	-2 $\rightarrow$ 50 dB
$BW_{IF}$	IF Bandwidth	2MHz

and

$$\sec \alpha = \frac{\Delta R_s}{\Delta R} \quad (4.2)$$

yields

$$\Delta R = \Delta R_s \sec \left( \tan^{-1} \left( \frac{H}{R} \right) \right), \quad (4.3)$$

$$= \Delta R_s \sqrt{1 + \frac{H^2}{R^2}}, \quad (4.4)$$

where the last step makes use of the identity  $\sec(\tan^{-1}(x)) = \sqrt{1 + x^2}$ . Equation 4.4 shows that the best range resolution is  $\Delta R_s$  for  $R \gg H$  and becomes very large for  $H \gg R$ .

The parameters shown in Table 4.1 are based on the previous derivations and system parameters defined for YINSAR in Table 2.1. The surface scatter coefficient ranges from -25 to 20 dB covering industrial to desert terrain classes over a 45° to 65° incidence angle [28].

#### 4.1.2 Track System Specifications

The SAR parameters shown in Table 4.2 represent the systems configuration when it is tested on the track to verify the radar's data quality.

#### 4.1.3 Block Diagram

Figure 4.3 shows the system's general block diagram for a dual channel SAR capable of doing interferometry. A PC using the RS232 protocol manages the FM/CW source in generating the frequency chirp. The chirp signal is divided by a power splitter feeding the LO port of each RF mixer and a transmit antenna. The return signal from the scene is received through an antenna and amplified by a low noise amplifier. The signal then passes into the RF mixer where it is mixed with the local oscillator, compressing the scene data into the baseband signal. The baseband signal comes out of the IF port of the mixer and is amplified by a PC controlled variable gain amplifier and then lowpass filter. The signal is then digitized using an analog-to-digital converter that is synchronized with the transmitter by a sampling trigger. The data is then processed to generate a fully compressed SAR image.

Table 4.2: BY $\mu$ SAR Track Parameters

Symbol	Description	Value
$f_o$	Initial Frequency	9.8 GHz
$\lambda$	Wavelength	3.03 cm
$BW$	Chirp Bandwidth	200 MHz
$T$	Chirp Period	500 $\mu s$
$T \cdot BW$	Time Bandwidth Product	1000
$Samp_{A/D}$	A/D Sample Rate	100 kHz
$PRF_{min}$	Minimum Pulse Repetition Frequency (PRF)	2.93 Hz
$\theta_a$	Azimuth 3dB Beam-width	10 $^\circ$
$\theta_r$	Range 3dB Beam-width	45 $^\circ$
$d$	Real Aperture Length	0.223 m
$\Delta R_s$	Slant Range Resolution	0.75 m
$\Delta a$	Theoretical Azimuth Resolution	0.10 m
$V$	Velocity	0.327 m/s
$H$	Nominal Radar Platform Elevation	0 m

The system design is divided into modules by functionality. Each module is designed for a general interface such that blocks may be changed to accommodate changes in system requirements.

1. RF Transmitter - contains only the high frequency components of the FM/CW source and is encased in a machined aluminum case. The module connects to the driver plane by a series of feed-troughs and a MCX RF connector. It connects to the transmit antenna and RF mixers through SMA semirigid coax cables.
2. Driver/Power Plane - this module contains the digital logic for the FM/CW source which includes a PECL frequency counter and a CMOS waveform generator. A RS232 connection allows a PC to communicate with the waveform generator. The plane routes signals between the other modules and distributes power to them. Voltage regulation for each LNA block is also provided on the plane.

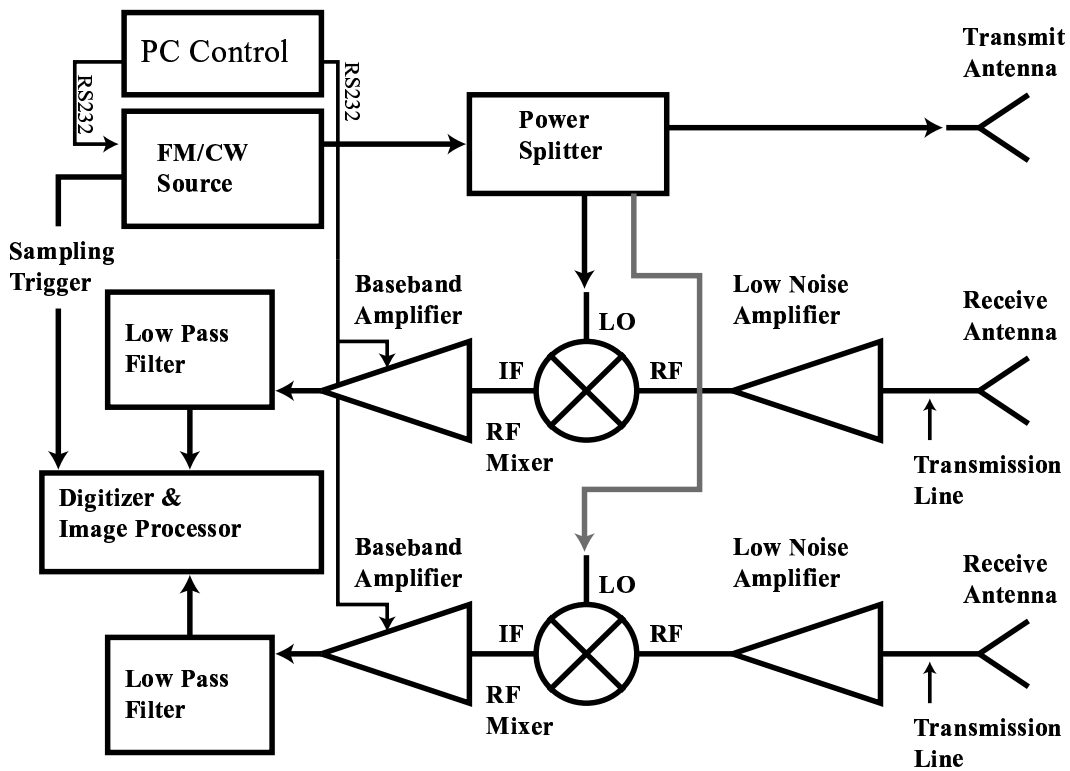


Figure 4.3: Simplified Block Diagram of SAR System.

3. LNA - two 50 dB low noise amplifiers with a 4 dB noise figure. Each LNA is encased in a machined aluminum case with SMA connectors to interface with the antennas and RF mixers.
4. RF Mixer - the mixer is encased in a machined aluminum case with SMA connectors to interface with the LNA, RF transmitter, and baseband module.
5. Baseband Module- this module includes a variable gain amplifier with filtering for baseband processing. It receives signals from the RF mixers via the SMA semirigid coaxial cables. The gain is controlled by a PC that communicates

via a RS232 protocol. It sends the amplified signal to the digitizer through a BNC connector and connects to the driver/power plane through a card edge connector.

6. Power Module - Input power is  $\pm 12$  Volts, which is divided into a variety of voltages and power planes. The module plugs into a card edge connector in the driver/power plane where the power is distributed to components and other modules.
7. Digitizer and Image Processor - the digitizer is an oscilloscope with deep memory acquisition. The image processing is accomplished using Matlab.

## 4.2 Transmitter

A unique way to linearize the chirp from a VCO is shown where a microcontroller sets the VCO's tuning voltage and then measures its response. The transmitter is discussed in two parts, the RF module and the driver. The RF module contains parts that radiate high frequency emissions and should be isolated from noise sources. The driver is separated into two sections based on functionality, which are the waveform generator and phase counter circuit. The waveform circuit takes the digital values calculated from the microcontroller and turns them into a clean analog signal, where the phase counter measures the frequency output of the VCO. The algorithms that control these operations are explained in the algorithms section.

### 4.2.1 LFM Generation

Frequency sweep nonlinearity is considered a limiting factor in FM/CW range resolution and a contributor to spectral clutter in the range compressed signal [29, 30]. Many different methods have been used to achieve high linearity in the FM signal with varying degrees of success [31, 32, 33]. A unique and successful method to linearize the output of a VCO is introduced.

The difficulty in producing a linear chirp comes from the fact that VCOs do not exhibit a linear tuning voltage as exaggerated in Figure 4.4 (a). The tuning voltage



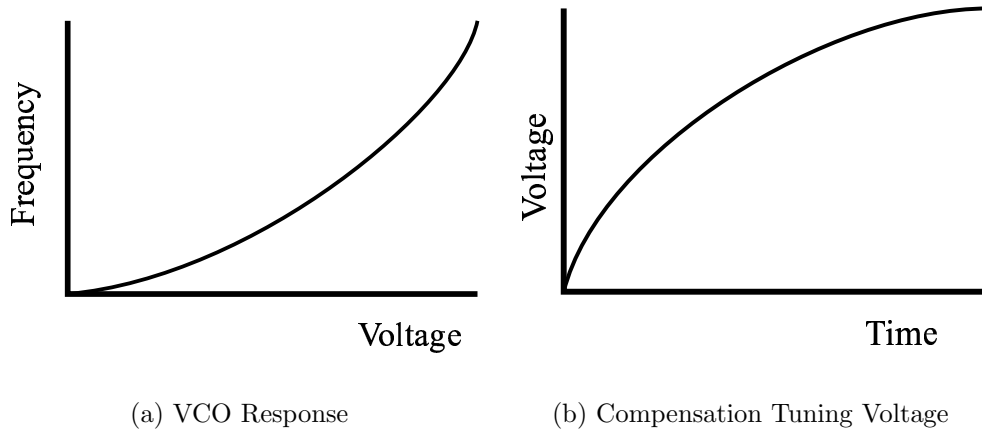


Figure 4.4: Figure (a) shows the nonlinear frequency response of a VCO due to a linear tuning voltage. The tuning voltage must compensate for nonlinearities in order to get a linear frequency response as illustrated in figure (b).

must take on a nonlinear form as illustrated in Figure 4.4 (b) in order to get a LFM waveform. A digital voltage mapping can be determined by measuring the frequency response of a given VCO by using a system like the one shown in Figure 4.5. This is done by setting the DAC to a known voltage and then measuring the frequency output of the VCO. The voltage is changed and the process repeated until the VCO is characterized over the bandwidth of interest. This design is used in a stationary interferometric radar system that detects track hazards on railways [34, 35, 36]. Phase errors are introduced in this system due to large drifts in the center frequency of the chirp on the order of MHz.

The railway system used a static calibration where it maps out the voltages once and then generates a waveform continuously based on that one mapping. A VCO's frequency-to-voltage relationship is dependent on its bias voltage (frequency pushing), load (frequency pulling), and temperature [37]. The dynamic calibration scheme used in this transmitter measures the initial frequency-to-voltage relationship and modifies the digital maps offset accordingly. This scheme assumes that the waveform shape does not change over time, thus allowing the frequency to be controlled

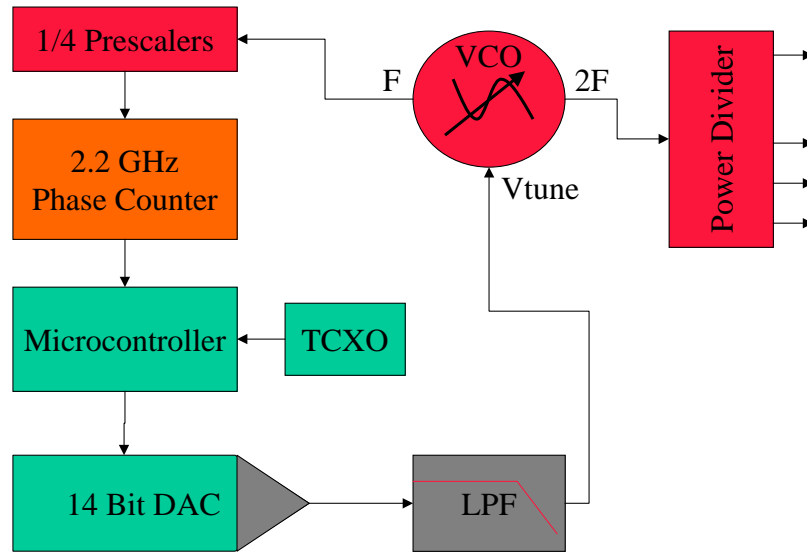


Figure 4.5: Block Diagram of Transmitter Architecture.

by simply changing the initial frequency. This assumption is valid for narrow banded chirping as used in this transmitter. The generator is simple in design and can be made using high volume production available integrated circuits.

#### 4.2.2 RF Module

The RF module is comprised of all the microwave components associated with the transmitter. This includes a VCO, 5GHz divide by 2 prescaler, 2.5GHz divide by 2 prescaler, and a ring coupler. These pieces are designed together on one piece of RF substrate where matching can be closely controlled.

The VCO is made by Spinnaker Microwave with a fundamental oscillator at 2.5 GHz which is doubled twice. Ports are supplied for the 5GHz and 10GHz signals. On the 10GHz chain an additional amplifier is integrated into the circuit to have an output of 14 dBm. The tuning voltage range is 0-10 volts and has a bias voltage of 10

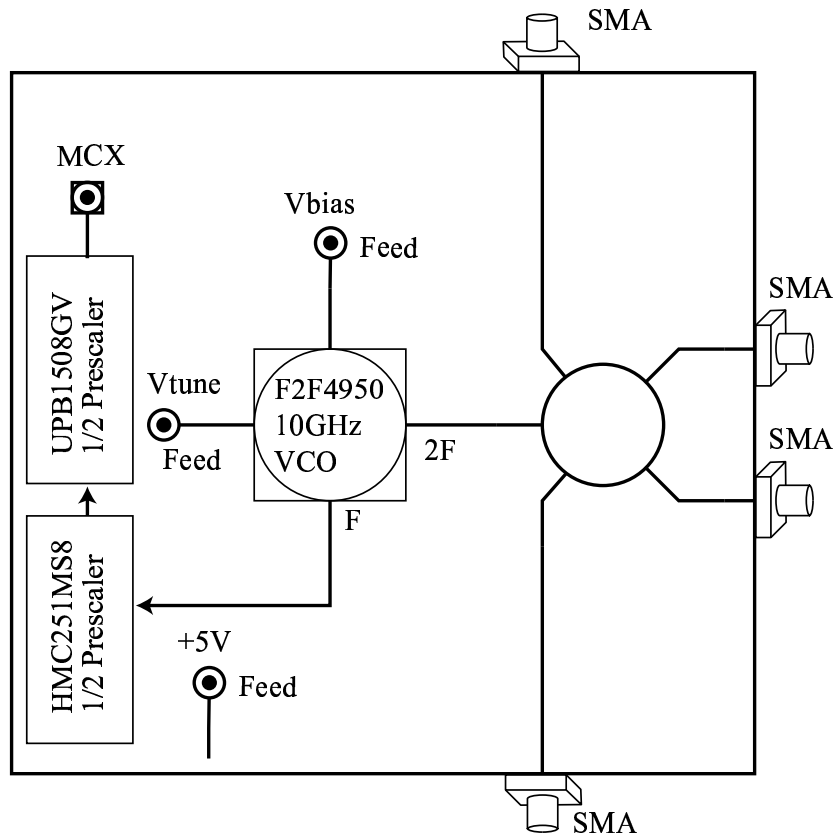


Figure 4.6: Transmitter Module Schematic.

volts. The high power is desired to eliminate the need for additional amplifier stages while allowing each mixer LO drive level to be approximately 10 dBm.

The 5GHz signal needs to be divided below the 1.3 GHz maximum input to frequency counter so two divide by 2 prescalers are used. The first prescaler is the Hittite HMC251MS8 that is biased by a single 5 volts supply. Its performance ranges from 3.0-6.5 GHz and allows a wide range of input power while maintaining a level output power of -7 dBm. The second prescaler is the NEC UPB1508GV and it is also biased at 5 volts and receives a 0.5-3.0 GHz input. This part has a broad input power sensitivity and an output power of -7 dBm. The signal is then routed to the driver board via a MCX connector which protrudes through a hole machined in the bottom of the RF modules case and the MCX connector series is rated up to 6 GHz.

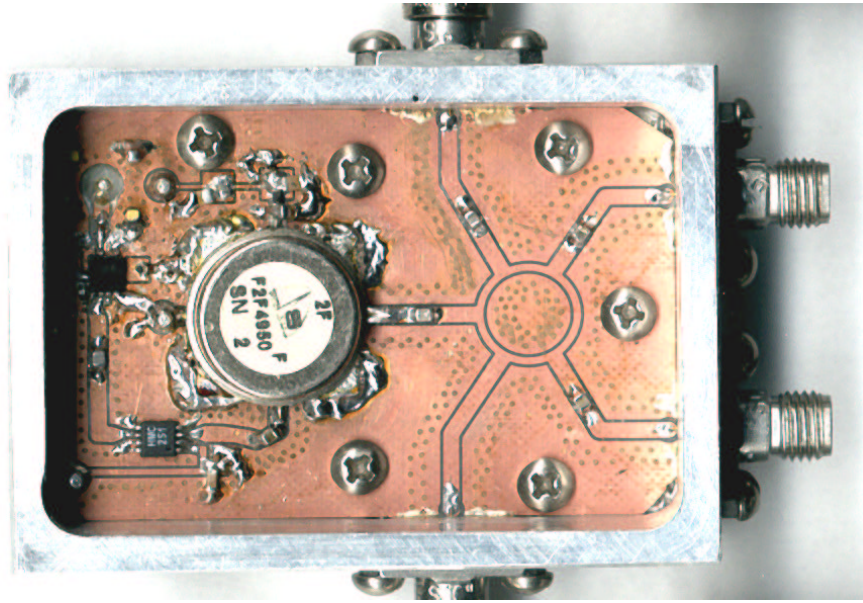


Figure 4.7: Transmitter Module. The large can in the center of the figure is the VCO, and the two other chips are the divide by two prescalars. The two side ports deliver 10 dBm of power while the end ports each provide 0 dBm of power.

The 10 GHz signal from the VCO is AC coupled into a ring coupler. This coupler is designed to have two LO ports at -4 dB and two at -14 dB. One -14 dB is used for the transmit signal and the other can be terminated or used for test purposes. The ring design and test are cover in Appendix A. Each of the ports are brought through the case using a Southwest Microwave SMA connector. The VCO's control voltage and power distribution are routed into the module using pi network filtered feed-throughs made by Tusonix. The filters have a 60 dB insertion loss at 10 GHz and 20 dB at 10 MHz . A parallel combination of capacitors 1 pF, 100 pF, and 100 nF are used to filter the power at the bias pins of all the active parts. A general schematic is shown in Figure 4.6 and the actual module is shown in Figure 4.7.

### 4.2.3 RF Driver Module

The driver module comprises the PECL phase counter, microcontoller, DAC, interpolation filter, and other support chips. The module is divided into two sections,

the phase counter circuit and waveform generator. The schematic shows additional parts that route the power and signals between modules.

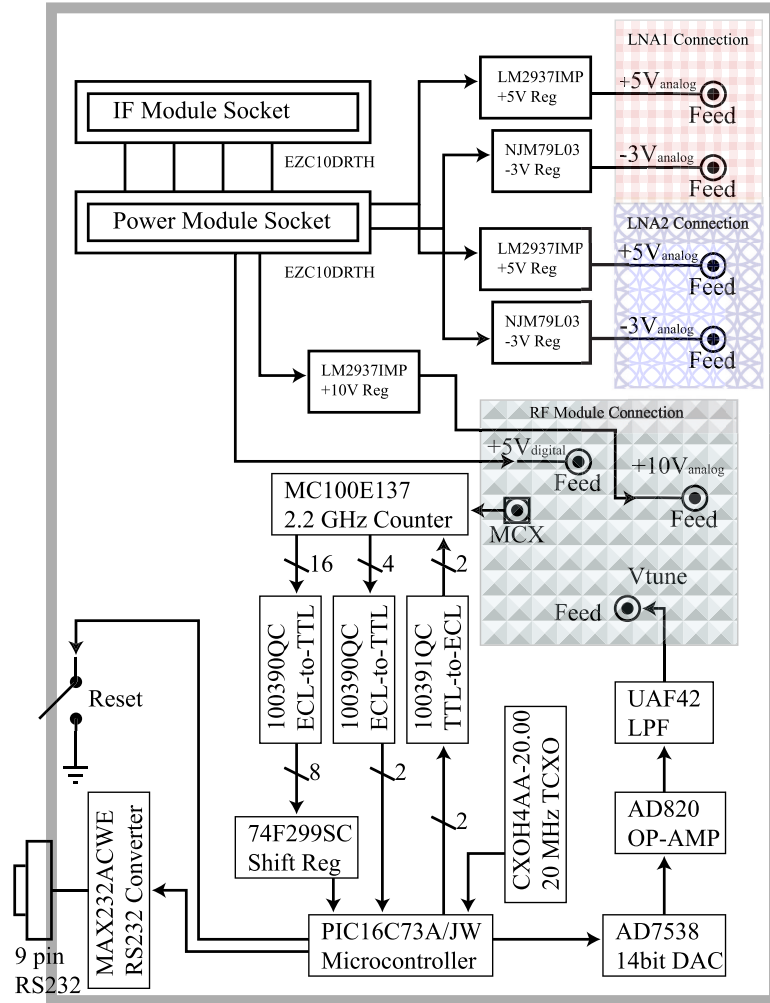


Figure 4.8: Main board Schematic Including Transmitter Driver.

Figure 4.8 shows the schematic for the main board. The driver board also routes power from the power module to all the other modules and provides regulation to LNA modules. Card edge connectors are used to interface to the power module and IF gain module. Maximum's MAX232ACWE converter is used to link a PC host to the PIC microcontroller, and a BNC trigger output is supplied to synchronize the

data acquisition. Figure 4.9 shows the driver board without the modules. The PIC can be reset using a momentary switch. An additional 28 pin dip socket is seen that is intended to hold another PIC that is to control the IF gain module, but development went faster when a PIC and its own RS232 converter was put on the IF gain module. Jumper wires in the socket connect the communication lines from the RS232 converter to the PIC that controls the DAC. The empty header with parallel traces from the empty PIC socket are for a LCD interface.

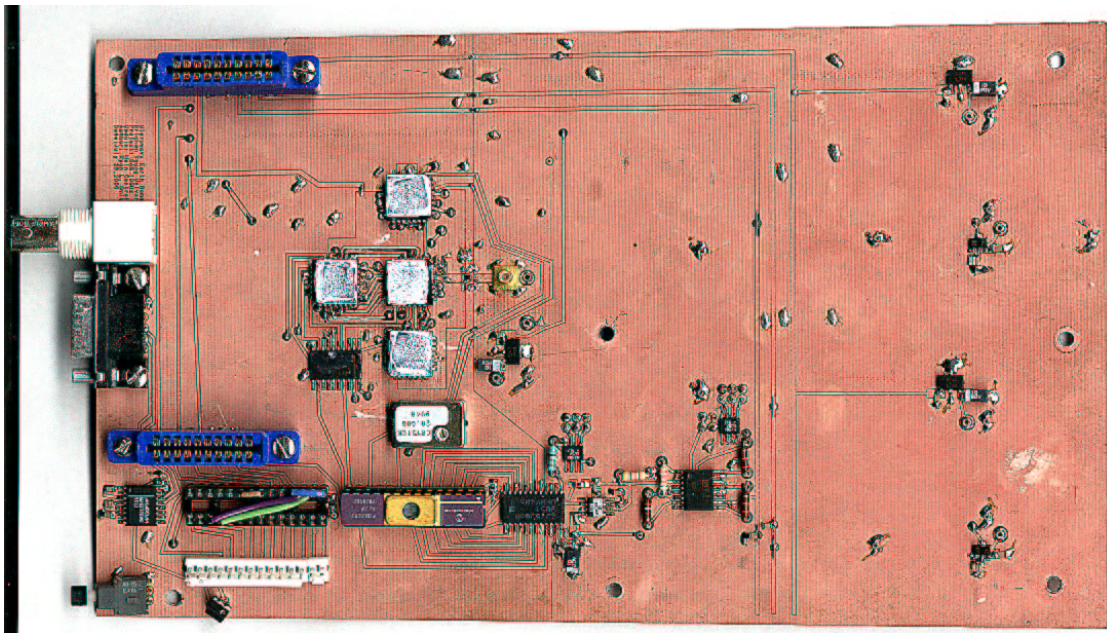


Figure 4.9: Driver Board without Modules.

## Waveform Generator

The waveform generator is designed to convert a digital waveform into a smooth, undistorted analog waveform. The generator is made up of a DAC followed by a current to voltage amplifier stage, lowpass filter, and a voltage offset amplifier. The tradeoff in the filter design is made between suppressing the DAC update rate

and allowing a quick recovery when the chirp changes directions. The design uses sockets and adjustable references to aid in the optimization process.

Analog Devices AD7538 14 bit, parallel load DAC is used to make the VCO frequency resolution high. The DAC's current output is converted to voltage using Analog Devices AD820 op-amp and interpolated through Burr Brown's UAF42 universal active filter. The filter is set in the lowpass configuration with resistors being adjusted to maximize performance in filtering out the undesired DAC update rate while maintaining the linearity of frequency ramp. The auxiliary op-amp in the UAF42 is used for a voltage level shift and gain stage following the filter to allow the drive voltage to be specifically tuned to the VCO tuning voltage range.

Sockets are used to allow easy insertion of leaded resistors to set the corner of the filter and adjust the voltage shift and gain of the offset amplifier. Voltage references are used in conjunction with regulators to stabilize the bias and reference voltages. The tuning voltage of the VCO is 5.6 to 8.1 volts for the 9.8 to 10 GHz frequency range. The resolution of the DAC corresponded to 14.84 counts or 618 kHz. The shape of the chirp is shown in Figure 4.10.

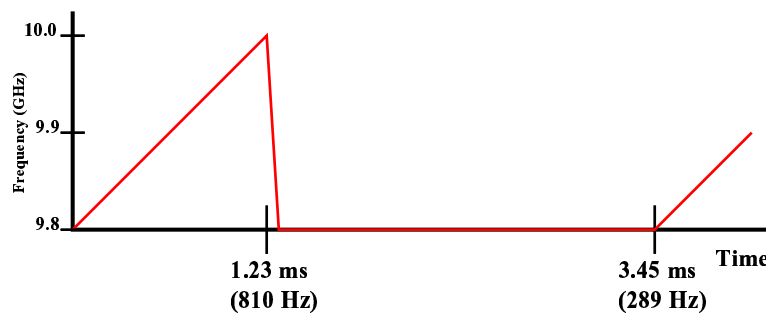


Figure 4.10: Frequency profile of transmit signal. The long flat spot is designed so that the phase counter can make an accurate measurement of the frequency at the beginning of every chirp.

## Phase Counter Circuit

The phase counter accurately measures the output of the VCO by the use of high speed logic and a counter in the PIC microcontroller. This measurement is used to determine an array of digital values, that when sent to the DAC create a linear frequency output from the VCO.

The phase counter circuit consists of a PECL counter, PECL-TTL translation chips, a shift register and a PIC microcontroller. A short overview of Emitter Coupled Logic (ECL) is included in Appendix F to aid understanding in the workings of the PECL parts. The MC100E137 is a high speed, 8-bit ripple counter that can handle clock speeds up to 2.2 GHz. The counter is able to count a 1.25 GHz signal at a power level of -10 dBm by using the AC coupling scheme as shown in Appendix F. CMOS or TTL level translation devices are necessary to interface with the chip. The two different Fairchild devices used are the 100390 ECL to TTL translator and the 100391 TTL to ECL translator. Power supply conversions, shown in the Appendix, are required to operate the devices as PECL devices where they run on a positive 5 volt supply.

A carefully designed 5 volt and 3 volt power plane ensures successful operation of PECL devices that tend to draw a lot of current and are sensitive to noise. The chips are placed close together to minimize transmission line effects at high speeds. The 3 volt supply is used to terminate the transmission lines so the amount of the energy consumed by the circuit is reduced. The PIC16C173A microcontroller is clocked at 20 MHz with a TCXO. A shift register is used to load the bits from the phase counter into the PIC to reduce the I/O support. The most significant bit from the MC100E137 is routed into a 16 bit counter in the PIC.

### 4.2.4 Algorithms and Control Code

The hardware has been described that generates the LFM signal and now the digital waveform generation in code is explained. Some processing for the calibration routine is carried out on the PC because the PIC is an 8 bit processor with limited



resources. Here the calibration algorithm is shown in detail, and the rest of the code is left to be examined as it is in the Appendix.

Figure 4.11 shows the flow diagram for the algorithm used to calibrate the transmitter. A static calibration loop in the microcontroller sets the DAC to a predetermined voltage and then measures the response of the VCO. The value from the PIC and PECL counters are sent to the PC where it compares the measured frequency to a desired frequency, and then adjusts the voltage accordingly. The adjusted voltage is sent back to the PIC where it loads the DAC, and again measures the frequency. It will repeat the process until the measured and desired frequencies match. This process is repeated for a linear array of desired frequencies.

The run mode follows a similar pattern by stepping through the array and loading the DAC in a timed sequence. A trigger pulse is generated to synchronize the transmitter with the digitizer. When the end of the array is reached, the PIC loads the start value for the chirp and then measures the output frequency. The array offset is adjusted if the measured initial frequency is out of range. The relative array is then run through once again. The ability to measure the initial frequency on each pass during transmission and correct for any error, makes the transmitter calibration quasi dynamic.

Because of the limited resources of the PIC, the Visual Basic Executable converts constants such as bandwidth, initial frequency, and channel gain into parameters used by the PIC. The Visual Basic user interface is shown in Figure 4.12. The radar's transmit frequency is strongly dependent on temperature and requires a warm up period. The strip chart shown at the bottom of the screen shot plots the frequency as a function of time. When the frequency stabilizes, the transmitter is ready for calibration. Debug functions include frequency counting, selectable voltage output, communication test, and calibration feedback. The code for both the PIC and the executable are included in the Appendix.

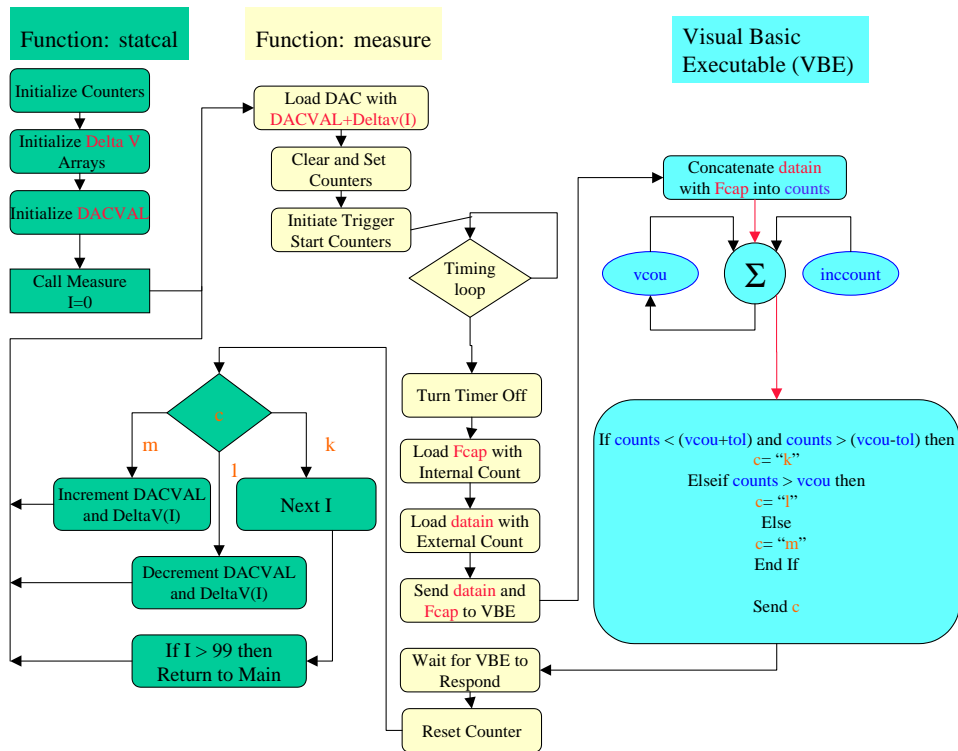


Figure 4.11: The transmitter calibration algorithm passes parameters back to the VBE to perform higher order arithmetic. The actual program uses two arrays due to the limitation of the microcontroller’s memory structure.

### 4.3 Low Noise Receiver

The design and development of a low noise receiver system for radar is now described. It begins with the design of a 50 dB LNA that has a noise figure of 4 dB. The RF mixer is discussed followed by the design of the IF gain module. The IF gain module is replaced by an instrument amplifier and filter during tests because of a design flaw in the IF baseband amplifier stage.

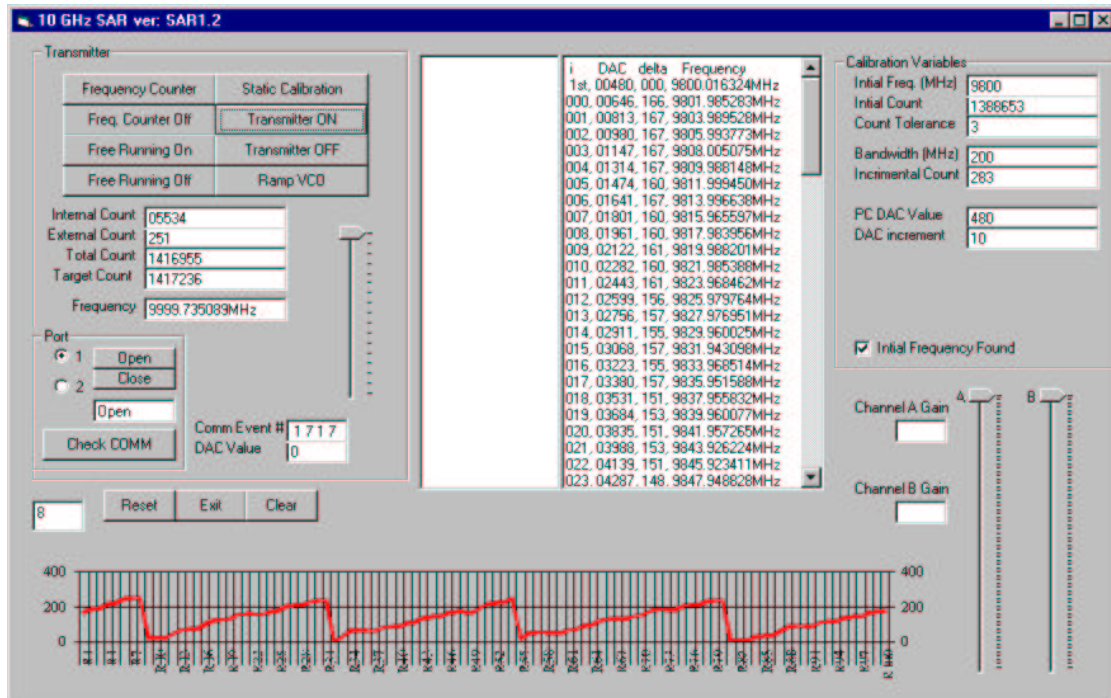


Figure 4.12: Visual Basic Graphical User Interface

### 4.3.1 Low Noise Amplifier

The design and development of a high gain LNA is outlined by covering the techniques used in biasing and matching. Simulated and measured results agree on gain, but the noise figure is different from what is expected. The board is designed on RF substrate using coplanar technology.

Section A.3 in Appendix A shows that high isolation can be achieved using coplanar technology. Figure 4.13 shows the combination of hand coiled inductors and capacitors used to achieve approximately 50 dB of isolation between the transmission line and biasing resistors. The gates are each biased using a  $10k\Omega$  trim pot and the drains use a single resistor connected to a 5 volt power supply that delivers the appropriate amount of current to set the S parameters of the FET.

CELs NE329S01 transistor is selected for its excellent gain and low noise at 10 GHz. A design program is used to calculate the reflection coefficients for the source and load of the amplifier. This program uses the unilateral match and the assumption that the load will be conjugate matched. Noise parameters and S parameters

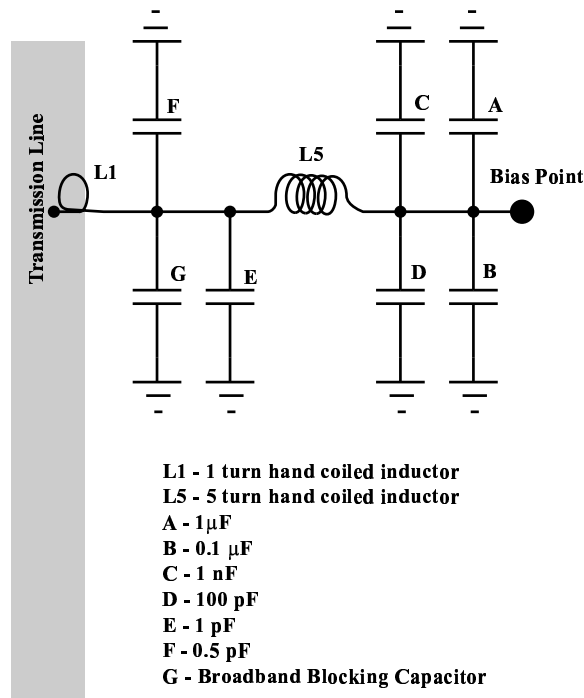


Figure 4.13: Biasing Network for Gate and Drain.

for a specific frequency, voltage, and current are loaded, and a Smith chart on the source reflection plane  $\Gamma_S$  is generated, showing the constant gain and noise circles. Reflection points are selected and the corresponding coefficients are tabulated and displayed as shown in Figures 4.14 and 4.15.

Four gain stages are required in order to achieve 50 dB of gain. The first is designed for low noise, followed by two for maximum gain and the last for maximum gain and output power. The first three operate at the same bias voltage and current on the drain, where the last stage has increased current and voltage. Two plots are required where the S parameters are different. The first three FETs are represented in Figure 4.14 while the last one is represent in Figure 4.15.

Figure 4.16 shows the general schematic for the LNA with matching networks 2 and 3 being the same. Staggered interdigital capacitors are used to set up the matching networks. These capacitors not only provide a match but also A/C couple the devices so that the bias points on the gate and drain of each transistor may be

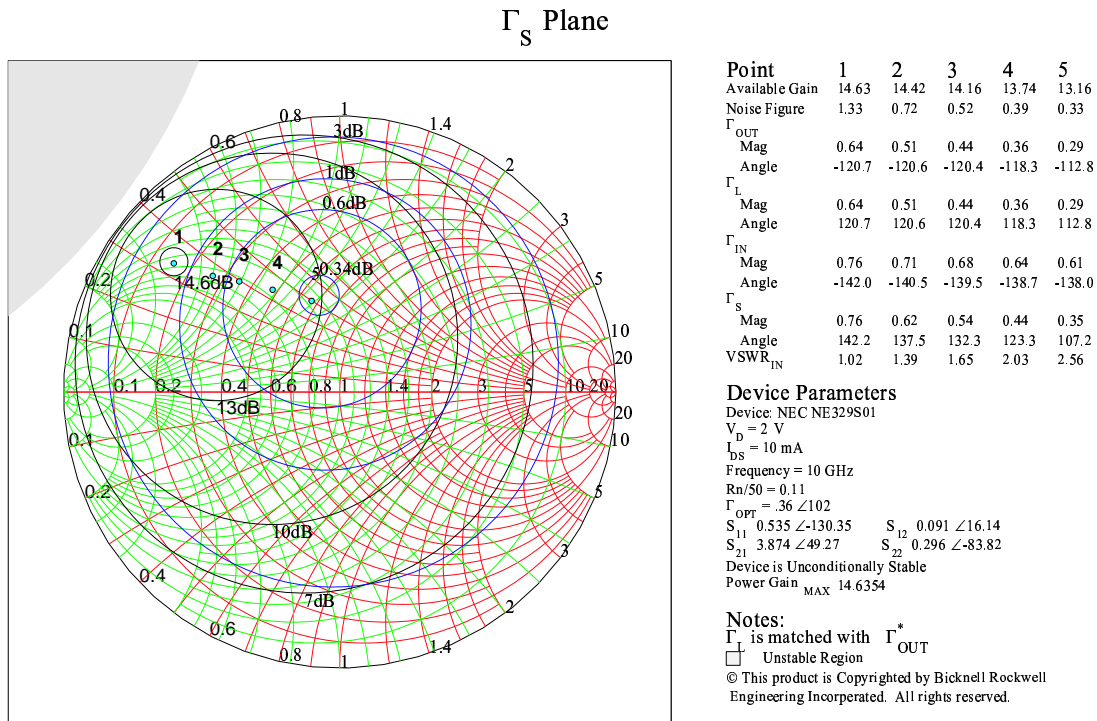


Figure 4.14: NE329S01 transistor source reflection plane biased at 2 Volts and 10 mA on the drain. FETs 1,2 and 3 are designed using this chart.

set independently. The interdigital dimensions listed in Table 4.3 are based on the geometry definitions specified in Figure A.8. Simulating the design in ADS as shown in Figure 4.17 showed that approximately the same results are achieved by using the parameters for MN4 in place of those for MN5.

The simulation shows a gain of 50 dB over 1.5 GHz of bandwidth and respectable matches on both the input and output. The measured performance of the two LNAs is shown in Figure 4.19, where a 40 dB attenuator is used to reduce the power level of the network analyzer. From 7 GHz to 11 GHz both amplifiers perform nearly the same, achieving a gain of 49 dB over the 9.8 to 10 GHz band with 1.2 dB variation. Variation found at the lower frequencies is due to a slight variation in the bias network filter components. The noise figure for each amplifier measured 4.1 and 3.6 dB. Figure 4.20 shows the LNA inside its case. Power is supplied through the

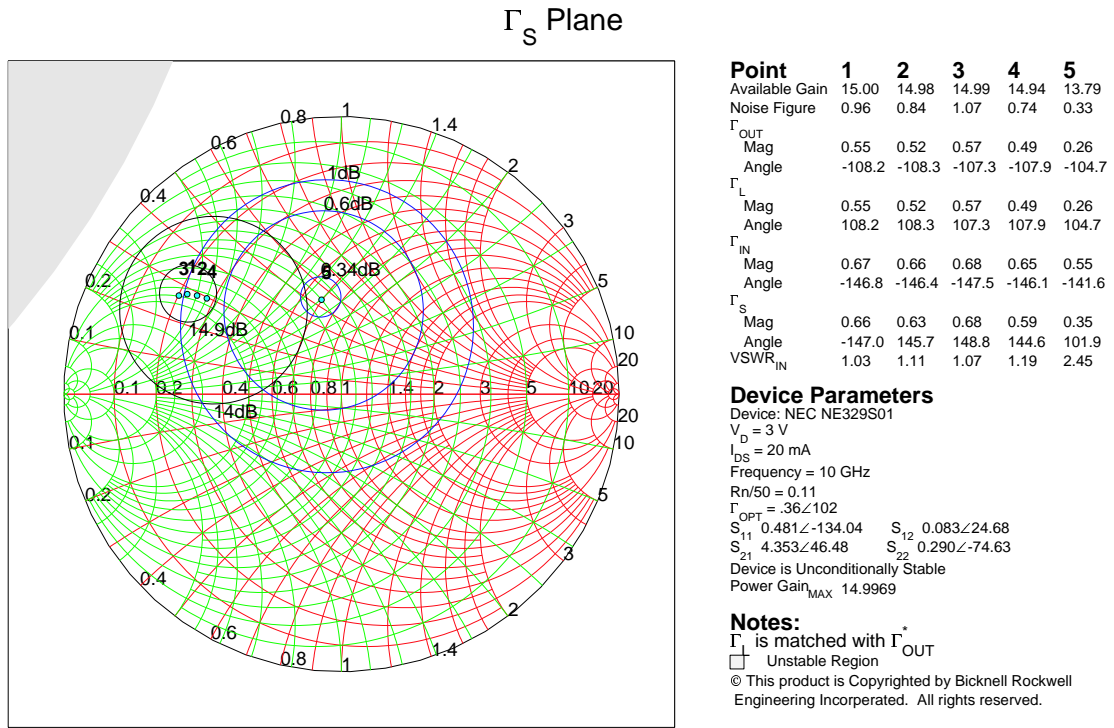


Figure 4.15: NE329S01 Transistor source reflection plane biased at 3 Volts and 20 mA on the drain. FET 4 is designed using this chart.

bottom of the case using filtered feed-throughs. Absorbing material is required on the lid of each case to eliminate oscillations that occur due to cavity effects.

### 4.3.2 RF Mixer Module

The HMC220S08 RF mixer made by Hittite Microwave is used because of its low cost and surface mount package. The device has LO and RF frequency range of 5.9 - 10 GHz, and the IF ranges from DC to 3.5 GHz at a 10 dBm LO drive level. It has a maximum noise figure of 10 dB and a maximum conversion loss of 10 dB. A small housing is machined out of aluminum to house the mixer alone as shown in Figure 4.21 with SMA connectors providing access to the LO, RF and IF ports.

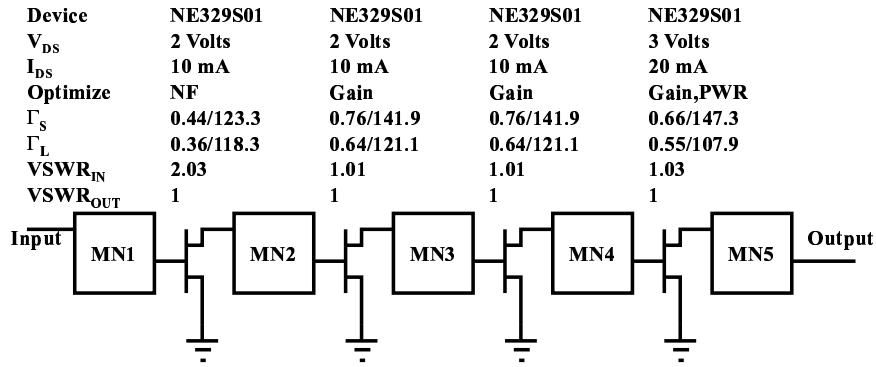


Figure 4.16: Matching Network and Transistor Setup for a 50 dB Low Noise Amplifier.

Table 4.3: Dimensions in mils of staggered interdigital capacitors used in matching networks of the LNA.

MN/Dim	1	2,3	4,5
A	9.5	9.5	9.5
B	9.5	9.5	9.5
C	9.5	9.5	9.5
D	9.5	9.5	9.5
E	158	168	88
F	100	131	161
G	90	55	120
H	150	140	180
I	90	55	120

### 4.3.3 IF Gain Module

The IF amplification and filter stage is contained in its own module. The IF from the RF mixer comes onto the board via a SMA connector and into a lowpass filter designed to knock out the RF frequencies. This filter is placed on a module so that it may be changed out easily for different corner frequencies. Next, the signal is gained up by 24 dB using a LM7121 video op-amp. The next stage uses the AD8321 amplifier with a gain range of -28 to 26 dB by 0.75 dB increments. The bandwidth of this device over all gain settings is 120 MHz. The gains are set by the user in the Visual Basic program and then sent to the PIC16C73A on the IF gain module.

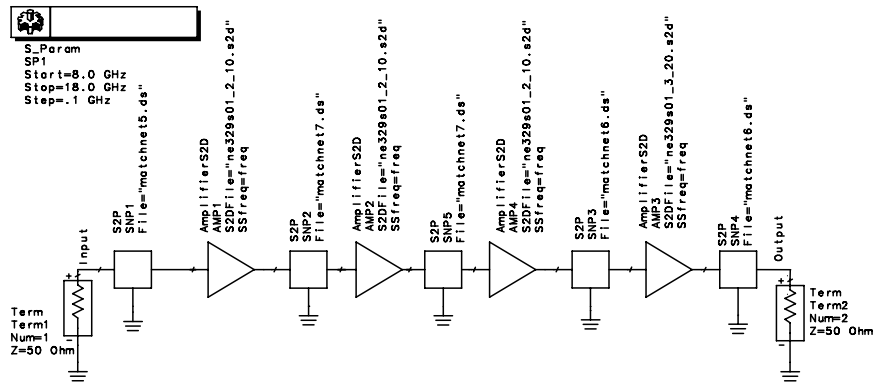


Figure 4.17: ADS Simulation of LNA.

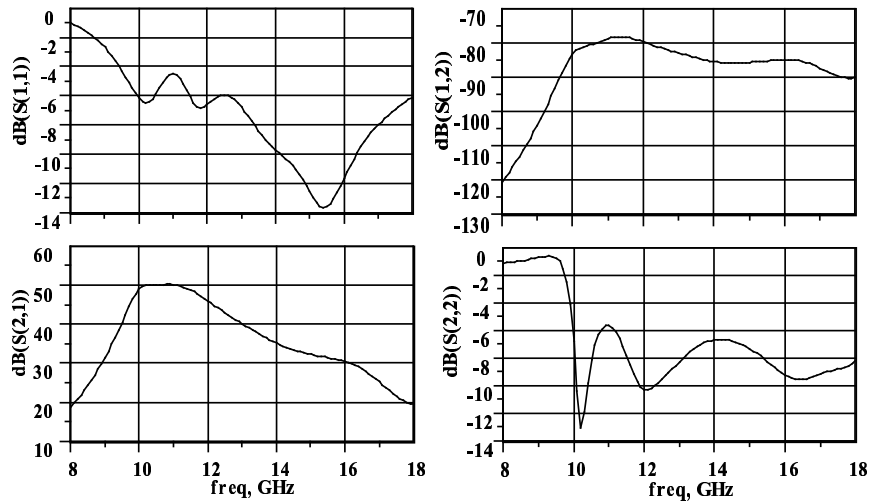


Figure 4.18: ADS Simulation Results for LNA.

The PIC then sends the setting to the amplifier via a SPI bus. The output of the amplifier goes into a standard 50Ω BNC Jack connection. This board did not operate correctly because the AD8321 does not have a high output power capability and would rail. This board is bypassed while acquiring images and a Stanford instrumentation programmable gain amplifier and filter is used in its place.

#### 4.4 System Assembly

The radar fits compactly together into a single box with few connections. The mixers and LNAs join to the transmitter module through SMA connectors as shown



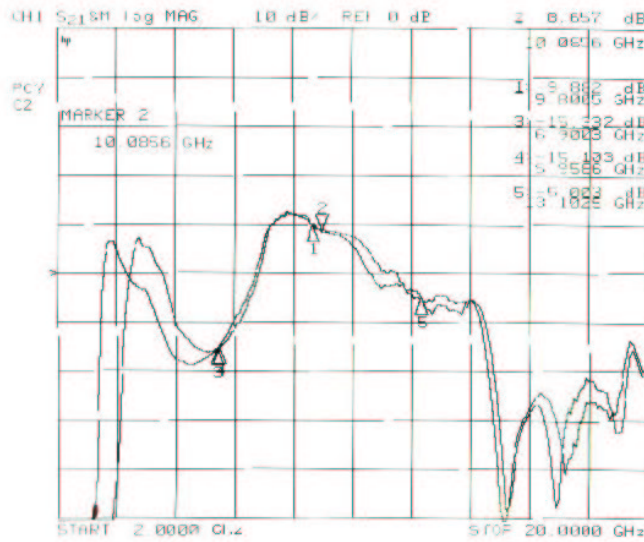


Figure 4.19: Measurements of 10 GHz Low Noise Amplifier with 50 dB of Gain.

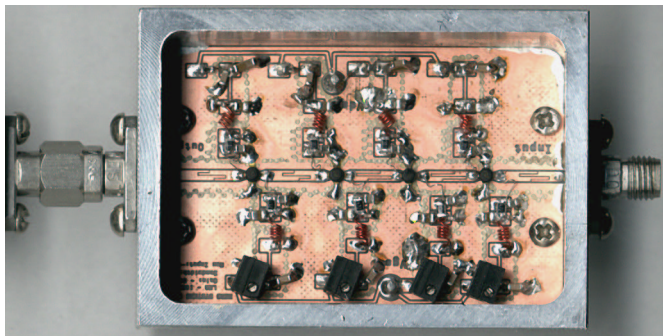


Figure 4.20: 10 GHz Low Noise Amplifier with 50 dB of Gain.

in Figures 4.23 and 4.24. Feed-throughs and connectors match up to sockets and jacks located on the main driver board, while antenna connections are made using coax cabling. The IF from the mixers are routed to the IF gain module through semirigid coax cable. This kind of modular design is easy to debug and enables the rapid switching of components that are not operating correctly.

The antennas for this system are the same as used by the YINSAR system. They are a slotted waveguide design that forms the azimuth beam, and an attached horn forms the the vertical beam [15]. The center frequency for these antennas is 9.9

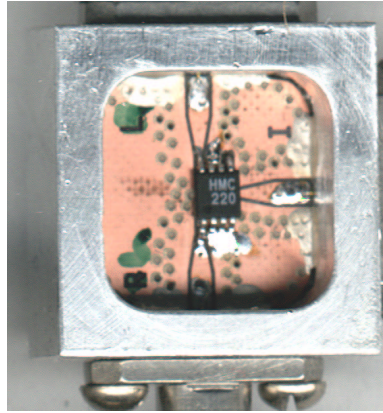


Figure 4.21: HMC220S08 Mixer in Housing.

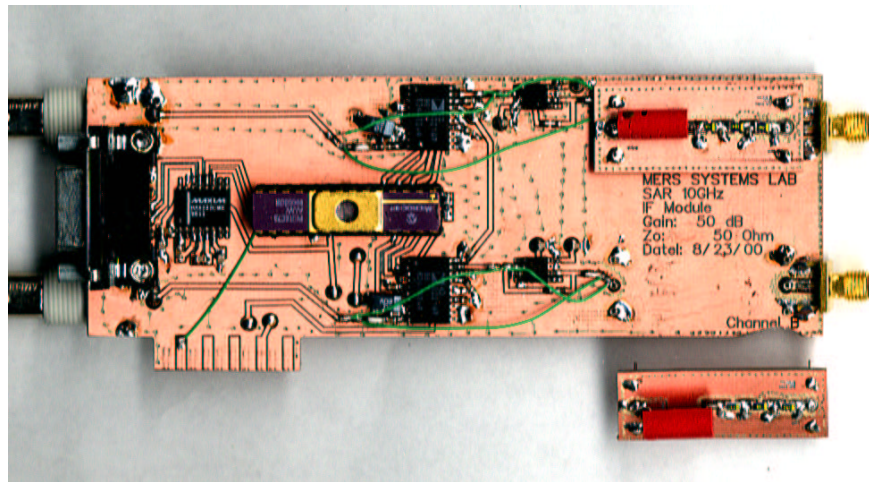


Figure 4.22: IF Filter and Amplification Module.

GHz with an azimuth beamwidth of  $10^\circ$  and vertical beamwidth of  $45^\circ$ . The transmit and receive antennas are all identical. Figure 4.25 shows the complete radar with all modules in place.

#### 4.5 Signal to Noise Analysis

This section derives the necessary equations to calculate the SNR of a SAR. The radar equation is used to calculate the expected receive power using the airborne

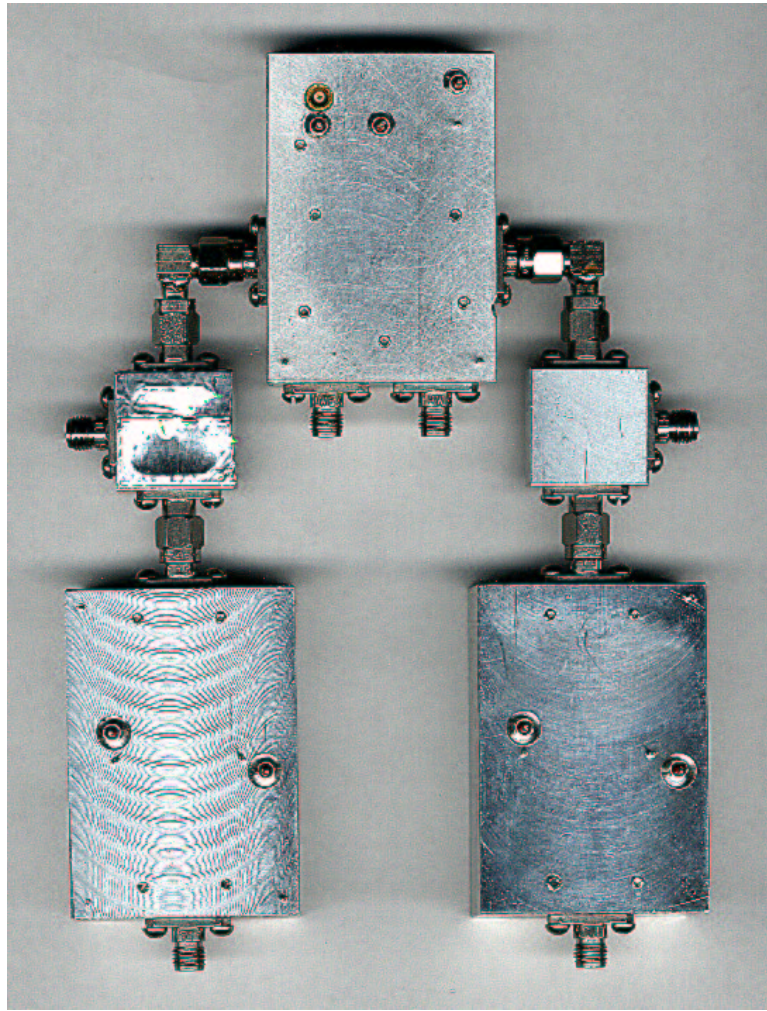


Figure 4.23: Bottom View of RF Subassembly

system parameters defined earlier in the specifications. The maximum expected radiometric noise is approximated and added to the calculated thermal noise generated by the receiver. The SNR is then calculated using airborne BY $\mu$ SAR parameters. The track parameters will yield a much higher SNR because the backscatter coefficient is higher for urban terrains and the range is shorter.



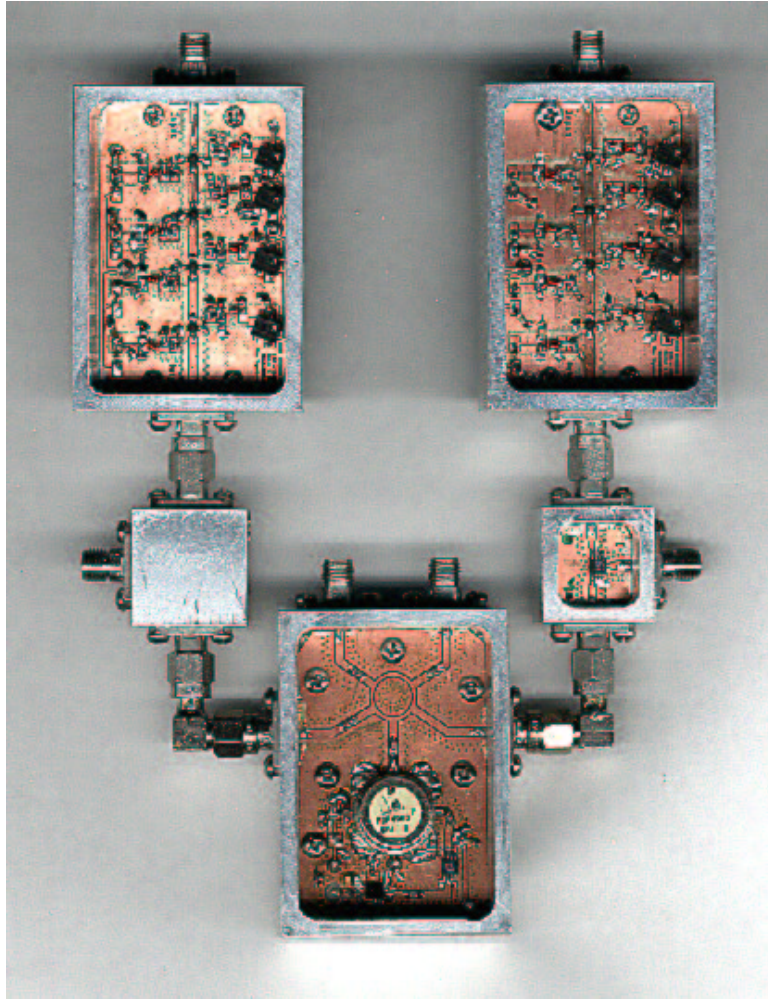


Figure 4.24: Top View of RF Subassembly

#### 4.5.1 The Radar Equation

The amount of transmit power that is required for a given system is found using fundamental equations. First, the power density  $S_t$  is calculate at a slant range  $R_s$  from a transmitter.

$$S_t = \frac{P_t G_t}{4\pi R_s^2} \left( \frac{W}{m^2} \right), \quad (4.5)$$

where  $P_t$  is the amount power delivered to the antenna and  $G_t$  is the gain of the receive antenna. The electric field  $E$  at the range  $R_s$  is related to the power density

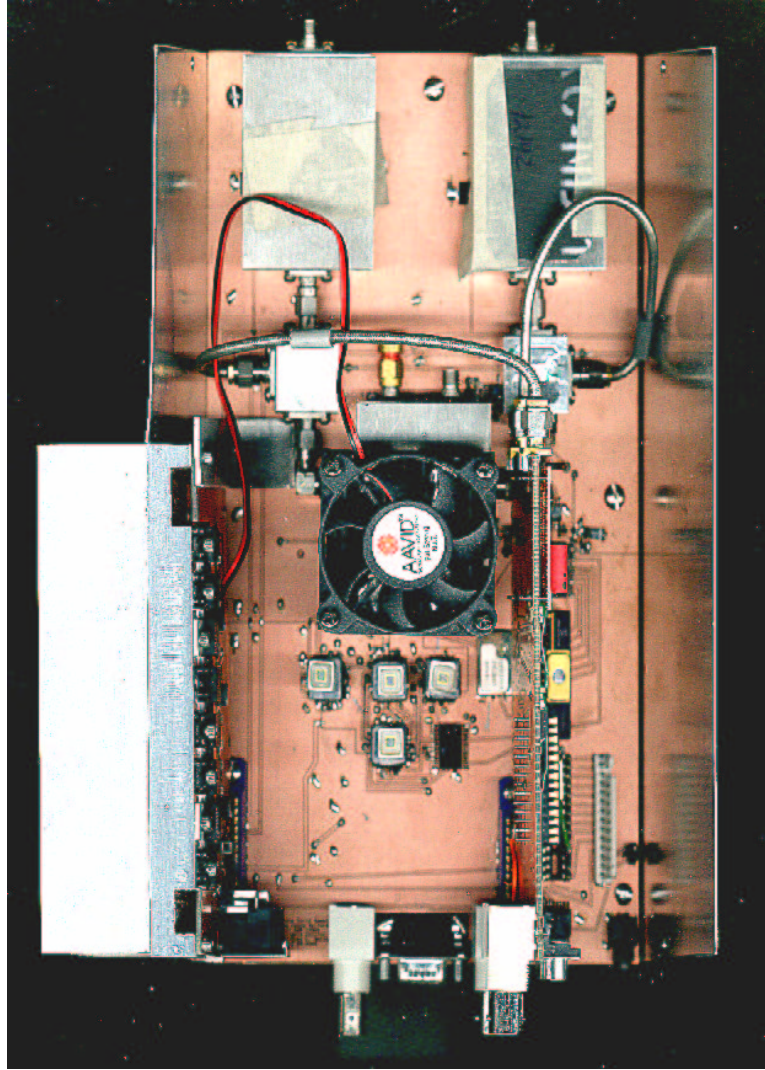


Figure 4.25: Complete SAR System with all Modules in Place.

$S$  by

$$S = \frac{E^2}{\eta} \left( \frac{W}{m^2} \right), \quad (4.6)$$

where  $\eta = 120\pi \Omega$  and is the intrinsic impedance of the atmosphere. The power captured by the receive antenna  $P_r$  is related to the power density by the effective area  $A_e$  as follows:

$$P_r = SA_e \quad (W). \quad (4.7)$$

This effective area is also related to gain of the receive antenna  $G_r$  and the carrier wavelength  $\lambda$  by

$$A_e = \frac{\lambda^2 G_r}{4\pi} \quad (m^2). \quad (4.8)$$

In a microwave communications link the power received  $P_r$  is related to the power transmitted  $P_t$  by the Friis power transmission Equation [38]

$$P_r = P_t \frac{G_t G_r \lambda^2}{(4\pi R_s)^2}, \quad (4.9)$$

Here the antenna mismatch is not included, and it is assumed that the antennas are polarized with each other. This is also assuming a non-obstructed path for the signal to travel through the air[1].

The radar equation changes slightly. A given target in the field will capture some of the energy and then reradiate it in all directions. The amount that is radiated in a given direction will be a function of the target's material composition and geometrical shape and size. It is called the radar cross section  $\sigma$ , but the surface scattering coefficient  $\sigma^\circ$  is commonly used for terrain classification and it is related to  $\sigma$  by

$$\sigma = \sigma^\circ A_{res}, \quad (4.10)$$

where  $A_{res}$  is the product of the azimuth and range resolution size.

There is imposed another loss range loss term  $1/4\pi R_s^2$  because the signal is reradiated which results in a received power of

$$P_r = \frac{P_t G_t G_r \lambda^2 \sigma^\circ A_{res}}{(4\pi)^3 R_s^4}. \quad (4.11)$$

The received power  $P_r$  is the amount of power delivered to the receiver from the antenna.  $\sigma^\circ$  is the quantity that is to be measured, and a range of values can vary from -25dB to 20dB. The other variables in Equation 4.11 are system design parameters. The amount of radiometric and thermal noise that is expected in the system must be calculated in order to determine the amount of transmit power needed. The physics of the system must be examined and the necessary assumptions stated that will

generate a rough calculation of the system parameters in order to ensure that the reflected signal from a target is larger than the thermal noise.

#### 4.5.2 Radiometric Noise

The problem is illustrated in Figure 4.26 where a footprint is radiated by a transmitter. The receive antenna not only collects the intended reflection but also the radiometric apparent temperature  $T_{AP}$ . This section will analyze the noise introduced by radiometric contributions.

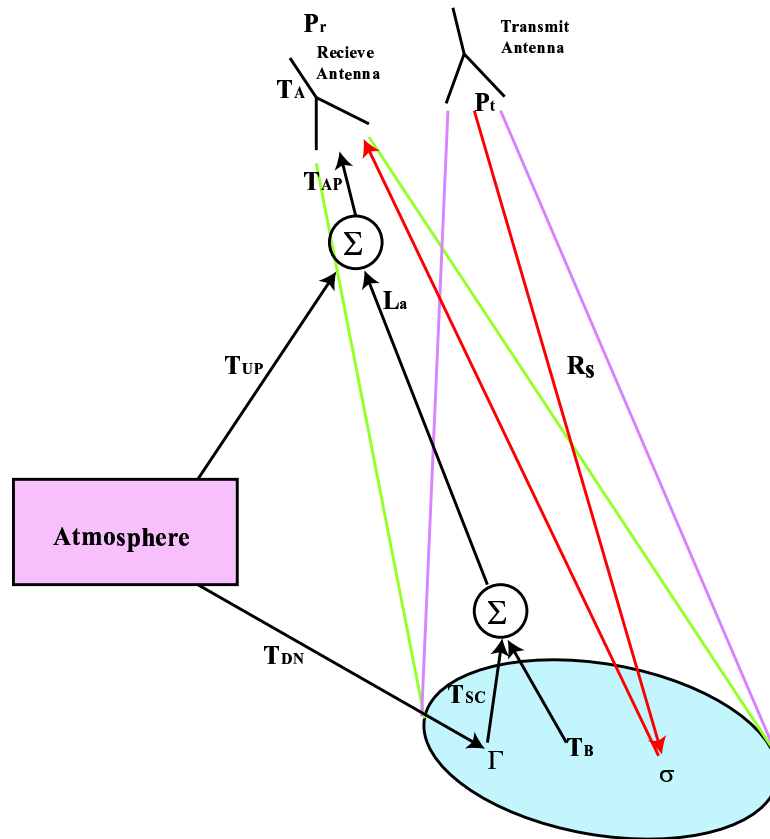


Figure 4.26: Radars receive reflected signals from the transmitter as well as radiometric energy that appears as noise. The radiometric parameters are expressed as temperatures where the coherent microwave signals are expressed as powers.

The total noise power at the input of the receiver  $P_{Ni,Tot}$  is expressed as a function of temperature

$$P_{Ni,Tot} = kB(T_A + T_{TL} + L_{TL}T_{rec}), \quad (4.12)$$

where  $T_A$  is the detectable antenna temperature,  $T_{TL}$  is the effective temperature of a lossy transmission line,  $L_{TL}$  is the loss of the line, and  $T_{rec}$  is the effective temperature of the receiver as seen at its input.  $B$  is the noise bandwidth and  $k$  is Boltzmann's constant. The detectable antenna temperature is related to the antenna efficiency  $\eta_l$ , the apparent temperature  $T_{AP}$ , and the antenna's physical temperature  $T_p$  by

$$T_A = \eta_l T_{AP} + (1 - \eta_l) T_p. \quad (4.13)$$

The transmission line temperature is related to its physical temperature  $T_P$  and its loss by

$$T_{TL} = (L - 1)T_P. \quad (4.14)$$

The apparent temperature  $T_{AP}$  as seen by the antenna is given by

$$T_{AP} = \frac{1}{L_a} [T_B + T_{SC}] + T_{UP}. \quad (4.15)$$

The loss term  $L_a$  is a function of frequency and distance. This term is expected to be negligible and will be assumed to be 1 at a 10 km range and 10 GHz. The brightness temperature  $T_B$  is related to the actual temperature of the ground  $T$  and emissivity  $e$  by

$$T_B(\theta, \phi, f) = T e(\theta, \phi, f). \quad (4.16)$$

The emissivity ranges from 0.2 to 1 when the incident angle is between  $45^\circ$  and  $65^\circ$ . The emissivity can be set to 1 by assuming the worst case.  $50^\circ C$  can be assumed as the hottest ground temperature.

The next term is called the downwelling scattered brightness  $T_{SC}$ , and represents the portion of radiation impinging on the surface from the upper atmosphere.



$T_{UP}$  is the upward emitted radiation due to the atmosphere. By assuming a lossless atmosphere both of these terms become negligible and are set to 0.

Equation 4.13 is simplified to

$$T_A = \eta_l T + (1 - \eta_l) T_p. \quad (4.17)$$

The noise power delivered by the antenna  $P'_A$  to the receiver is represented by

$$P'_A = k[\eta_l T + (1 - \eta_l) T_p] B, \quad (4.18)$$

### 4.5.3 Thermal Noise

The last contribution to  $P_{Ni,Tot}$  is by the receiver itself. Electrons within conductors are in a state of random motion which generates variations in voltage. This variation is called thermal noise.  $T_{rec}$  is calculated by knowing the noise temperature of each of the receiver subsystems. The noise temperature for the receiver is then calculated, and then the total noise power is defined for the system.

A common measurement of thermal noise is noise figure  $F$  defined as

$$F = \frac{P_{si}/P_{ni}}{P_{so}/P_{no}}, \quad (4.19)$$

$$= \frac{SNR_{in}}{SNR_{out}}. \quad (4.20)$$

The noise figure is defined by having the input to the receiver matched, and the matching element at  $290^\circ K$ . It can then be related to the equivalent noise temperature by

$$T = (F - 1)T_o, \quad (4.21)$$

where  $T_o = 290^\circ K$ .

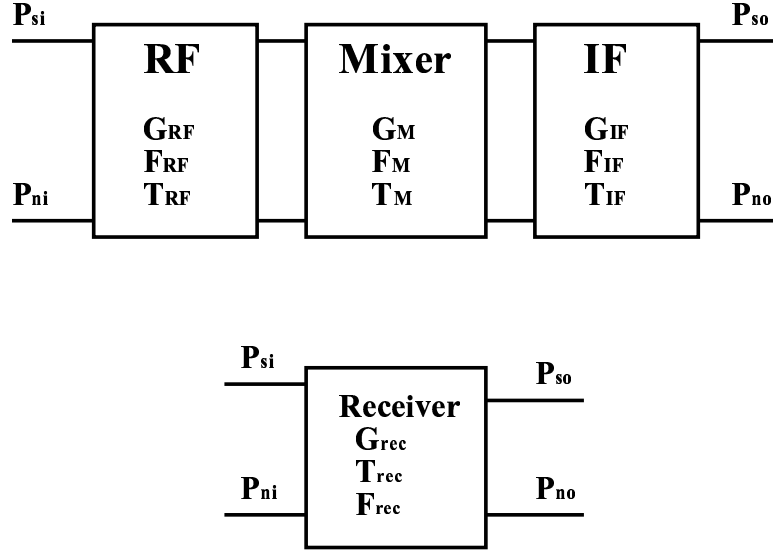


Figure 4.27: A typical receiver comprises a low noise RF amplifier, a mixer and a IF amplifier stage. Each stage has an associated gain, thermal noise temperature and noise figure. The entire system may be modeled as a single block as shown.

The three receiver parameters are related to the stage parameters by

$$G_{rec} = G_{RF}G_MG_{IF}, \quad (4.22)$$

$$F_{rec} = F_{RF} + \frac{F_M - 1}{G_{RF}} + \frac{F_{IF} - 1}{G_{RF}G_M}, \quad (4.23)$$

$$T_{rec} = T_{RF} + \frac{T_M}{G_{RF}} + \frac{T_{IF}}{G_{RF}G_M}. \quad (4.24)$$

The thermal noise can be controlled by designing the RF front end with the right gain and noise figure. Equation 4.23 shows that the RF amplifier sets the noise figure of the receiver if its gain is sufficient to minimize the effect of the following stages. The RF amplifier gain may be set so that

$$G_{RF} > 10 \frac{F_M - 1}{F_{RF} - 1} \quad (4.25)$$

holds true. This ensures that the RF amplifier is the main source of the receiver noise figure.

The total noise power at the receiver's input can be found given that the noise figure of each device is known along with the physical temperatures. The noise bandwidth  $B$  is determined by the RF bandwidth. The SNR is determined by using the time-bandwidth product  $T \cdot BW$  as processing gain [28]. The thermal and radiometric noise is cancelled due to their randomness. The radar signal is coherent and therefore experiences no cancellation. This is also true for the azimuth compression and can be represented by twice the value of  $n_o(R)$  as defined in Equation 3.76. The output signal to noise ratio becomes

$$SNR_{out} = \frac{P_r T \cdot BW 2n_o}{P_{Ni,Tot}}. \quad (4.26)$$

#### 4.5.4 SNR Calculations

The expected SNR for the airborne system can now be calculated using the parameters listed in Table 4.1 with an elevation of 600 m.

$$P_r = \frac{P_t G_t G_r \lambda^2 \sigma^\circ \Delta R \Delta a}{(4\pi)^3 R^4} \quad (4.27)$$

where  $R_{min}$  and  $\sigma_{max}^\circ$  are used for maximum SNR and  $R_{max}$  and  $\sigma_{min}^\circ$  for minimum SNR.

$$P_{r,min} = -2dBm + 17dB + 17dB - 25dB + 10\log_{10} \left( \frac{\Delta R_{max} \Delta a}{(4\pi)^3 R_{s,max}^4} \right), \quad (4.28)$$

$$= -161dBm, \quad (4.29)$$

$$P_{r,max} = -2dBm + 17dB + 17dB + 20dB + 10\log_{10} \left( \frac{\Delta R_{min} \Delta a}{(4\pi)^3 R_{s,min}^4} \right), \quad (4.30)$$

$$= -108dBm. \quad (4.31)$$

The processing gain for both azimuth and range compression is found by

$$PG_T = T \cdot BW 2n_o \quad (4.32)$$

$$= 10,000 \frac{\theta_a R}{vT} \quad (4.33)$$

$$PG_{T,Rmin} = 74dB, \quad (4.34)$$

$$PG_{T,Rmax} = 76dB. \quad (4.35)$$

The noise temperature of the receiver is

$$T_{rec} = T_{RF} + \frac{T_M}{G_{RF}} + \frac{T_{IF}}{G_{RF}G_M}, \quad (4.36)$$

$$= 435 + \frac{9(290)}{100,000} + \frac{9(290)}{10,000}, \quad (4.37)$$

$$\approx 435, \quad (4.38)$$

which shows that the noise is dominated by the noise figure of the RF amplifier. The total noise power at the input of the receiver is

$$P_{Ni,Tot} = kBW(T_A + T_{TL} + L_{TL}T_{rec}), \quad (4.39)$$

$$= 1.38 \times 10^{-23} 200 \times 10^6 (323^\circ K + (1.6 - 1)290^\circ K + 696^\circ K), \quad (4.40)$$

$$= -84.8dBm. \quad (4.41)$$

The signal to noise ratio is the sum of the received power from the radar signal and the processing gain minus the noise power expressed in dB as follows:

$$SNR_{out} = P_r + PG - P_{Ni,Tot}, \quad (4.42)$$

$$SNR_{out,min} = P_{r,min} + PG_{T,Rmax} - P_{Ni,Tot}, \quad (4.43)$$

$$= -161dBm + 76dB + 84.8dBm, \quad (4.44)$$

$$= -0.2dBm, \quad (4.45)$$

$$SNR_{out,max} = P_{r,max} + PG_{T,Rmin} - P_{Ni,Tot}, \quad (4.46)$$

$$= -108dBm + 74dB + 84.8dBm, \quad (4.47)$$

$$= 50.8dB. \quad (4.48)$$

Either the maximum range or the range of the backscatter coefficient will be limited by using the parameters chosen.

## Chapter 5

### BY $\mu$ SAR System Tests

Several tests are used to verify that the system performs as expected and can produce quality SAR images that have resolution which match the theoretical values calculated. Bench tests are performed that examine the transmitter's ability to generate a linear frequency modulation with a flat power response over the entire bandwidth. The next test verifies the range and azimuth resolution of the system by using a corner reflector mounted on a track. The last test images the roof of a building containing mechanical devices, to verify that the system can accurately image a known structure.

#### 5.1 Bench Tests

Three main bench tests verify the transmitter's ability to produce a linear FM signal and have a moderately flat power response. The first test is to verify that the phase counting circuit can accurately measure the frequency of the VCO over the bandwidth of interest without instability. The second test is a delay line test that gives indication to the linearity of the chirp and the overall RF system power response as a function of frequency. The third test measures the spectral output of each port on the transmit module.

##### 5.1.1 Phase Counter

The phase counter on the main board is tested for drive power limitations, frequency range, and count accuracy. A test board with only the phase counting circuit is first used and then the main board phase circuit is tested as illustrated

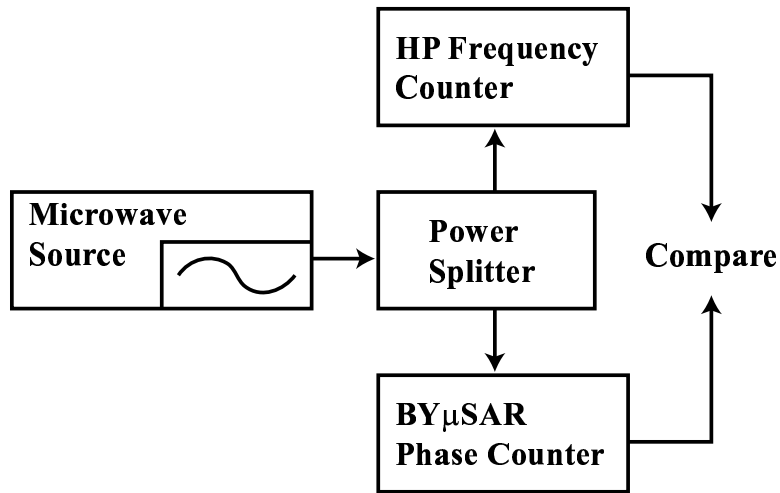


Figure 5.1: Setup for verifying the accuracy of the SAR's phase counting circuit.

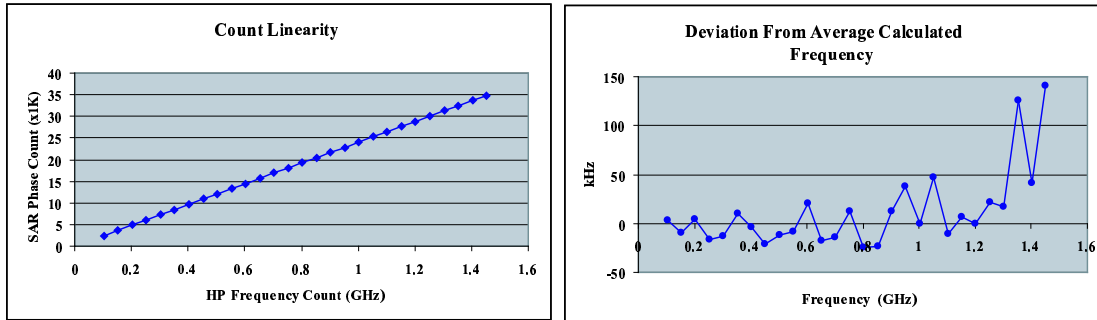


Figure 5.2: Measurement of linearity of phase counter using a HP frequency counter. Lower plot shows the deviation of the calculated frequency from the averaged calculated frequency in kHz.

in Figure 5.1 . The maximum drive power sensitivity of the counter is found to be -10 dBm while it is able to count up to 1.4 GHz with less than 140 kHz error. The count accuracy in Figure 5.2 shows that the counter works well up to 1.3 GHz with a maximum error of 50 kHz over a 1.3 GHz bandwidth.

### 5.1.2 Impulse Response

The impulse response test using a 17 m coaxial transmission line to simulate a single target at a fixed range is shown in Figure 5.3. The test gives an indication

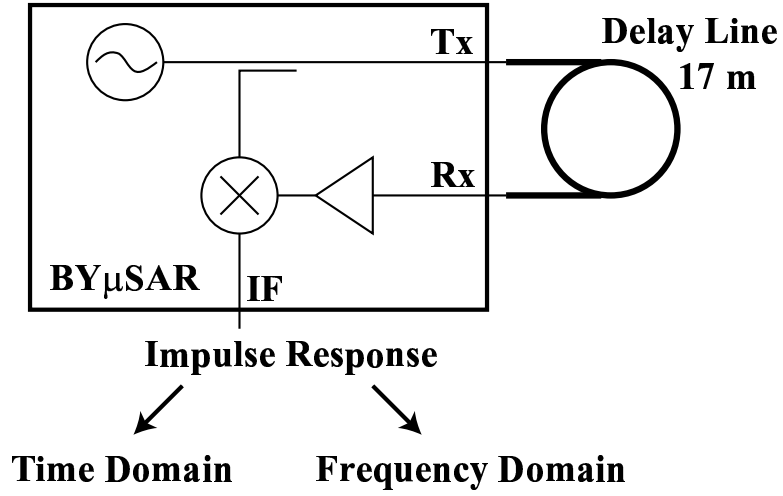


Figure 5.3: Test Setup for the Impulse Response.

of the FM signal linearity in frequency, and the overall system linearity in power. The coax is connected to the transmit port and one of the receive ports with the proper amount of attenuation. The real-time waveform is windowed with a rectangle whose width is 1.151 msec as shown in Figure 5.4. The window would be expected to produce a maximum frequency resolution of 874 Hz based on the Rayleigh criterion. The power variation measured between the beginning of the time domain waveform and the end is 3 dB. This power variation represents the total power variation in the whole system.

The time waveform is transformed to the frequency domain  $\tilde{X}[k]$  using the FFT and then interpolated using the interpolater [39]

$$X(e^{j\omega}) = \frac{1}{N} \sum_k \tilde{X}[k] \frac{\sin[(\omega N - 2\pi k)/2]}{\sin\{[\omega - (2\pi k/N)]/2\}} e^{-j[(N-1)/2](\omega - 2\pi k/N)}, \quad (5.1)$$

and displayed in Figure 5.4. The 3 dB resolution is approximately 766 Hz and the null to null divide-by-two resolution is 874 Hz. The measured resolution is exactly the same as the expected, indicating that the transmitter signal is linear in frequency over time.



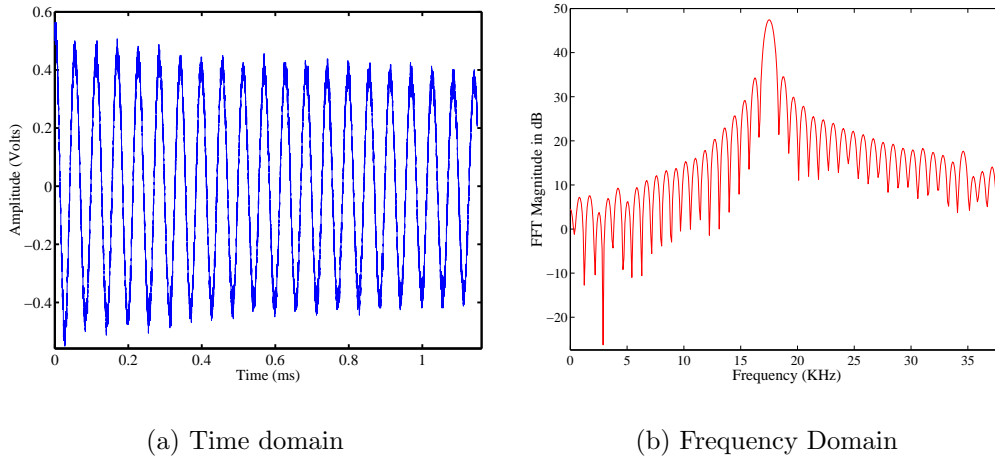


Figure 5.4: Figure (a) shows the time domain response for the impulse response test which shows the linearity of power for the whole system. The FFT of impulse response shown in figure (b) is found using a rectangular window. The impulse resolution is 874 Hz.

### 5.1.3 Transmitter Spectral Output

The transmitter spectral output is measured with an HP spectrum analyzer. The cable used to make the measurements has a 1.8 dB loss at 10 GHz and this factor is taken into consideration in Table 5.1. The LO ports have matched power of 9 dBm at 10 GHz on both 2 and 4. The other two ports 3 and 5 have 0 and -2 dBm of power at 10 GHz respectively, as is expected. Either port will work suitably for the transmit antenna feed. The harmonically related signals are higher than the desired level, and should be filtered out. The selective frequency response of the antennas will provide some filtering.

## 5.2 Inverse SAR of Corner Reflector

The quality of compression in range and azimuth is verified using a corner reflector. The reflector provides a near point target response in both dimensions. Examination is made of the range and azimuth cross-sections of the fully compressed image which shows the quality of the resolution in both directions.

Table 5.1: Measurements made of the RF module output ports in dBm. The ports are defined the same as Figure A.6.

Freq(GHz)/Port	5	10	15	20
2	-15	9	-15	-23
3	-15	0	-21	-23
4	-16	9	-15	-23
5	-15	-2	-19	-22

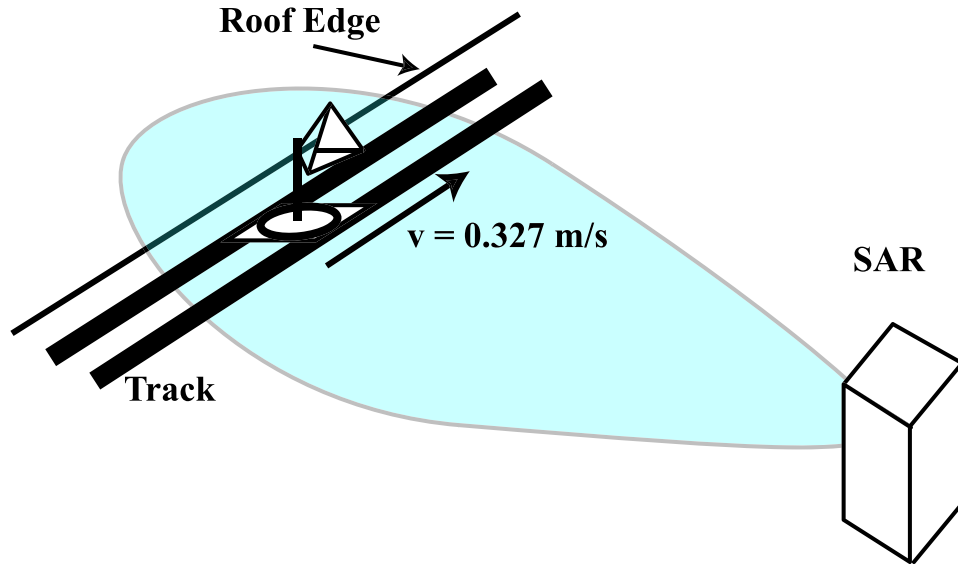


Figure 5.5: BY $\mu$ SAR is Stationary While it Images a Moving Corner Reflector.

A corner reflector has a bright, narrow response which is easy to detect in an image. This is commonly known as inverse SAR where the target is moving and the radar is stationary. The imaging takes place on the roof of the Clyde Building at BYU with the SAR set back about 12 m from the track as shown in Figure 5.5. The multipath type response in the magnitude plot is expected for the given environment, but should be more like the rectangle shown in Figure 5.6 for airborne imaging. The phase plot is essentially the same as the expected response ignoring the shift in time and problems in the phase unwrapping.

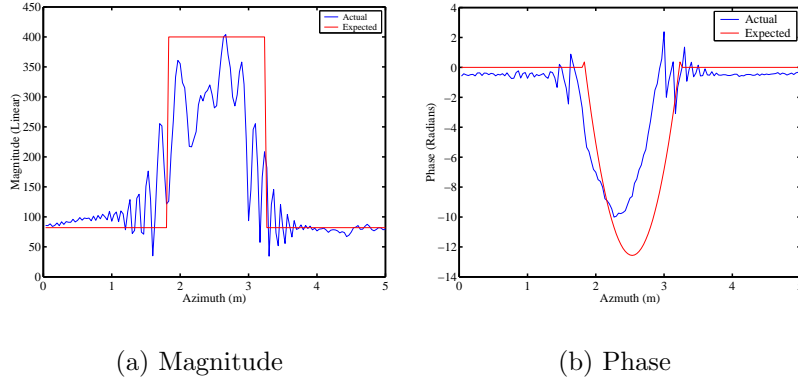


Figure 5.6: Azimuthal magnitude and phase response of from a moving corner reflector.

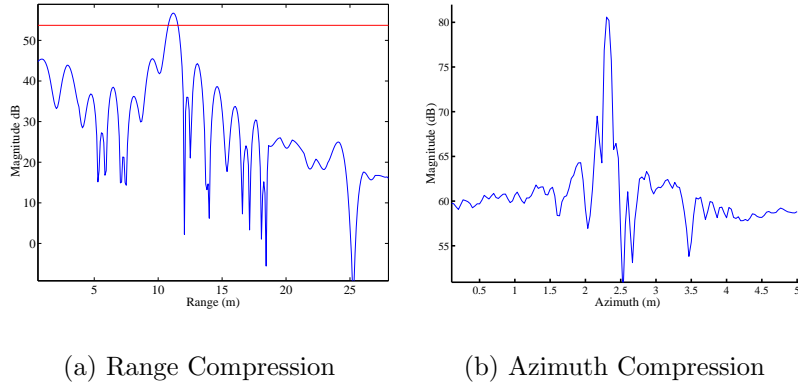


Figure 5.7: Range resolution is shown to be approximately 0.75 m at the 3 dB beamwidth, and the azimuth resolution is approximately 0.10 m which matches the expected values.

The effectiveness of the range compression is checked by plotting the magnitude response of the range compressed signal as a function of range when the corner reflector is in the middle of the radar beam, as shown in Figure 5.7 (a). This plot shows that the target is 0.75 m wide in range, and this is equal to the theoretical range resolution. The azimuth compression is checked by plotting the magnitude response of the fully compressed signal as a function of azimuth at the fixed range of 12m as seen in Figure 5.7 (b). The 3 dB beamwidth of the signal is 0.10 m, equalling the expected azimuth resolution.

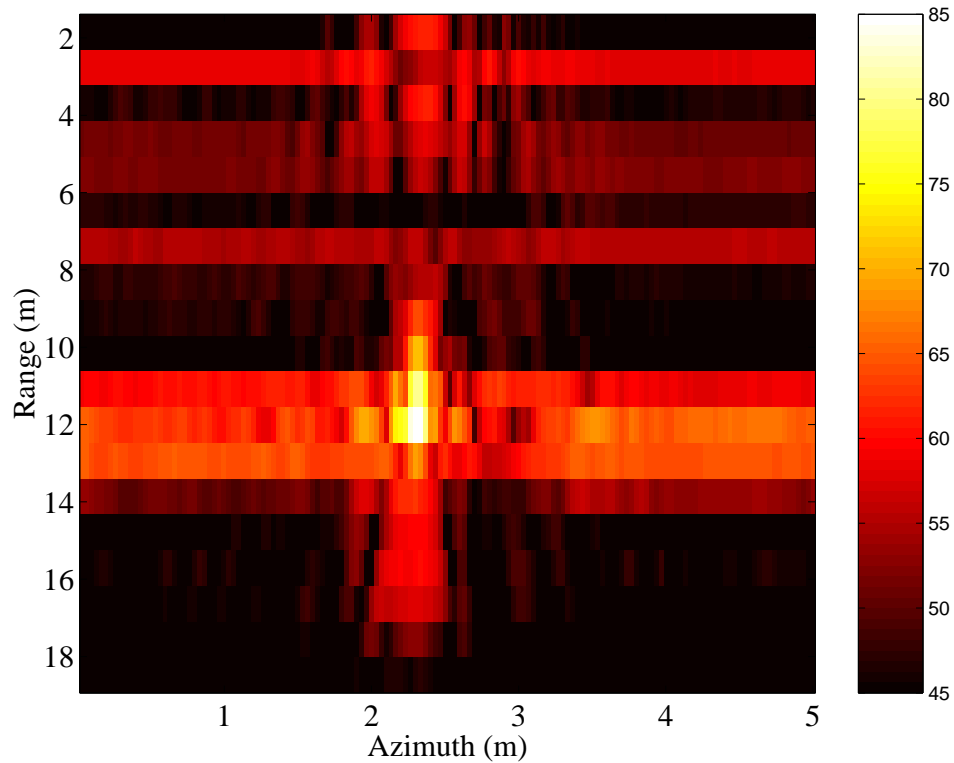


Figure 5.8: Range and azimuth compressed image of a corner reflector with scale in dB.

Figure 5.8 shows the image of the corner reflector resulting from range and azimuth compression. The image shows spreading in range due to the finite length of the window in range. This effect is masked in azimuth because of the superposition of the corner reflectors response and the reflections received from the track. The near range is also cluttered with obstructions that give a constant response over azimuth. The image and compression plots show that the  $BY\mu$ SAR achieves the resolution for which it is designed.

### 5.3 Imaging using Track Platform

The SAR's capability to image a scene is verified using a track mounted platform to move the radar. The data collected is processed and compared to photographs

highlighting significant targets. A zoomed section of the image taken by YINSAR in Figure 2.13 shows the same building that is imaged in this test, and a comparison is made between the two images.

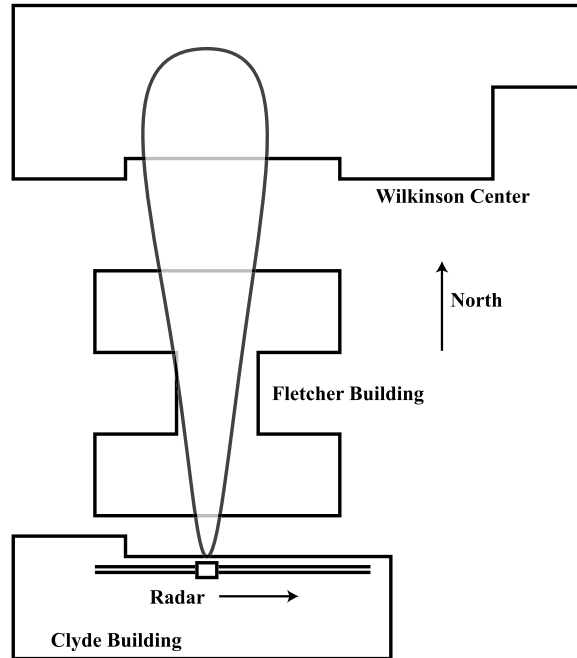
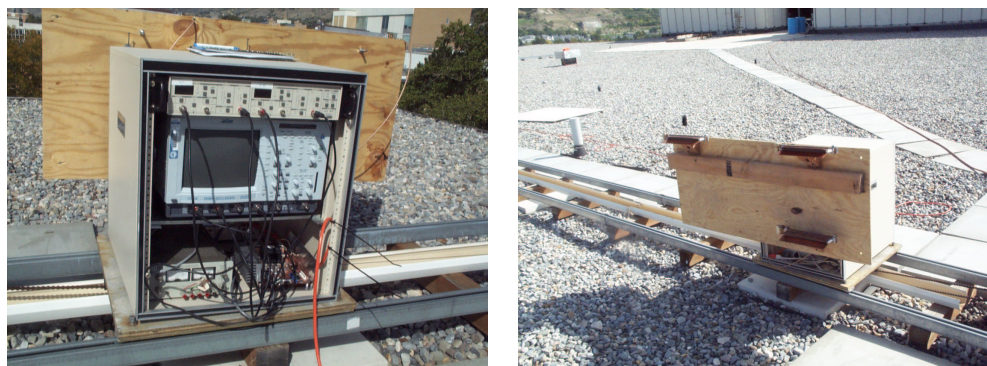


Figure 5.9: BY $\mu$ SAR on the Clyde Building imaging the Fletcher Building and Wilkinson Center to the North.

The SAR unit is mounted on top the track platform on the Clyde Building facing north. Parts of the Fletcher Building and Wilkinson Center to the north are imaged, as illustrated in Figure 5.9. The SAR is set up in a rack mount case with an instrumentation amplifier and an acquiring oscilloscope to digitize the waveforms as shown in Figure 5.10. One transmit and two receive antennas mounted on a sheet of plywood are all identical in performance, and are connected to the radar unit using coaxial cable. The tracks platform has difficulty moving uniformly down the track due to the weight of the rack and its contents. This motion smears the image but no corrective procedures are taken at this point.



(a) Data Acquisition

(b) Antennas

Figure 5.10: Radar setup for imaging. Data is collected using a oscilloscope and processed using Matlab.

Figure 5.11 is a combination of the radar image on the left and photographs on the right. Several objects are circled and numbered to identify objects that are common in each image. Many of the other objects are easily correlated using the marked ones. The flashings that border the edges of the building stand out and the tree casts a large shadow in range beyond itself.

The YINSAR image shown earlier in Figure 2.13 contains the roof of the Fletcher building. Figure 5.12 is a zoomed-in image of the Fletcher and Clyde buildings with part of the Wilkinson Center at the top. Some of the same targets appear in the YINSAR image as in the  $BY\mu SAR$  image. Not everything appears the same, however. The YINSAR image has a large, bright spot right in the middle of the Fletcher building at the location of the air conditioning unit marked "B" in the  $BY\mu SAR$  image. The main reason for the differences is that YINSAR is in an aircraft, imaging from north to south, and  $BY\mu SAR$  is imaging west to east on the track. The view from each platform is different, and the incident angles are also different. The aircraft is looking west, so shadows are cast on the west side of the buildings and brighter edges on the east are seen in both Figures 2.13 and 5.12.

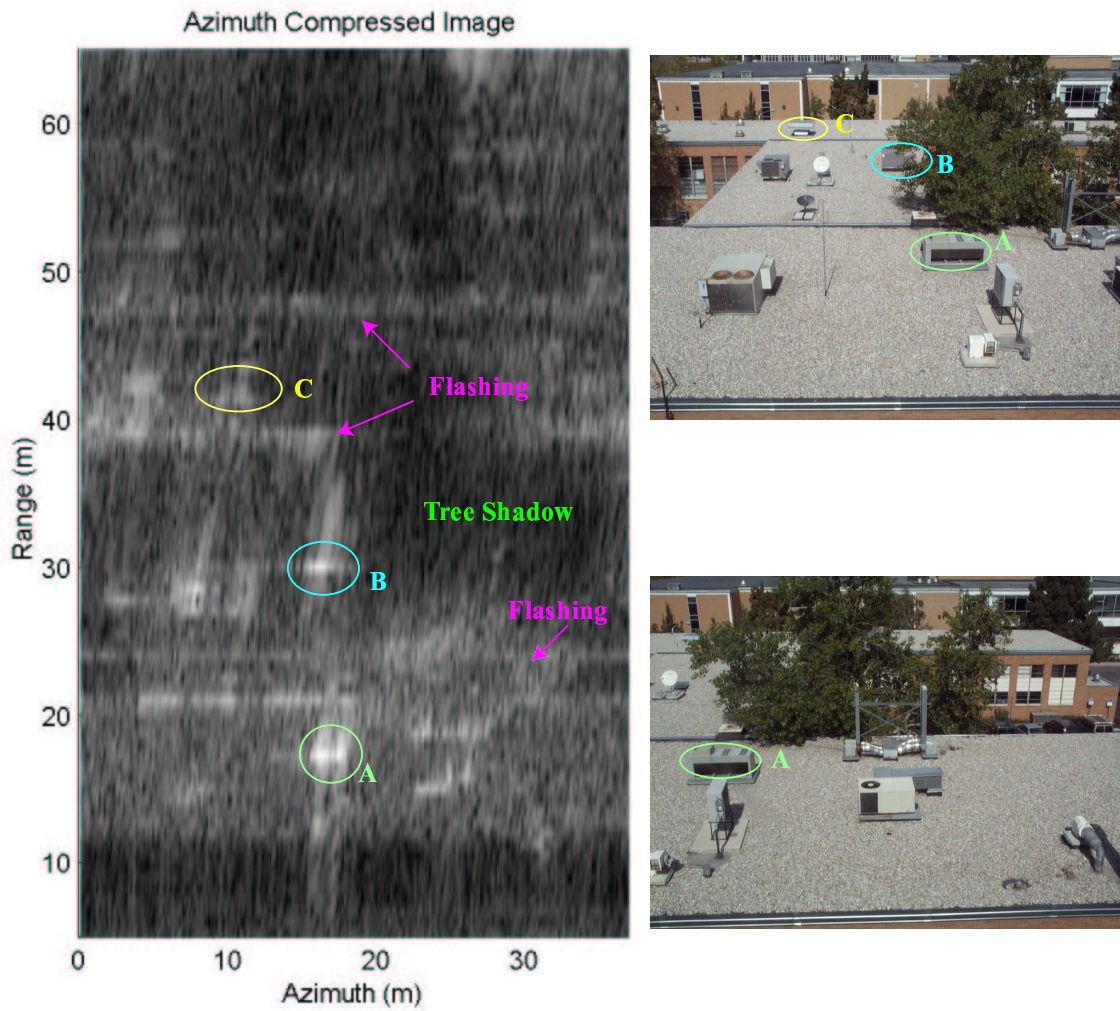


Figure 5.11: The SAR image and photographs are both taken looking north from the Clyde Building, imaging the top of the Fletcher building and beyond.



Figure 5.12: Image taken of Fletcher (top) and Clyde (lower) from YINSAR in the air.





## Chapter 6

### Conclusion

In conclusion, it has been shown that the BY $\mu$ SAR project is successful in developing new technologies that will affect the SAR community. Recommendations are given for the improvement of the SAR sensor and for microwave circuit development in a research setting. The contributions made by this thesis are then given.

#### 6.1 Summary

BY $\mu$ SAR is an innovative system developed on the success of three other SAR projects at BYU. It is the first SAR of its cost, size, weight, and power consumption to be developed which has excellent resolution. The use of FM/CW range compression in a SAR application makes this work unique. The transmit power is very low because it is compensated by the large processing gain achieved using a long chirp period. The signal is already compressed before it is digitized, reducing the cost and complexity of the digital acquisition. This thesis has addressed the question: What effects are found in compression due to using FM/CW techniques? It is shown that an increased linear shift in range walk occurs and an equation to solve for the shifted amount is given. In addition, it is proved that no phase errors are introduced within the specified bounds of operation.

A 10 GHz prototype unit is designed and built to validate these claims. The prototype's linear chirp waveform generator uses a novel technique in generating a quasi dynamic frequency to voltage mapping digitally. The system is successfully fabricated using coplanar technology that enables compact circuit design at high frequencies. Part of the research is to develop methods that allowed accurate design

of coplanar microwave circuits. A test fixture is built, and procedures are developed that make precise measurements of coplanar circuits possible.

The system design is composed of small module blocks that can be switched, making debugging easy. The entire unit fits compactly into a single box and is powered by a +/- 12 volt supply. Analysis is made on the system's SNR and shows that its specifications would allow excellent terrain mapping. The bench tests performed show that the radar has excellent linearity and a flat power response.

It is shown by using a corner reflector that the range and azimuth resolution of the prototype match the design specifications. A SAR image is also made of a building, and has good detail and contrast supporting that quality images can be expected from an airborne system.

## 6.2 Future Work

The radar system could be further reduced in size and complexity with expected advances in the development of microwave circuits on ICs. The IF gain module needs to be redesigned in conjunction with the design of a compact data acquisition system with a large memory storage capacity. The system could then be flown aboard an aircraft and larger data sets could be collected to further verify the system's performance.

In-flight processing should also be pursued by using a digital signal processing technology. Memory space for raw data is the same size as that of a processed image, making processing an attractive option for realtime image realization. Motion compensation should be studied for this type of system, and then the appropriate algorithms can be used to remove degenerate motion effects. This would allow the use of data while the instrument is imaging. Planar array antennas should be manufactured to increase compactness of the system and increase its reliability. These arrays would form fit into the skins or hull of a miniature aircraft making it suitable for use on UAVs.

It is recommended that a specification be made and followed for the development of future microwave sensors that allow the modulation type, center frequency

and bandwidth of systems to be easily changed or modified without the expense of a complete system redesign. This would reduce development cost and time. It would also increase quality, reliability, and flexibility of prototyping microwave sensors.

### **6.3 Contributions**

The work in this thesis introduces a new technique and sensor for SAR imaging. It is proved that within limits, FM/CW SAR introduces no azimuth phase errors, but increases a linear shift to range walk. A simple LFM signal generator is designed and developed that showed good linearity and fair frequency stability that finds use in several other systems at Brigham Young University.

Techniques to design and/make innovative coplanar circuits using relatively inexpensive equipment are developed. A high gain LNA is achieved using a low cost PCB substrate, and this gives confidence for the design of other technical building blocks of microwave circuits. The development of a modular style design is initiated where parts like the driver circuit could be reused in other designs helping to eliminate unnecessary design cost and effort.



## Appendix A

### Channelized Coplanar Waveguide Technology

Coplanar waveguide technology produces effective isolation, allows simple conductor geometries to realize fundamental circuit elements, and facilitates simple component placement. Coplanar is not used extensively in circuit design because of the difficulty in analyzing its behavior. This appendix will show an approach to developing circuits using coplanar technology. It begins with a discussion on its benefits, followed by the design of a  $50\Omega$  line, DC isolation circuits, basic elements. The final section covers the tools used for fabrication and issues in board design.

#### A.1 Coplanar's Benefits

Conductor Backed Coplanar Waveguide (CBCPW) is chosen to develop the main board and modules due to its strong confinement of electromagnetic energy and its ability to provide easy shunt and series part placement [40, 41]. A Finite Difference Time Domain (FDTD) solution is shown in Figure A.1. FDTD only considers the static field and does not include the energy found in parallel plate or waveguide modes. Channelized Coplanar Waveguide (CCPW) is realized by creating vias between the bottom and top conductors [42]. Parallel plate and rectangular waveguide modes within the dielectric are eliminated by choosing the position of the vias properly. Parallel plate wave modes also exist in microstrip due to the boundary created by the dielectric and air, which allows waves to propagate in the substrate. This contributes to transmission loss and crosstalk between lines. A large percentage of the energy in CPW transmission lines propagate in the slot mode, and this further reduces the amount of radiated energy into the air.

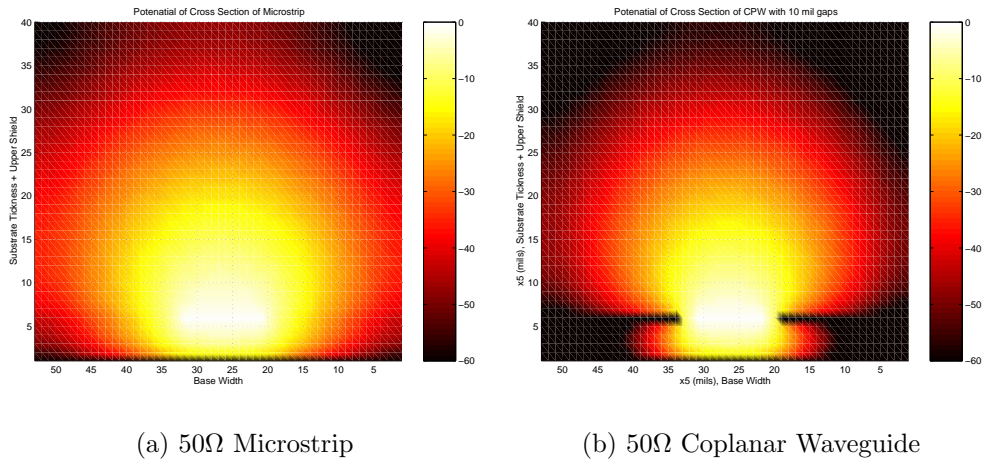
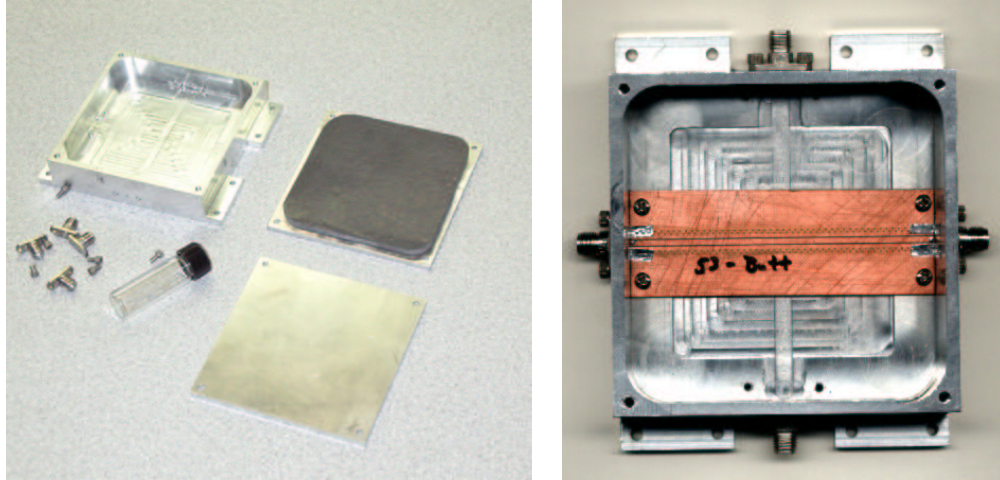


Figure A.1: Static solution of microstrip and coplanar technologies showing the difference in the amount of power they each radiate. This solution does not include the parallel plate mode or the slot mode waves.

Hewlett Packard’s simulation package Advanced Design System (ADS) provides excellent analyzation of numerous transmission lines and circuits including CPW, but testing physical CPW circuits is difficult because of poor coax to CPW transitions. A test box is designed and fabricated using aluminum and a Southwest Microwave connector is used to make the CPW to coax transition. Figure A.2 shows the 3”x3” test box with the four connectors along with absorbing lined and plain lids.

## A.2 50Ω Transmission Line

A 50Ω characteristic impedance transmission line 500 mils long is designed and simulated in ADS as shown Figure A.4. The parameters are based on a GIL1000 PC board with an effective permittivity of 3.2, a dielectric thickness of 30 mils, a loss tangent of 0.004, and double sided 1 oz copper clad. Figure A.3 shows the simulation model with 10 mil gaps in red rectangles, and a via strip in blue rectangles starting 25 mils from each edge of the gaps and a center conductor 53 mils wide. White in the image represents where the metal is not removed. The cutoff frequencies for each



(a) Test Kit

(b) Test of Transmission Line

Figure A.2: Figure (a) shows the test box used to analyze coplanar waveguide circuits. One lid shows a 3/8" absorbing liner while the other is not lined to analyze packaging effects. Figure (b) shows A S parameter test for a 53 mil transmission line with non-tapered connections to the connector signal pin. Aluminum tape is also used to connect the connector's RF ground with the ground of the circuit board.

mode of the dielectric filled channel are found by

$$f_{c(m,n)} = \frac{c}{2\pi\sqrt{\epsilon_r}} \sqrt{\left(\frac{m\pi}{a}\right)^2 + \left(\frac{n\pi}{b}\right)^2}. \quad (\text{A.1})$$

The first mode, TE, has a cutoff frequency of 26 GHz.

Several transmission lines with slight variations are tested along with the simulated design. Figure A.2 (b) shows the first test using a 53 mil line with neither end tapered where the connector attaches. Aluminum tape is seen making a RF ground connection between the board's ground plane and the ground of the box and connector. The tape improves the performance of the connection by several dB, but it is still unsatisfactory. Silver paste painted into the gap between the board and casing, as seen in Figure A.3, improves the connector performance significantly, yielding a 0.7 dB loss on  $S_{21}$  at 10 GHz. This is less than the loss simulated in ADS that accounts



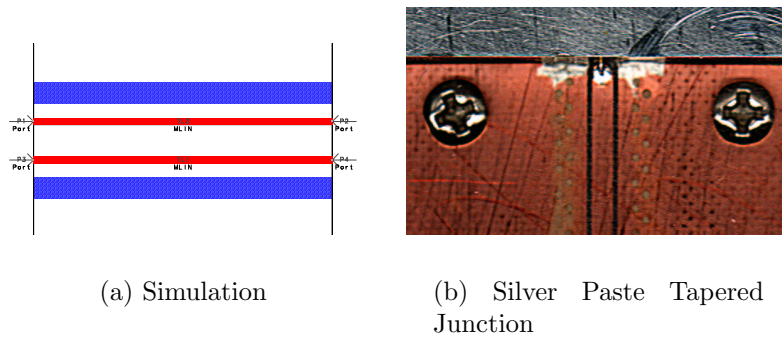


Figure A.3: Figure (a) shows the ADS simulation layout of a  $50\Omega$  transmission line built on 30 mil GILL1000 laminate. A tapered line junction of a transmission line with the connector is shown in figure (b). Also seen is the silver conductive paste used to make an excellent RF ground connection between the case and board.

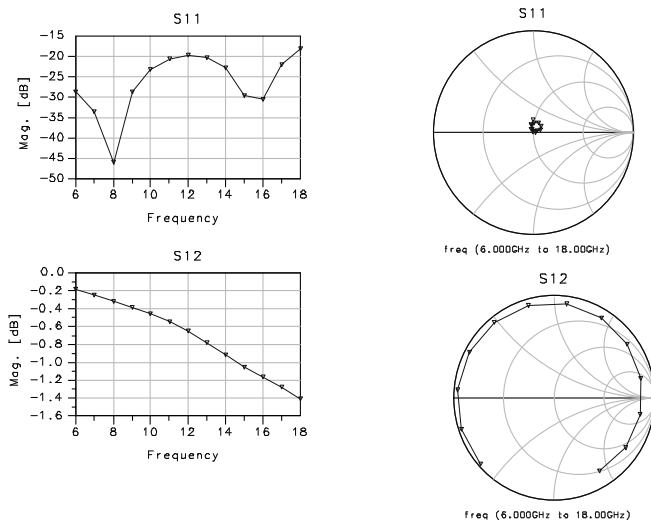
for the dielectric loss of the substrate. The transmission lines with variations each prove to be inferior to the 53 mil tapered line with vias spaced 25 mils from the edge of the gap. This verifies the accuracy of ADS's ability to simulate the performance of coplanar transmission lines.

### A.3 DC Isolation and Cavity Effects

A simple test board shown in Figure A.5 is built in order to test the effects of crosstalk on the board and in the test fixture. The results are shown in Table A.1.

The maximum coupling within the cavity is the same over the 6-16 GHz band without the lid and with the absorber lined lid. An extra 7 dB isolation is achieved at the 9.8-10GHz band by using the absorbed lid. Many resonances within the cavity occur when the lid without absorber is used, and this will raise the overall crosstalk power level. The transmission coefficient  $S_{31}$  shows no detectable change with or without the lid.

The ability to bias FETs with high isolation networks is crucial to eliminate the chance of the device becoming unstable. A bias network is designed to see what kind of isolation might be achieved. Figure A.5 (b) shows the board achieves a 50 dB

Figure A.4: ADS Momentum Simulation Results of a 50 $\Omega$  Line.

isolation while maintaining DC continuity on  $S_{32}$  and has a 0.8 dB transmission loss on  $S_{31}$ .

#### A.4 CCPW Elements

An unequal power divider is required that delivers most of the power from the VCO to two ports to supply the LO on the RF mixers. Another port is needed for the transmit signal. It is desirable to have short transmission lines to minimize loss. Wilkinson power splitters exhibit good power balance between each branch and provide excellent isolation between ports, but a coupler is needed as well. A homework problem in [38] shows a ringed coupler that has good coupling off two ports and low coupling off two others as seen in Figure A.6 (a).

The hybrid ring splits the majority of the power equally to ports 2 and 4 if the signal is injected at port 1. Ports 3 and 5 receive the remainder of the split. The measured S parameters are shown in Equation A.2. If the 1 dB drop in power over a 3" line is considered, these parameters would all be 1 dB higher. Sharp curves are

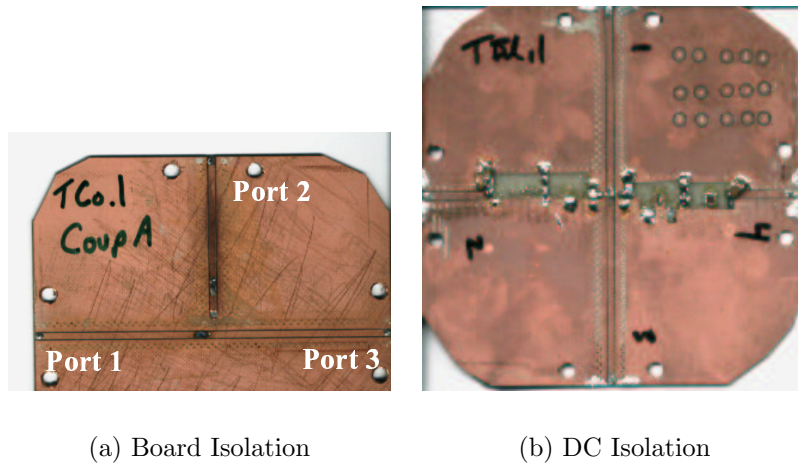


Figure A.5: Figure (a) shows a board used to examine isolation and cavity effects. A simple board used to achieve 50 dB isolation on a DC bias network is shown in Figure (b).

used to get the transmission lines to match the ports of the test fixture as shown in Figure A.6 (b). These tight curves cause phase mismatches between the coupled slots, and this degrades the transmission coefficient of the line. Values near -3dB might be achievable on  $S_{21}$  and  $S_{41}$  as is expected if these curves are eliminated. The coupling of the power into port 3 matched the amount desired.

$$[S_{meas}] = -1 \begin{bmatrix} 12 & 5.5 & 11 & 5 \\ 5.5 & & 6 & 14 \\ 11 & 6 & 12 & 5 \\ 5 & 14 & 5 & 15 \end{bmatrix} \quad (\text{A.2})$$

CPW gives circuit designers an easy tool to develop simple and compact matching networks. Series and shunt inductors or capacitors can be realized by the use of simple conductor geometries as shown in Figure A.7 [40, 42]. The suggested element representations are only a simplified model and do not include higher order effects. The series capacitor and inductor are referred to as an interdigital capacitor and an interdigital inductor because of the interleaving fingers. An attempt is made to in-

Table A.1: S parameter measurements taken to verify the amount of coupling with tangential coplanar lines inside a cavity. The lid designators are: N - no lid, Y - metal only lid, A - lid with absorber. The other two columns show the maximum S parameter value over the designated bandwidth.

S Parameter	Lid	6-16GHz max (dB)	9.8-10GHz max (dB)
$S_{21}$	N	-45	-47
$S_{21}$	Y	-32	-45
$S_{21}$	A	-45	-52
$S_{31}$	N	0	-1
$S_{31}$	A	0	-1

crease the transmission coefficient by adding as many fingers as physically practical, and by introducing a staggered section in the center that would allow longer sections of conductor material to be in parallel, and thus add to the coupling as shown in Figure A.8. The full s-parameters are simulated in ADS and show that the capacitor has a series self-resonance which is a function of the finger length. Increasing the length drops the self-resonance of the capacitor, indicating that it is only useful for frequencies where the wavelength is approximately a quarter of the finger length.

A matching network using an interdigital capacitor is made by reiteratively simulating the element in ADS and finding the point where the magnitude is correct while ignoring the phase. The magnitude is controlled by the length of the coupling fingers, and the phase is set by adjusting the distance between the matching port and the interdigital capacitor. The magnitude and phase are dependant on one another and so it takes several attempts to get both of them into a tolerable range.

## A.5 Prototypes and Developing

All of the boards in this thesis are built using LPKF's Proto91VS system in conjunction with their through plating system. Artwork is exported in Gerber format into CircuitCam where it is isolated and exported to the board plotter. First the drilling and milling are performed where the spindle has a variable speed motor

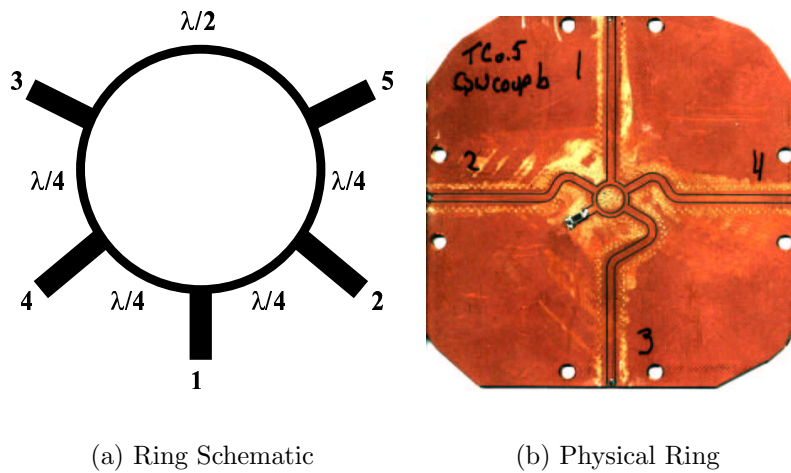


Figure A.6: Figure (a) shows the schematic to a hybrid ring that has  $Z_o$  impedance on each arm and  $\sqrt{2}Z_o$  impedance on the ring. The realized board design is shown in Figure (b) with one port terminated in  $50\Omega$  so it could work in the test fixture.

facilitating the use of a large variety of tools. Most of the previous designs use a 10 mil end mill and the interdigital designs use a 5 mil end mill to cut the coupling slot.

Milling tools with small diameters require a high spindle RPM to ensure proper tool operation. Plating follows next, by injecting conductive paste into the holes that are to be plated. Care must be taken to ensure that the paste does not enter into the milled slots. The board is then baked at  $100^\circ\text{C}$  for 30 minutes where the paste cures, and then the board is cut out of the stock material using a contour router.

The vias produced by the LPKF system have a high tendency to fail resulting in extensive circuit debugging problems. Eyelets are used to eliminate this problem for any signal or power via and the conductive paste is used for vias that confine RF signals. The time to install the eyelets pays for itself by minimizing circuit debug time and reducing intermittent failures.

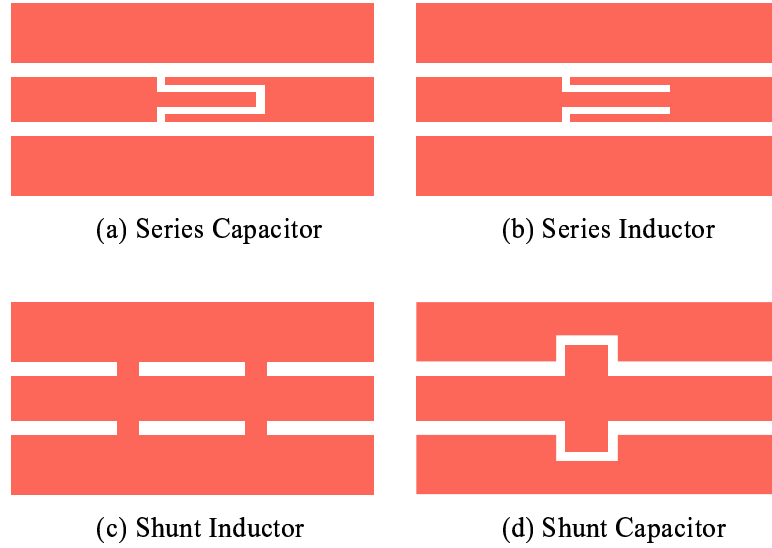


Figure A.7: Fundamental circuit elements are realized using simple geometries in CPW. These devices are compact and easy to design.

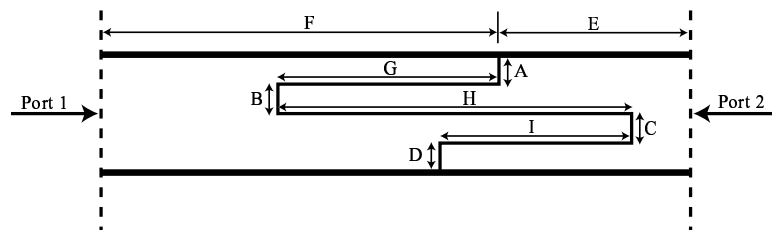


Figure A.8: The LNA matching networks were designed using this staggered interdigital capacitor.



## Appendix B

### SAR Imaging Functions

The following functions written in Matlab are used to process the SAR images. Compressor1.m is used to compress the data files for the corner reflector moving down the track. Compressor2.m is used to compress the data files the radar imaging while moving on the track. Azch2.m generates the matched filter for each range to enable the azimuth compression.

```
%compressor1.m
load sarimmich01.dat % Load Data File

%%%%%%%%%%%%%%%%%%%%%%%%%%%%%%%%%%%%%%%%%%%%%%%%%%%%%%%%%%%%%%%%%%%%%%%% RANGE COMPRESSION %%%%%%%%%
for k=1:150,
    fm = fft(sarimmich01((k-1)*502+1:k*502));
    abc=fm(1:250);
    im1(:,k) =abc;
end
RangeRes=0.75;
yz=[1:1:250].*RangeRes;
ll='r';

figure(31)
Fs1=500e3;T=1/Fs1;
N=10;dx=8;
[w,Y]= sincfilt(abs(im1(:,70)),dx,N,T);
YY=log10(abs(Y)).*20;
xyz=linspace(0,231,length(w));
plot(xyz,YY,'b',xyz,ones(1,length(w))*(max(YY)-3),'r-')

figure(32)
    imagesc((abs(im1(2:80,:))));
    title('Range Compressed Image');colorbar
    ylabel('Range')
```



```

        colormap(hot)

%%%%%%%%%%%%%%%%%%%%%%%%%%%%%%%%%%%%%%%%%%%%%%%%%%%%%%%%%%%%%%%%%%%%%%%% Azimuth Compression %%%%%%%%%
RangeRes=0.75; %in meters
AzRes = 0.10;
samples=150;
for k=2:250
    a=k;
    Ro=a*RangeRes;
    r=azch2(10,0.34,Ro,9.53,samples);
    fq=fft(im1(k,:));
    fr=fft(r);
    azf=fq.*(fr);
    im2(k,:) = fftshift(iffz(azf));
end

figure(33)
xz=[1:1:150]./30;
yz=[2:1:20].*0.924;
imagesc(xz,yz,20*log10((abs(im2(2:20,:)))));
title('Azimuth Compressed Image');
caxis([35 85])
colorbar
colormap(jet)
ylabel('Range (m)')
xlabel('Azimuth (m)')

figure(34)
plot(xz,unwrap(angle(im1(12,:)),1.5*pi),xz,...
unwrap(-angle(azch2(10,0.34,12*RangeRes,9.53,samples)),1.5*pi))

figure(35)
plot(xz,abs(im1(12,:)),xz,318.*abs(azch2(10,0.34,12*...
RangeRes,9.53,samples))+82)

figure(36)
plot(xz,20*log10(abs(im2(12,:))))
axis([0 15 50 85])

*****
*****
*****

%compressor2.m
load hannah2.dat % Load Data File

```

```

azsamp = 372;

% RANGE COMPRESSION
for k=1:azsamp,
    fm = fft(hannah2((k-1)*250+1:k*250));
    abc=fm(1:250);
    im1(:,k) =abc;
end figure(31)
    plot(20*log10(abs(im1)));
    title('Absolute Value of each Range Line')
figure(32)
    imagesc((abs(im1(2:80,:))));
    title('Range Compressed Image');colorbar
    ylabel('Range in Samples, .75 meters per sample')
    colormap(jet)

% Azimuth Compression
RangeRes=0.75; %in meters
AzRes = 0.10; samples=azsamp; for k=5:250
    a=k;
    Ro=a*RangeRes;
    r=azch2(10,0.34,Ro,5,samples);
    fq=fft(im1(k,:));
    fr=fft(r);
    azf=fq.*(fr);
    im2(k,:) = fftshift(iffz(azf));
end

figure(33) xz=[1:1:372].*AzRes; yz=[5:1:200].*RangeRes;
surf(xz,yz,(abs(im2(5:200,:))).^0.1), shading interp
title('Azimuth Compressed Image');
caxis([1.0 1.9]) colormap(gray)
view(0,90) ylabel('Range (m)') xlabel('Azimuth (m)')
axis equal
axis([0 37 5 65])

figure(34)
plot(xz,unwrap(angle(im1(22,:))),1.5*pi),xz,...
unwrap(angle(azch2(10,0.34,22*RangeRes,9.53,samples)),1.5*pi))

figure(35)
plot(xz,abs(im1(22,:)),xz,100.*abs(azch2(10,0.34,22*...
RangeRes,9.53,samples)))

figure(36) plot(xz,20*log10(abs(im2(22,:))))

```

```
axis([0 40 20 50])
```

```
*****  
*****  
*****
```

```
function [c,t] = azchirp(bw,vel,range,samplerate,nsamples)  
%function c = azchirp(bw,vel,range,samplerate,nsamples)  
%  
% returns a centered azimuth chirp nsamples long  
% bw is the antenna beam width (in deg)  
% vel is the velocity (in m/s)  
% samplerate is the azimuth sample rate (PRF) in Hz  
  
global bandwidth  
fc=9.9e9; %frequency in Hz  
lambda=3.0e8/fc; %wavelength in m  
off=nsamples/2; %samp offset-cent chirp  
bandwidth=4*vel/lambda*sin(bw*pi/360); %chirp bandwidth in Hz  
deltaa=vel/bandwidth; %azimuth resolution  
denom=(lambda * range)/(2*deltaa*vel); %rect scaling constant  
for n=1:nsamples,  
    c(n)=0;  
    t(n)=(n-1-off)/samplerate; %time in s  
    if abs(t(n)/denom) < .5 %rect func  
        c(n)=exp(-j*(2*pi*vel^2/(lambda*range))*t(n)^2);%chirp wave  
    end  
end  
end
```

## Appendix C

### SAR Visual Basic Code for Instrument Control

```
Option Explicit
Dim flag1 As Integer, flag2 As Integer, pcdacval As Long
Dim counts As Long, trans As Single, flagendcal As Integer
Dim flagcalmes As Boolean, freqcap As String, runflag As Integer
Dim flagrun2 As Integer
'End of Globals

Private Sub channa_sld_change()
    phcomm1.Output = "w" + Format(channa_sld.Value, "000")
    Text13.Text = channa_sld.Value
End Sub

Private Sub channb_sld_Click()
    phcomm1.Output = "x" + Format(channb_sld.Value, "000")
    Text14.Text = channb_sld.Value
End Sub

Public Sub Form_Load()
    phcomm1.EOFEnable = True
    If phcomm1.PortOpen = False Then
        phcomm1.PortOpen = True
    End If
    Text7.Text = "Open"
    'Text4.Text = "11111900"    'Intial Count
    Text5.Text = "3"          'Tolerance
    Text8.Text = "100"        'DAC Increment
    Text9.Text = "200"        'Bandwidth
    Text10.Text = "9800"      'Intial Frequency
    trans = 0.00088215 * 8    'count to MHz coefficient
    calcomm.Text = " i      DAC   delta   Frequency" + Chr(10)
End Sub

Private Sub cleartxt_but_Click()
```

```

        oncomm.Text = ""
End Sub

Private Sub Command1_Click()
flag1 = 0
End Sub

Private Sub exit_Click()
    port_cl_cmd_Click
    End
End Sub

Private Sub freerunoff_but_Click()
    oncomm.Text = ""
    phcomm1.Output = "d"
End Sub

Private Sub freerunon_but_Click()
    oncomm.Text = ""
    phcomm1.Output = "c"
End Sub

Private Sub freqcount_cmd_Click()
    flag1 = 1
    While (flag1)
        oncomm.Text = ""
        phcomm1.Output = "b"
        'Beep
        wait
        wait
        wait
        wait
        wait
        DoEvents
    Wend
    'eofhandle
End Sub

Private Sub port_conn_cmd_Click()
    oncomm.Text = ""
    phcomm1.Output = "a"
End Sub

Private Sub port_cl_cmd_Click()
    If phcomm1.PortOpen = True Then

```

```

        phcomm1.PortOpen = False
    End If
    Text7.Text = "Closed"
End Sub

Private Sub port_op_cmd_Click()
    If phcomm1.PortOpen = False Then
        phcomm1.PortOpen = True
    End If
    Text7.Text = "Open"
End Sub

Private Sub port_opt_Click(Index As Integer)
    port_cl_cmd_Click
    phcomm1.CommPort = Index + 1
End Sub

Private Sub phcomm1_OnComm()
    Dim temp
    temp = phcomm1.CommEvent
    Text1.Text = Text1.Text + Str(temp)
    Select Case phcomm1.CommEvent
        ' Handle each event or error by placing
        ' code below each case statement

        ' Errors
        Case comEventBreak    ' A Break was received.
            MsgBox ("Break in Comm data")
        Case comEventFrame    ' Framing Error
        Case comEventOverrun  ' Data Lost.
        Case comEventRxOver   ' Receive buffer overflow.
        Case comEventRxParity ' Parity Error.
        Case comEventTxFull   ' Transmit buffer full.
        Case comEventDCB     ' Unexpected error retrieving DCB]

        ' Events
        Case comEvCD         ' Change in the CD line.
        Case comEvCTS       ' Change in the CTS line.
        Case comEvDSR       ' Change in the DSR line.
        Case comEvRing      ' Change in the Ring Indicator.
        Case comEvReceive   ' Received RThreshold # of
            ' chars.
        Case comEvSend      ' There are SThreshold number of
            wait           ' characters in the transmit
            eofhandle      ' buffer.
    End Select
End Sub

```

```

        Case comEvEOF      ' An EOF charater was found in the
                          ' input stream
        'MsgBox ("EOF Recieved")
        eofhandle
    End Select
End Sub

Private Sub eofhandle()
    Dim temp As String, capture1 As String, where, where2, where3
    Dim capture2 As String, freq As Double
    Dim countarr(100) As Long
    temp = ""
    'Do
        'DoEvents
        temp = phcomm1.Input + temp
    'Loop Until phcomm1.CommEvent = 7
    'Loop Until InStr(temp, Chr(26) + vbCrLf)
    oncomm.Text = temp + oncomm.Text
    where = InStr(oncomm.Text, "z") ' Find string in text.
    where2 = InStr(oncomm.Text, "@")
    where3 = InStr(oncomm.Text, "$")
    flagendcal = InStr(oncomm.Text, "FiN5")
    If where Then ' If found,
        oncomm.SelStart = where ' set selection start and
        oncomm.SelLength = 5 ' set selection length.
        capture1 = oncomm.SelText
        cap1_txt.Text = capture1
        oncomm.SelStart = where + 5 ' set selection start and
        oncomm.SelLength = 3 ' set selection length.
        capture2 = oncomm.SelText
        Text2.Text = capture2
        counts = CLng(capture1) * 256 + CLng(capture2)
        display_txt.Text = counts
        freq = counts * trans
        cap2_txt.Text = Format(freq, "0.000,000") + "MHz"
        If flag2 > 99 Then
            flag2 = 0
        End If
        flag2 = flag2 + 1
        countarr(flag2) = counts
        Text3.Text = flag2
        With MSChart1
            .Row = flag2
            .Data = capture2
        End With
    End If
End Sub

```

```

        flagrun2 = 0
    End If
    If where2 Then ' If found,
        oncomm.SelStart = where2 ' set selection start and
        oncomm.SelLength = 15 ' set selection length.
        calcomm.Text = calcomm.Text + oncomm.SelText + ", " +_
        freqcap + Chr(10)
        flagcalmes = False
    End If
    If where3 Then ' If found,
        oncomm.SelStart = where3 ' set selection start and
        oncomm.SelLength = 5 ' set selection length.
        capture1 = oncomm.SelText
        cap1_txt.Text = capture1
        oncomm.SelStart = where3 + 5 ' set selection start and
        oncomm.SelLength = 3 ' set selection length.
        capture2 = oncomm.SelText
        Text2.Text = capture2
        counts = CLng(capture1) * 256 + CLng(capture2)
        display_txt.Text = counts
        freq = counts * trans
        cap2_txt.Text = Format(freq, "0.000,000") + "MHz"
        flagrun2 = 0
    End If
End Sub

Private Sub wait()
    Dim i
    For i = 1 To 200000
    Next
End Sub

Private Sub reset_Click()
    Form_Load
End Sub

Private Sub Slider1_Change()
    dacval_txt.Text = Slider1.Value
    phcomm1.Output = "e" + Format(Slider1.Value, "00000")
    wait
    wait
    wait
    DoEvents
    phcomm1.Output = "b"
End Sub

```



```

Private Sub statcal_but_Click()
Dim vcou As Long, tol As Long, flagstat As Boolean
Dim dacin As Long, bw As Long, flagcal2 As Boolean
Dim flagcal3 As Boolean, inccount As Long, i
    Slider1.Value = 0
    Slider1_Change
    wait
    DoEvents
    wait
    wait
    Slider1.Value = 0
    Slider1_Change
    wait
    DoEvents
    wait
    wait
    flagstat = True
    flagcal2 = True
    flagcal3 = False
    pcdacval = 0
    tol = CLng(Text5.Text)
    vcou = CLng(CLng(Text10.Text) / trans)
    Text12.Text = vcou
    Text4.Text = vcou
    dacin = CLng(Text8.Text)
    bw = CLng(Text9.Text)
    inccount = CLng(bw / trans / 100)
    Text11.Text = inccount
    phcomm1.Output = "f"
    wait
    wait
While (flagstat)
    phcomm1.Output = Format(pcdacval, "00000")
    Text6.Text = pcdacval
    'wait
    wait
    DoEvents
    wait
    wait

If counts < (vcou + tol) And counts > (vcou - tol) Then
    'wait
    phcomm1.Output = "j"
    Check1.Value = 1

```

```

    freqcap = cap2_txt.Text
    calcomm.Text = calcomm.Text + " 1st, " + _
        Format(pcdacval, "00000") + _
        ", 000, " + freqcap + Chr(10)
    flagstat = False
ElseIf counts > vcou Then
    If flagcal2 Then
        dacin = 10
        flagcal3 = True
    End If
    Text8.Text = dacin
    pcdacval = pcdacval - dacin
    phcomm1.Output = "i"
Else
    pcdacval = pcdacval + dacin
    phcomm1.Output = "i"
    If flagcal3 Then
        dacin = 1
        flagcal2 = False
    End If
End If
Wend
'wait
wait
For i = 1 To 100
    Beep
Next
'vcou = vcou - inccount
'DoEvents
While Not flagendcal
    vcou = vcou + inccount
    flagcalmes = True
    Text12.Text = vcou
    While flagcalmes
        If counts < (vcou + tol) And counts > (vcou - tol) Then
            'wait
            freqcap = cap2_txt.Text
            phcomm1.Output = "k"
        ElseIf counts > vcou Then
            'wait
            phcomm1.Output = "l"
        Else
            'wait
            phcomm1.Output = "m"
        End If
    End While
End While

```

```
        wait
        DoEvents
        'wait
        'wait
        'DoEvents
    Wend
Wend
For i = 1 To 1000
    Beep
Next
End Sub

Private Sub tranon_but_Click()
    phcomm1.Output = "g"
End Sub

Private Sub tranoff_but_Click()
    runflag = 0
End Sub
```

## Appendix D

### PicBasicPro Code for Transmitter Module

```
'10 GHz SAR Using FM/CW
'Written by Ryan Smith
'Date 8/12/00
'Code generated for a PIC16C73A

'-----
'Variable Definitions

'Interrupt Variables
wsave  var byte $20 system 'saved in such a manner to protect
wsave1 var byte $a0 system 'both banks of registers
ssave  var byte $21 system
psave  var byte $22 system
fsave  var byte $23 system

'counter con    125

baud    con 84      'Baud Rate (9600)
c  var byte      'character
spout   var PortC.6  'Serial Output Port
spin    var PortC.7  'Serial Input Port

trigger var PortC.4  'trigger & EXT Counter:Reset
s1  var PortC.2      'SR:0-shifts right 1-parallel load
exttime var PortC.1  'Line to turn ext. counter on(1) or off(0)
srclk  var PortC.5   'load dac & shift register clock
datpin  var PortC.3  'shifted in data
fin var PortC.0      'Inut frequency to internal timer
datain  var byte

Fcap    var word bank1 'Captured frequency forced to filebank 1
FcapH  var Fcap.byte1 'high byte of Fcap
FcapL  var Fcap.byte0 'low byte of Fcap
```

```

dacval  var word          'digital value to send to dac
dacvalh var dacval.byte1  'high byte of dacval
dacvall var dacval.byte0  'low byte of dacval
deltavl var byte[51]     'incremental voltage array upper
deltavu var byte[51]     'incremental voltage array upper
pcdacval var word        'digital DAC value received from PC

i  var word          'loop counter
j  var word          'loop counter
k  var byte          'loop counter
flag1 var bit        'run loop flag
'-----
'Initialization
'-----
'Timer1 set up in Capture Mode
T1CON = %000110      'Timer1 setup
'-----
'Set up ports...
define OSC 20
TRISA = %00000000    '0 is output
TRISB = %00000000    '1 is input
TRISC = %10001001
ADCON1 = %111
'-----
'Initial States
srclk=0:exttime=1:trigger=0

for i = 0 to 49
    deltaVL[i]=160
    deltaVU[i]=160
next i
'deltaVL[0] = 0

serout2 spout,baud,["10 GHZ SAR Transmitter",169,10,_,_
    "Microwave Earth Remote Sensing",10,_,_
    "Brigham Young University",10,"8/12/00"_,_
    ,13,10,26,13,10,13,10,26,13,10]
while 1
cmdln:
    serin2 spin,baud,[c]
    if c="a" then
        serout2 spout,baud,["Communication Established",_,_
            13,10,26,13,10]
    endif
    if c="b" then

```

```

        gosub freqcount
        serout2 spout,baud,["FiN1",13,10,26,13,10]
    endif
    if c="c" then
        gosub freerunon
        serout2 spout,baud,["FiN2",10,26]
    endif
    if c="d" then
        gosub freerunoff
        serout2 spout,baud,["FiN3",10,26]
    endif
    if c="e" then
        gosub loaddac
        serout2 spout,baud,["FiN4",10,26]
    endif
    if c="f" then
        gosub statcal
        serout2 spout,baud,["FiN5",10,26]
    endif
    if c="g" then
        gosub run
        serout2 spout,baud,["FiN6",10,26]
    endif
wend

'*****
freqcount:
    T1CON.0=0:exttime=1:trigger=1:trigger=0:s1=1
    TMR1H=0:TMR1L=0:T1CON.0=1
    for j = 1 to 1
        exttime=0
        for i = 1 to 125
            next i
        exttime=1
        Fcaph=TMR1H:Fcapl=TMR1L
        TMR1H=0:TMR1L=0
        gosub shiftdata
        serout2 spout,baud,["z",dec5 Fcap,dec3 datain,"qq",10]
        'serout2 spout,baud,["Int:",dec5 Fcap," Ext:",dec3 datain,10]
        trigger=1:trigger=0:
    next j
    T1CON.0=0
    Return
'*****
freerunon:

```

```

        trigger=1:trigger=0:exttime=0
    Return
freerunoff:
    exttime=1
    gosub shiftdata
    Return
'*****

shiftdata:
    s1=1:srclk=1:srclk=0:srclk=1:srclk=0:s1=0
    datain.7=datpin:srclk=1:srclk=0
    datain.6=datpin:srclk=1:srclk=0
    datain.5=datpin:srclk=1:srclk=0
    datain.4=datpin:srclk=1:srclk=0
    datain.3=datpin:srclk=1:srclk=0
    datain.2=datpin:srclk=1:srclk=0
    datain.1=datpin:srclk=1:srclk=0
    datain.0=datpin
    s1=1
    Return
'*****

loaddac:
    srclk=1
    serin2 spin,baud,[dec5 dacval]
    portb=dacvall
    porta=dacvalh
    srclk=0
    srclk=1
    Return

'*****

statcal:
'LFM Generator
    srclk = 1
    focal: serin2 spin,baud,[dec5 pcdacval]
        dacval = pcdacval
        gosub measure
        if c = "i" then focal
        'serout2 spout,baud,[64, "1st, ",dec5 dacval,", 000",10]
        for k = 0 to 49
        'if k = 0 then skip1
            dacval = dacval + DeltaV1[k]
        meas1: gosub measure
            if c="k" then

```

```

        deltavl[k+1] = deltavl[k]
        goto skip1
    endif
    if c="l" then
        DeltaVl[k]=DeltaVl[k]-1
        dacval=dacval-1
        goto meas1
    endif
    if c="m" then
        DeltaVl[k]=DeltaVl[k]+1
        dacval=dacval+1
        goto meas1
    endif
skip1:  serout2 spout,baud,[64, dec3 2*k,", ",_
dec5 dacval,", ",dec3 deltavl[k],10]
'-----
        dacval = dacval + DeltaVu[k]
meas2:  gosub measure
        if c = "k" then
            deltavu[k+1] = deltavu[k]
            goto skip2
        endif
        if c = "l" then
            deltavu[k]=deltavu[k]-1
            dacval=dacval-1
            goto meas2
        endif
        if c = "m" then
            deltavu[k]=deltavu[k]+1
            dacval=dacval+1
            goto meas2
        endif
skip2:  serout2 spout,baud,[64, dec3 2*k+1,", ",_
dec5 dacval,", ",dec3 deltavu[k],10]
next i

return
'*****
measure:
    PortB = dacvall
    PortA = dacvalh
    srclk=0
    srclk=1
    T1CON.0=0:exttime=1:trigger=1:trigger=0:s1=1
    TMR1H=0:TMR1L=0:T1CON.0=1 'Clearing int. counter registers
                                'and turning on counter

```



```

extttime=0          'Turn Ext. Counter ON
for i = 1 to 125    'loop determines period of phase count
next i
extttime=1          'Turn Ext. Counter OFF
FcapH=TMR1H:FcapL=TMR1L 'Capture Phase Count from Int. Counter
TMR1H=0:TMR1L=0    'Clear Int. Counter Registers
gosub shiftdata     'Collect Shift Reg. Data to "datain"
serout2 spout,baud,["z",dec5 Fcap,dec3 datain,"qq",10]
serin2 spin,baud,[c]
trigger=1:trigger=0 'Resets External Counter
T1CON.0=0
Return

```

```

'*****

```

```

run:

```

```

trigger = 0
extttime = 1
flag1 = 1
TMR1H = 0
TMR1L = 0
srclk = 1
dacval=pcdacval
Fcap = 0
'Ramp UP
while flag1
  trigger = 1 'Trigger for receiver
  trigger = 0
  dacval=pcdacval
  for i = 0 to 49
    dacval = dacval + DeltaVl[i]
    PortB = dacvall
    PortA = dacvalh
    'for k = 0 to 17
    'next k
    @nop
    srclk = 0          'Loads the DAC
    srclk = 1
  ,-----
    dacval = dacval + DeltaVu[i]
    PortB = dacvall
    PortA = dacvalh
    'for k = 0 to 18
    'next k
    srclk = 0
    srclk = 1

```

```

        next i
    -----
'Ramp Down
    dacval=pcdacval
    PortB = dacvall
    PortA = dacvalh
    srclk = 0
    srclk = 1
    pause 10
    T1CON.0=0:s1=1
    TMR1H=0:TMR1L=0:T1CON.0=1    'Clearing int. counter
                                'registers and turning on counter
    exttime=0                    'Turn Ext. Counter ON
    for i = 1 to 125            'loop determines period of phase count
    next i
    exttime=1                    'Turn Ext. Counter OFF
    Fcaph=TMR1H:Fcapl=TMR1L    'Capture Phase Count from
                                'Int. Counter
    TMR1H=0:TMR1L=0            'Clear Int. Counter Registers
    gosub shiftdata            'Collect Shift Reg. Data to "datain"
    serout2 spout,baud,["$",dec5 Fcap,dec3 datain,"qq",10]
    Oserin2 spin,baud,[dec5 pcdacval, dec1 flag1]
    T1CON.0=0
wend
    serout2 spout,baud,["FiN2",10]
return

'*****
'VCO Ramp
ramp:
    dacval = 0
    'Ramp UP
    PortB = dacvall
    PortA = dacvalh
    srclk=0
    srclk=1
    pause 10
    for j = 0 to 100
        for i = 0 to 2046
            dacval = dacval + 8
            PortB = dacvall
            PortA = dacvalh
            srclk=0
            srclk=1

```

```
    next i
',-----
  for i = 0 to 2046
    dacval = dacval - 8
    PortB = dacvall
    PortA = dacvalh
    srclk=0
    srclk=1
  next i
next j
serout2 spout,baud,["FiN6",10]
return
'*****
```

## Appendix E

### PicBasicPro Code for Receiver Module

```
'10 GHz SAR Reciever
'Written by Ryan Smith
'Date 8/24/00
'Code generated for a PIC16C73A

baud    con 84      'Baud Rate (9600)
c      var byte    'character
spout   var PortC.6  'Serial Output Port
spin    var PortC.7  'Serial Input Port

Asdata  var PortA.0  'Channel A Serial Data Line
ACLK    var PortA.1
ADaten  var PortA.2
AbPO    var PortA.3

gaina   var byte
gainb   var byte

Bsdata  var PortB.7  'Channel A Serial Data Line
BCLK    var PortB.6
BDaten  var PortB.5
BbPO    var PortB.4

'Set up ports...
define  OSC 20
TRISA = %00000000  '0 is output
TRISB = %00000000  '1 is input
TRISC = %10001001
ADCON1 = %111
```

```

AbPO = 1:   ADaten = 1: ACLK = 0
BbPO = 1:   BDaten = 1: BCLK =0

```

```

serout2 spout,baud,["10 GHZ SAR Receiver",169,10,_
  "Microwave Earth Remote Sensing",10,_
  "Brigham Young University",10,"8/12/00",13,10,_
  26,13,10,13,10,26,13,10]

```

```
while 1
```

```
cmdln:
```

```
  serin2 spin,baud,[c]
```

```
  if c="a" then
```

```
    serout2 spout,baud,["Communication Established",_
      13,10,26,13,10]
```

```
  endif
```

```
  if c="w" then
```

```
    gosub channa
```

```
    serout2 spout,baud,["FiN8",10,26]
```

```
  endif
```

```
  if c="x" then
```

```
    gosub channb
```

```
    serout2 spout,baud,["FiN9",10,26]
```

```
  endif
```

```
wend
```

```
'*****
```

```
channa:
```

```
  serin2 spin,baud,[dec3 gaina]
```

```
  ADaten = 0
```

```
  Asdata = gaina.7:ACLK=1:ACLK=0
```

```
  Asdata = gaina.6:ACLK=1:ACLK=0
```

```
  Asdata = gaina.5:ACLK=1:ACLK=0
```

```
  Asdata = gaina.4:ACLK=1:ACLK=0
```

```
  Asdata = gaina.3:ACLK=1:ACLK=0
```

```
  Asdata = gaina.2:ACLK=1:ACLK=0
```

```
  Asdata = gaina.1:ACLK=1:ACLK=0
```

```
  Asdata = gaina.0:ACLK=1:ACLK=0
```

```
  ADaten = 1
```

```
  Return
```

```
'*****
```

```
channb:
```

```
  serin2 spin,baud,[dec3 gainb]
```

```
  BDaten = 0
```

```
  Bsdata = gainb.7:BCLK=1:BCLK=0
```

```
  Bsdata = gainb.6:BCLK=1:BCLK=0
```

```
Bsdata = gainb.5:BCLK=1:BCLK=0
Bsdata = gainb.4:BCLK=1:BCLK=0
Bsdata = gainb.3:BCLK=1:BCLK=0
Bsdata = gainb.2:BCLK=1:BCLK=0
Bsdata = gainb.1:BCLK=1:BCLK=0
Bsdata = gainb.0:BCLK=1:BCLK=0
BDaten = 1
Return
```



## Appendix F

### PECL Design Overview

#### F.1 ECL Basic Gate

Emitter Coupled Logic (ECL) in Pico Seconds (ECLinPS) logic family is the focus of this overview. Data sheets often confuse the issue of ECL design by many equations and charts to help designers with transmission line effects due to the high speed of ECL devices. It is much simpler to have a basic understanding of an ECL device layout and its DC and AC electrical characteristics, and then apply transmission theory to match the transmission lines.

#### F.2 Positive Emitter Coupled Logic

ECL is developed using ground for  $V_{CC}$  and  $-5V$  for  $V_{EE}$ . This voltage arrangement is selected because ground is a relatively stable power plane, and the performance of ECL devices are sensitive to fluctuations in  $V_{CC}$  voltage but are tolerant of noise in the  $V_{EE}$  power plane. Positive ECL (PECL) is the name given when an ECL circuit is designed using a  $+5V$  supply for  $V_{CC}$  and ground for  $V_{EE}$ . Any ECL chip will work in a PECL design with the exception of logic translators to and from TTL. Specific translators are available for both PECL and ECL circuits. PECL can be implemented by the careful design of a power plane for  $V_{CC}$  and  $V_{TT}$  which should be well isolated from analog and digital planes. Table F.1 shows specified voltage levels by Motorola [43] for a temperature range of 0 to  $85^{\circ}C$ .

It is seen from the conversion table that the voltage is simply shifted up by 5 Volts. It is also seen from specifications that the typical AC signal is approximately  $800\text{ mV}_{pp}$ . This is equivalent to 2.0 dBm referenced to a  $50\ \Omega$  system.



Table F.1: Motorola’s Specifications for ECL/PECL DC Level Conversion from  $V_{CC} = 0.0V \Rightarrow 5.0V$ . \* denotes specifications defined by author.

Symbol	Description	Min	Max	Unit
$V_{OH}$	Logic Output High Voltage	-1.025/3.975	-0.880/4.120	V
$V_{OL}$	Logic Output Low Voltage	-1.810/3.190	-1.620/3.380	V
$V_{OHA}$	$V_{OH}$ with inputs biased	—	-1.610/3.390	V
$V_{OLA}$	$V_{OL}$ with inputs biased	-1.035/3.965	—	V
$V_{IH}$	Logic Input High Level	-1.165/3.835	-0.880/4.120	V
$V_{IL}$	Logic Input Low Level	-1.810/3.190	-1.475/3.525	V
$V_{BB}$	Reference Voltage	-1.380/3.620	-1.260/3.740	V
$V_{TT}^*$	Termination Voltage	-2.000/3.000	—	V
$V_{CC}^*$	Collector Voltage	0.000/5.000	—	V
$V_{EE}^*$	Emitter Voltage	-5.000/0.000	—	V

### F.3 Termination of Transmission Lines and Interconnects

Due to the differential amplifiers on the input of the devices, the signal is switched between one of two voltage states. The current drain on each device remains constant regardless of the state of the output. Because the inputs of the devices have internal pull-down resistors, the unused inputs may be left open. If the output voltage level is a concern, National Semiconductor has several recommendations on proper terminations [44]. The outputs may be left unterminated.

A simple scheme maybe implemented to bias the inputs of a device in order to couple a signal that has no DC content or information. This design allows the optimum performance to be obtained. Figure F.1 shows the inverting input of the receiving device connected directly to the reference voltage  $V_{BB}$  and a coupling capacitor to ground to minimize the ripple on  $V_{BB}$ . The non-inverting pin is then AC coupled to the desired signal and terminated to  $V_{BB}$  with the line system impedance resistance, which in this case is  $50 \Omega$ . By connecting the termination resistor to  $V_{BB}$  the non-inverting is biased at the reference voltage and the maximum dynamic range is achieved for the input signal. The receiving device may go into oscillation or an unknown state if no signal is present, and a fix for this is outlined by [45].

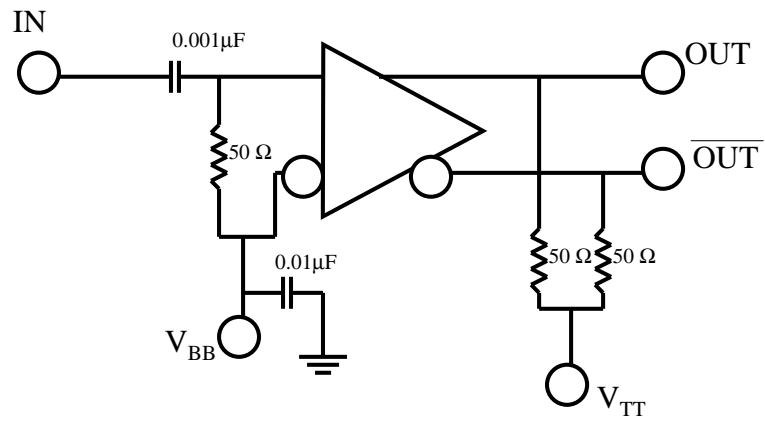


Figure F.1: An AC Signal Coupled to an ECL Device.



## Bibliography

- [1] F. T. Ulaby, R. K. Moore, and A. K. Fung, *Microwave Remote Sensing Active and Passive*, vol. I, Artech House, 1981.
- [2] R. L. Smith, “Rain and cloud cover detection in south asia”, EcEn Department Report TR-L000-01.1, Brigham Young University, 459 Clyde Building, Provo, Utah, 84602, April 2001.
- [3] A. E. Robertson, “Multi-baseline interferometric sar for iterative height estimation”, Master’s thesis, Brigham Young University, Provo, Utah, December 1998.
- [4] M. Zink and R. Bamler, “X-sar radiometric calibration and data quality”, *IEEE TRANSACTIONS ON Geoscience and Remote Sensing*, vol. 33, no. 12, 1995.
- [5] R. L. Jordan, B. L. Huneycutt, and M. Werner, “The sir-c/s-sar synthetic aperture radar system”, *IEEE TRANSACTIONS ON Geoscience and Remote Sensing*, vol. 33, no. 4, pp. 829–839, July 1995.
- [6] Staff, “The critical role of sar in earth system science”, White paper, Alaska SAR Facility User Working Group, June 1998.
- [7] Y. Kim, Y. Lou, J. van Zyl, L. Maldonado, T. Miller, T. Sato, and W. Skotnicki, “Nasa/jpl airborne three-frequency polarimetric/interferometric sar system”, *IEEE Geoscience and Remote Sensing Symposium*, vol. 3, pp. 1612–1614, May 1996.
- [8] G. F. Adams, D. A. Ausherman, S. L. Crippen, G. T. Sos, B. P. Williams, and R. Heidelberg, “The erim interferometric sar: Ifsare”, *IEEE Aerospace and Electronics Systems Magazine*, vol. 11, no. 12, pp. 31–35, December 1996.

- [9] J. B. Mercer and M. Gill, “Radar-derived DEMs for urban areas”, *ISPRS Commission IV*, vol. 3, September 1998.
- [10] C. L. Glennie, *An Analysis of Airborne Gravity by Strapdown INS/DGPS*, PhD thesis, University of Calgary, 2500 University Drive NW, Calgary, AB, T2N 1N4, 1999.
- [11] B. Bullock and L. Fosse, “Accurate, low-cost digital elevation model (DEM) products”, *Wall Street Corporate Reporter*, vol. 6, no. 21, September 2001.
- [12] B. R. Jarrett, “Byu sar, a low cost, compact synthetic aperture radar”, Master’s thesis, Brigham Young University, Provo, Utah, August 1994.
- [13] D. G. Thompson, D. V. Arnold, D. G. Long, G. F. Miner, M. A. Jensen, T. W. Karlinsey, A. E. Robertson, and J. S. Bates, “Ysar and yinsar: Compact, low-cost synthetic aperture radars”, in *European Conference on Synthetic Aperture Radar*, Friedrichshafen, Germany, May 1998, pp. 25–27.
- [14] D. G. Thompson, D. V. Arnold, D. G. Long, G. F. Miner, T. W. Karlinsey, and A. E. Robertson, “Ysar: A compact, low-cost synthetic aperture radar”, in *IGARSS*, Singapore, August 1997, IEEE, pp. 386–388.
- [15] D. G. Thompson, *Innovative Radar Interferometry*, PhD thesis, Brigham Young University, 459 Clyde Building, Provo, Utah, 84602, August 2001.
- [16] D. G. Thompson, D. V. Arnold, and D. G. Long, “Yinsar: a compact, low-cost interferometric synthetic aperture radar”, in *IGARSS*, Hamburg, Germany, July 1999, IEEE, pp. 598–600.
- [17] R. B. Lundgreen, “Method of motion compensation of yinsar data”, Master’s thesis, Brigham Young University, Provo, Utah, August 2001.
- [18] M. Soumekh, “Wide-bandwidth continuous-wave monostatic/bistatic synthetic aperture radar imaging”, in *1998 International Conference on Image Processing*, IEEE, 1998, vol. 3, pp. 361–365.

- [19] M. Soumekh, “Fm-cw sar and phased array spatial-velocity imaging”, in *1994 International Conference on Image Processing*. IEEE, 1994, vol. 1, pp. 471–475.
- [20] H. D. Griffiths, “Conceptual design of an ultra high-resolution mm-wave synthetic aperture radar”, in *Proceedings of the 1996 IEEE National Radar Conference*. IEEE, 1996, pp. 225–260.
- [21] G. Connan, H. D. Griffiths, and P. V. Brennan, “Fmcw-sar development for internal wave imaging”, in *MTS/IEEE Conference Proceedings*. IEEE, 1997, vol. 1, pp. 73–78.
- [22] S. Haykin, *Adaptive Filter Theory*, Prentice Hall, 2 edition, 1991.
- [23] A. V. Oppenheim, Willsky, and Nawab, *SIGNALS & SYSTEMS*, Prentice Hall, 2 edition, 1997.
- [24] H. R. Raemer, *Radar Systems Principles*, CRC Press, 1996.
- [25] P. D. L. Beasley and A. G. Stove, “Pilot - an example of advanced fmcw techniques”, *IEEE Colloquium on High Time-Bandwidth Product Waveforms in Radar and Sonar*, pp. 10/1–10/5, 1991.
- [26] J. C. Curlander and R. N. McDonough, *Synthetic Aperture Radar: Systems and Signal Processing*, Remote Sensing. Wiley, 1991.
- [27] D. V. Arnold, “Vector quantization of synthetic array radar data”, Master’s thesis, Brigham Young University, Provo, Utah, 1987.
- [28] F. T. Ulaby, R. K. Moore, and A. K. Fung, *Microwave Remote Sensing Active and Passive*, vol. II, Artech House, 1986.
- [29] S. S. Piper, “Homodyne fmcw radar range resolution effects with sinusoidal nonlinearities in the frequency sweep”, in *Record of the IEEE 95 International Radar Conference*. IEEE, 1995, pp. 563–567.

- [30] C. Weidong, X. Shanxia, W. Dongjin, and L. Falin, “Range performance analysis in linear fmcw radar”, in *2nd International Conference on Microwave and Millimeter Wave Technology*. IEEE, 2000, pp. 654–657.
- [31] S. S. Piper, “Fmcw linearizer bandwidth requirements”, in *Proceedings of the 1991 IEEE National Radar Conference*. IEEE, 1991, pp. 142–146.
- [32] J. Fuchs, K. D. Ward, M. P. Tulin, and R. A. York, “Simple techniques to correct for vco nonlinearities in short range fmcw radars”, in *IEEE Microwave Technologies and Techniques International Symposium Digest*. IEEE, 1996, vol. 2, pp. 1175–1178.
- [33] B. K. Kang, H. J. Kwon, B. K. Mheen, H. J. Yoo, and Y. H. Kim, “Nonlinearity compensation circuit for voltage-controlled oscillator operating in linear frequency sweep mode”, in *IEEE Microwave and Guided Wave Letters*. IEEE, December 2000, vol. 10, pp. 537–539.
- [34] J. L. Waite, “An interferometric radar system that detects track hazards to improve safety”, Master’s thesis, Brigham Young University, Provo, Utah, May 2001.
- [35] J. C. Beard, “Railroad hazard detection system using an interferometric radar”, Master’s thesis, Brigham Young University, Provo, Utah, October 2000.
- [36] R. L. Smith and D. V. Arnold, “Development of a low cost, fm/cw transmitter for remote sensing”, *Proceedings, IEEE Geoscience and Remote Sensing Symposium*, vol. 5, pp. 2328–2330, 2000.
- [37] Staff, “1998 vco catalog”, Tech. Rep., EMHISER Micro-Tech, 1998.
- [38] D. M. Pozar, *Microwave Engineering*, John Wiley & Sons, 2 edition, 1998.
- [39] A. V. Oppenheim and R. W. Schaffer, *Discrete-Time Signal Processing*, Prentice Hall, 1989.

- [40] K.C. Gupta, R. Garg, and I. Bahl, *Microstrip Lines and Slotlines*, Artech House, 2 edition, 1996.
- [41] K. Hettak and M. G. Stubbs, “The use of uniplanar technology to reduce microwave circuit size”, *Microwave Journal*, pp. 302–316, May 2001.
- [42] R. N. Simons, *Coplanar Waveguide Circuits, Components, and Systems*, John Wiley and Sons, 2001.
- [43] C. Petty and T. Pearson, “Designing with PECL (ecl at +5.0v)”, Logic AN1406, Motorola, February 1998.
- [44] Staff, “Terminating F100K ECL inputs”, Logic AN-682, National Semiconductor, July 1992.
- [45] Staff, “High performance ECL data, ECLINPS and ECLINPS Lite”, Logic DL140/D, REV2, Motorola, December 1993, 4-29 to 4-31.